Periodic and Aperiodic Plasmon Lattice Lasers

Ph.D. thesis University of Amsterdam, January 2016
Periodic and Aperiodic
Plasmon Lattice Lasers
Aaltje Hinke Schokker

ISBN 978-94-92323-01-9

A digital version of this thesis can be downloaded from http://www.amolf.nl.

Periodic and Aperiodic Plasmon Lattice Lasers

ACADEMISCH PROEFSCHRIFT

ter verkrijging van de graad van doctor
aan de Universiteit van Amsterdam
op gezag van de Rector Magnificus
prof. dr. D. C. van den Boom
ten overstaan van een door het College voor Promoties
ingestelde commissie,
in het openbaar te verdedigen in de Agnietenkapel
op donderdag 28 januari 2016, te 14:00 uur

door

Aaltje Hinke Schokker

geboren te Drachten

Promotiecommissie

Promotor	prof. dr. A. F. Koenderink	Universiteit van Amsterdam
Overige leden	prof. dr. W. L. Barnes	University of Exeter
	prof. dr. A. Fiore	TU Eindhoven
	prof. dr. M. S. Golden	Universiteit van Amsterdam
	prof. dr. A. Lagendijk	Universiteit van Amsterdam
	dr. R. J. C. Spreeuw	Universiteit van Amsterdam

The work described in this thesis is part of the research program of the
"Stichting voor Fundamenteel Onderzoek der Materie (FOM)"
which is financially supported by the
"Nederlandse Organisatie voor Wetenschappelijk Onderzoek (NWO)".

This work was carried out at the
Center for Nanophotonics,
FOM Institute for Atomic and Molecular Physics AMOLF,
Science Park 104, 1098 XG Amsterdam, The Netherlands,
where a limited number of copies of this dissertation are available.

Contents

1

Introduction

1.1 Background

Light interacts with matter through scattering, absorption and fluorescence. Without matter there is nothing to look at, and without light the world around us can not be seen. The appearance of an object is determined by how it interacts with light. For instance, both white paper and mirrors reflect all colors of the light, yet they appear very different. When light impinges on a paper sheet, light penetrates many wavelengths experiencing multiple reflections from irregularities within the paper. A part of the multiply scattered light will emerge again from the paper, but due to the multiple scattering almost all information about how light impinged onto, and travelled through the medium is lost, resulting in a diffuse, white appearance. In contrast, mirrors reflect light specularly and the reflected light retains full information of the input beam, even allowing us to see an image of the scene illuminating the mirror. The difference between white paper and a specularly reflecting interface shows that geometry matters for light-matter interaction. In addition, also the electronic structure of the material matters. For instance, both glass and mirrors display a specular reflection, but mirrors much more strongly so than glass. The distinction is through the dielectric constant, or polarizability, of the matter [1]. Glass is an insulator, in which electrons are tightly bound to atomic nuclei, leading to a small, and positive dielectric constant. In contrast, mirrors consist of conductive metals and electromagnetic fields that interact with the metal surface cause conduction electrons to move in such a manner that light can not penetrate by more then the skin depth. In terms of optical constants, conducting materials are characterized by having a negative ϵ_r. When instead of a flat surface you would have a particle smaller than the skin depth, which is typically 10 to 100 nm, the electromagnetic fields can significantly penetrate. The electron density in the particle can undergo a collective

resonant oscillation that is driven by the impinging light field, creating a quasiparticle called plasmon polariton [2, 3]. This thesis deals with a particular combination of matter and geometry, namely particles of metal smaller than the skin depth.

Due to the involvement of all free electrons in the particle in this plasmon oscillation, the interaction between light and the particle is much stronger than it would be when the material is not conductive. This is especially true at resonance, when the driving light field corresponds to the eigenfrequency of the electron density oscillation, which occurs for frequencies in the visible spectral range. This increased light matter interaction has three important consequences. First, plasmonic structures have a much stronger polarizability per volume and therefore scatter light much more strongly than their dielectric counterparts [4]. Second, the strong light matter coupling in plasmonics makes possible subdiffraction confinement of light. Third, in the near field of plasmonic structures, a huge field enhancement can occur. These three properties have drawn much attention among researchers, not only because of the many fundamental questions these properties give rise to, but also from the perspective of practical applications such as Surface Enhanced Raman Spectroscopy [5–7], sensing [8–12] and enhanced light trapping in solar cells [13–16]. However, there is one major factor that limits using plasmonics in functional systems: loss. Scattering of electrons by phonons causes loss which is known as "Ohmic damping". This is accounted for within the "Drude-Sommerfeld" model for the transport of electrons in solids [17] which starts out from a classical equation of motion describing free electrons driven by light

$$m_e \frac{\partial^2 \vec{r}}{\partial t^2} + m_e \gamma \frac{\partial \vec{r}}{\partial t} = -e\vec{E}_0 e^{-i\omega t} \tag{1.1}$$

where $r(\vec{t})$ represents position, m_e is the (effective) electron mass, E_0 is the incident electric field that drives the system and γ represents the rate of Ohmic loss, due to scattering of electrons off phonons, impurities and soforth. In addition to the Ohmic damping represented by γ, depending on the metal electron density, oscillations are dampened by interband and intraband transitions. Interband transitions occur when an electron absorbs a photon and is excited from the valence band to the Fermi surface, or from the Fermi surface to a conduction band. Intraband transitions occur by scattering with other electrons and are dependent on the quality of the metal. In many optical experiments, a large fraction of the incident light is therefore absorbed by the metal and transformed into heat. Three solutions have been proposed. First, some authors have suggested that very high positive index materials, such as silicon in the visible can show strong optical resonances with much lower loss than metals [18]. Second, many groups are exploring the possibility of new materials that have lower loss in addition to having a negative, i.e. metal-like, dielectric constant [15, 19, 20]. Third, loss can be compensated by including gain. Various demonstrations of loss compensation in plasmonic systems exist [21–26] in which a plasmonic particle or surface is embedded in or is adjacent to a gain material, which is typically a semiconductor material or an organic dye. The gain medium is excited by an external source and emission by the gain medium feeds the plasmonic mode.

Going beyond mere compensation of losses, i.e., exactly negating absorption by

gain, one can also wonder if it is possible to realize lasing based on plasmons. This was first envisioned in the plasmonic context by Stockman and Bergmann in 2003 [27], who proposed that a deep subwavelength plasmonic particle in a gain medium could lase. This idea is related to the "scattering laser" [28] in which the feedback required for lasing is generated by scatterers, instead of by a cavity with finely tuned mirrors. Recently several plasmonic lasers were reported, notably using nanoparticle, nanowires, metal films, and diffractive plasmonic systems. In this thesis we study lasers created by 2D lattices of plasmonic particles in a slab of gain medium. In section 1.2, we discuss the configuration of the laser that we study in this thesis, examining all the ingredients that make up the plasmonic mode structure on which the laser is built. In section 1.4 we discuss the concept of a gain medium and how some elementary laser characteristics derive from rate equations. Subsequently, a summary is given on what has been done so far regarding plasmonic lasers, and what type of questions define debates in the plasmonics community on lasing. Finally we preview the content of the subsequent thesis chapters.

1.2 Building blocks of plasmon lattice lasers

The system we study throughout this thesis consists of the following basic geometry. First, we have a planar glass substrate which can be considered infinitely thick. Next, on top of this, a periodic lattice of isolated silver particles is made that are strong plasmonic scatterers, which provide feedback. Finally, the particles are embedded in a thin polymer layer that has two functions. On one hand it acts as gain medium, as we dope the polymer with fluorophores. On the other hand, as the polymer has a higher index than the glass and air surrounding it, it supports waveguide modes. In this section we discuss textbook physics that is generally used to describe waveguides, scatterers, and periodic systems.

1.2.1 Waveguide modes of slabs

To describe the optical response of a particle array embedded in a photoresist, it is easiest to start with the simple case of a bare waveguide. Waveguides exist in many forms and shapes, the most frequently applied ones being 1D waveguides such as optical fibers, as well as 2D waveguides in form of dielectric slabs. Waveguiding in dielectric layers can occur when there is an index contrast, i.e. the waveguide has a higher index then the two adjacent media. In addition, the layer can only support waveguide modes if it is sufficiently thick. The waveguide dispersion as well as the mode profile in the waveguide can be calculated using the method described by Urbach and Rikken [29]. In the method by Urbach, one first writes down an Ansatz for the field in each medium. In this Ansatz, one incorporates two steps that are common for any problem involving stratified media. The first is that in each layer one writes down the field as a sum of plane waves, where the parallel momentum is the same in all layers as required by translational invariance. The second is that polarization can be separated in "s" and "p",

or equivalently TE and TM illustrated in figure 1.1. With these assumptions, the field in

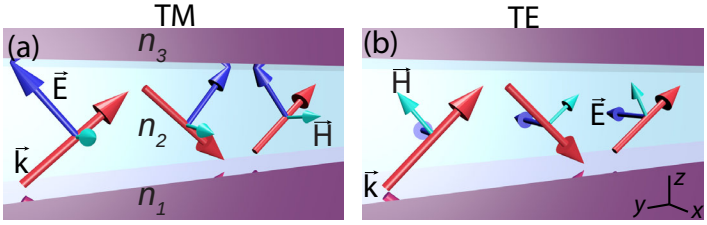

Figure 1.1: In (a) a TM mode of a slab waveguide is sketched, where the magnetic field, represented by the green arrow, points in a direction transverse to the waveguide, and the electric field represented by the blue arrow has a component directed out of the waveguide plane. The red arrow indicates the wavevector. In (b) a TE mode is sketched, where the electric field is transverse to the plane of the waveguide, whereas the magnetic field has a component pointing out of the waveguide.

each medium is simply the sum of forward and backward propagating waves, of which one needs to find relative amplitudes. The relative amplitudes follow from boundary condition matching, using continuity conditions on the fields. For a dispersion relation, one solves the Maxwell equations *in absence* of any external driving field, meaning that a non-zero solution can only be found for select combinations of parallel momentum and frequency. This set defines the dispersion relation.

By way of example, in figure 1.2 we plot the dispersion relation and typical mode profiles for the dielectric waveguide chosen throughout this work. The systems consists of a glass substrate, (index 1.515) covered by a polymer (index 1.6), adjacent to air. We assume the high index layer is dispersionless with a fixed refractive index of $n_{SU8} = 1.6$, a substrate with index 1.515 and top medium with index 1. Rather than plotting the dispersion itself, i.e., ω versus k, we calculate mode indices, defined as the ratio of k to ω/c. Figure 1.2 shows mode indices as a function of layer thickness, at a fixed wavelength of 590 nm, which is the operation wavelength of our laser in Chapter 2. The general trend is that for very small thickness, no mode is supported. At cut off (about 250 nm in this case), the waveguide modes have index only just above that of the substrate. For larger thickness the index increases towards that of the polymer, and the mode energy density is more strongly localized in the high index layer. Above 750 nm a next waveguide mode appears. For a thickness of 450 nm, which is the thickness we use throughout the thesis, we can see from the graph that two solutions exist: one solution for TE polarized light and one for TM polarization. TE polarized light has a transverse electric field (figure 1.1a) and therefore experiences different boundary conditions as compared to transverse magnetic (TM) polarized light (figure 1.1). The TE and TM modes have a very similar mode index, and also a very similar distribution of energy density in the waveguide. However, the TE mode has entirely in-plane polarization while the TM mode only has a small in-plane polarized component. While the energy density of the modes is a measure for the overlap with the gain medium, the polarization is important to understand coupling to the particle arrays in our work,

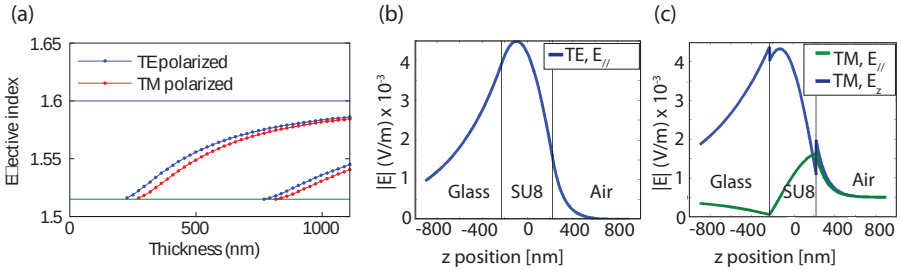

Figure 1.2: In (a) the effective refractive index of a waveguide mode for a slab with no particles is plotted, as a function of layer thickness. We assume n_{glass}=1.515, n_{SU8}=1.6 and n_{air}=1. The blue and green horizontal lines indicate the refractive index of the SU8 and the glass, respectively. From the graph we can see that no modes exist for a thickness below 114 nm below which cut off occurs. Above 114 nm one TE and one TM mode occurs and from a thickness of 770 nm onwards two TE modes exist. In figure (b) and (c) field plots of a TE and a TM mode are given for the in plane and the out of plane electric field component. The x, y and z directions are defined as shown in the inset of figure 1.1b.

owing to the fact that we deal with anisotropic particles. In the work described in this thesis, we deal with TE polarization. For TE polarization, the in plane electric field component is large and has a maximum near the glass/SU8 interface.

1.2.2 Periodic systems

In this section we discuss qualitatively the effects of introducing periodicity in a 2D waveguiding system. A periodic perturbation, such as a particle array, or a perforation of a dielectric layer by holes, will influence the system depending on e.g. the optical properties of the scatterers. First, we discuss the simplified case where a very weak periodic refractive index modulation scatters the waveguide mode but does not significantly change the waveguide mode itself [30]. If the periodic refractive index modulation does not scatter very strongly then the forward and backward propagating modes interact very little with each other, and we can approximate the dispersion of our combined system with a free folded dispersion mode similar to the notion of a free electron dispersion in solid state physics [31]. In this model the particle array creates copies of the dispersion curve at $k+G$, where G is the reciprocal lattice vector $G = n2\pi/d$, with n an integer and d the pitch of the periodicity. Taking into account only the first Brillouin zone, a dispersion diagram results as shown in Figure 1.3(a) for a one-dimensionally periodic system. This type of diagram shows the following essential physics. First, within the 1st Brillouin zone, the dispersion organizes in discrete bands. Second, at special points in the Brillouin zone, notably the Brillouin zone edge and origin, intersections of bands occur. These intersections correspond to Bragg conditions.

The dispersion of a real periodic system will deviate from the presented case of infinitely weak perturbation, for which modes simply fold back and intersect without

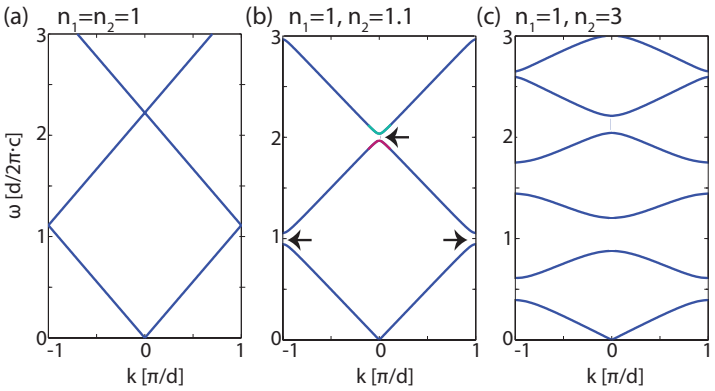

Figure 1.3: Dispersion of a 1D photonic crystal consisting of just 2 slabs with frequency independent refractive indices. In figure (a) both slabs are chosen to have a refractive index equal to 1. In this situation, no reflection can occur and there are no back- and forward traveling waves that can interact with each other. In figure (b) we have chosen $n_1 = 1$ and $n_2 = 1.2$. In this case, back- and forward traveling waves interact with each other, giving rise to stop gaps indicated by the arrows. In figure c) we set $n_1 = 1$ and $n_2 = 3$, where the deviation from the ideal folded dispersion of (a) is even more clear as not only stop gaps open, but the entire dispersion changes.

altering the shape of the dispersion. The deviation occurs most notably at the crossing points of the waveguide modes, which in real systems will be avoided crossings. At these avoided crossings a stop gap is created. The occurrence of a stop gap can be understood by analyzing a 1D periodic system, such as a dielectric mirror under normal incidence shown in figure 1.4b. A dielectric miror, also known as 1D photonic crystal, consists of an infinite stack of lossless dielectric slabs with a thickness comparable to the wavelength of light, which alternate in refractive index. The dispersion of waves in a dielectric mirror can be calculated using the transfer matrix method [32]. Results from this calculation are shown in figure 1.3b and c, and show most of the important features that occur for a real photonic crystal. For a small refractive index contrast of 10%, a small gap opens at the previous intersection points. Both on the upper band edge (colored green) as well as the lower band edge (colored pink in figure 1.3b) a standing wave is created in the crystal. In the first case, the electric field has its peaks in the slabs with the lowest refractive index, as is sketched in figure 1.4b, case (1). For the lower band edge, the opposite is true and the electric field has its peaks at the highest refractive index (case 2).

When the index contrast increases, the stop gap becomes larger and for very large index contrast (figure 1.3c, where $n_1 = 1$ and $n_2 = 3$) the entire shape of the dispersion has changed in the sense that bands are no longer linear over most of the Brillouin zone. When the index contrast is not too large, perturbation theory can be applied to obtain the following expression for the relative size of the lowest stopgap [33]:

$$\frac{\delta\omega}{\omega} \approx \frac{\Delta\epsilon}{\bar{\epsilon}} \cdot \frac{\sin(\pi d/a)}{\pi} \tag{1.2}$$

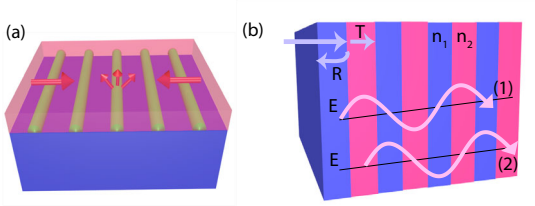

Figure 1.4: In (a) a schematic of a 1D scattering array in a waveguide is shown. Qualitative understanding can be obtained using the 1D photonic crystal (b) as a model for (a). In (a) scattering off a corrugation on the surface occurs, which creates backward and forward propagating modes, whereas in the photonic crystal reflection and transmission occurs at each interface, creating backward and forward propagating modes. In (b) we also show the electric field for light at the upper (case 1) or lower (case 2) band edge. In both cases the mode in the crystal is a standing wave but the maxima of the electric fields are shifted with respect to each other, where the upper band edge has its electric field peaks at the lowest refractive index (n_2).

where $\Delta\epsilon$ is the difference in permittivities, while $\bar{\epsilon}$ is the mean and a is the spatial period. In other words, the relative stop gap size scales directly with the contrast in dielectric constant, while the second term represents the geometry of the layer. As we will see in chapter 3, even though this equation is not derived for scattering in plasmonic systems, the dispersion of a plasmonic system can be qualitatively explained using notions akin to Eq. (1.2).

As outlined above, the systems we study are not one dimensional. Instead we study 2D periodic lattices of scatterers embedded in a waveguide with gain. Dielectric 1D and 2D gratings with gain (see sketch in Fig. 1.4) have already been studied in the limit of very small index contrast well before the field of photonic crystals was born. Indeed, when combined with gain to make a laser, this type of structure is known as distributed feedback (DFB) laser [34–36]. To some degree, the analysis for the 1D system carries over. The first approximation one makes in this case, is that the unperturbed dispersion relation that is folded into the Brillouin zone by the periodicity is no longer the dispersion of free space, but rather the dispersion relation of the waveguide mode. The second complication to deal with, is that for a 2D lattice, the band folding results in a richer band structure. Figure 1.5a shows a repeated zone-scheme view for a square two-dimensionally periodic system. For a 2D square system, we have waveguide mode cones instead of $\omega - k$ dispersion lines intersecting (figure 1.5). In this plot the axes k_x and k_y represent the in plane wavevector components, meaning parallel to the waveguide plane. A horizontal crosscut through the repeated zone scheme dispersion results in isofrequency contours (figure 1.5(b)). Taking a vertical crosscut gives a dispersion band diagram of the 2D system in a specific wave vector slice. Note that in the plotted band diagram (figure 1.5(c), which takes a slice along k_x while keeping $k_y = 0$, parabolas appear that are due to cones centered on reciprocal lattice points in the perpendicular direction (i.e. on the k_y-axis).

In the field of DFB lasers, a powerful analytical tool to describe waves in periodic media was developed by Kogelnik and Shank [37] and is known as "coupled mode

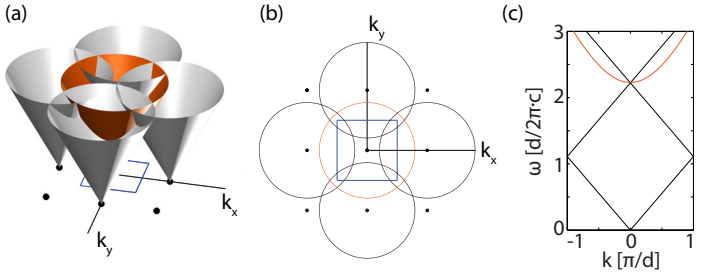

Figure 1.5: (a) Repeated zone scheme representation of the dispersion of a two-dimensionally periodic system. We assume the dispersion of the system without periodic modulation to be a simple cone (orange cone centered on origin). Panel b shows a constant frequency cut taken at $\omega d/2\pi c = 1.5$ (d the lattice pitch). Panel (c) shows a band diagram, i.e., a slice along k_x while keeping $k_y = 0$.

theory". In this model, one essentially describes the physics near a stop gap by taking just a few modes, i. e., one for each band that meets in the band crossing, that in the transverse direction all follow the mode profile of the waveguide, and in the in-plane direction are a simple plane wave. These plane waves are then coupled according to the strength of the periodic dielectric structure, giving rise to stop gaps, exactly as in our sketch of the nearly free photon model. However, beyond the nearly free photon analysis of photonic crystals, in coupled mode theory one can also include temporal and spatial modulations of, for instance, the gain medium.

1.2.3 Interaction of light with plasmon particles

While the previous section dealt essentially with the physics of weakly modulated periodic systems, in this thesis in fact we work with nanoparticles with a plasmonic resonance. The motivation for using metallic nanoparticles is that metallic nanoparticles exhibit resonance behaviour, in contrast to dielectric particles which have a spectrally flat response. The difference originates from how electrons behave in the material. In a dielectric system, electrons can not move freely through the material as they are bound to an atom. For a plasmonic particle, electrons can move freely within the metal, and the effect of an electric field is to slightly displace the free electron cloud relative to the ionic lattice of the particle (figure 1.6b). This creates an effective dipole moment (Fig. 1.6c) $\vec{p} = q \cdot \vec{d}$ and at the same time a linear restoring force, as the electron cloud is pulled back to the positively charged ionic backbone [38]. The motion of electrons therefore behaves like a harmonic oscillator where the light field is the external force. When the incident light is equal to the characteristic frequency of the harmonic oscillator, a resonance occurs for which the created net dipole moment is maximal. Light scattering occurs due to reradiation of incident light due to the collective oscillatory motion of electrons. Thus, at resonance light scattering is maximal.

To illustrate this, we show in figure 1.6 scattering efficiencies calculated using

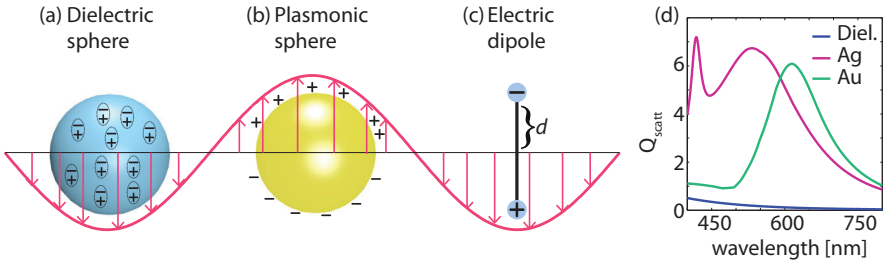

Figure 1.6: A schematic of how dielectric versus plasmonic particles respond to an incoming light field. In dielectric particles electrons can not move freely as opposed to plasmonic particles, where the light field causes changes in the electron density such that an effective dipole moment is generated. The resulting scattering efficiency plotted in (d) shows what effect this has on the scattering strength. The plots are obtained from Mie theory where spheres embedded in glass ($n_{glass} = 1.52$) are used. The dielectric sphere has a refractive index of 2.4.

Mie theory [4] for silver, gold and a dielectric particle, where all three spheres have a diameter of 100 nm and are embedded in glass ($n_{glass} = 1.52$). The graph exemplifies three facts. First, silver and gold particles exhibit a strong dipolar resonance whereas the dielectric sphere does not. Second, the scattering efficiency is much smaller for the dielectric particle (even though we assigned it a high refractive index of 2.4), especially compared to silver and gold when they are at resonance. Indeed, for the metal particles the scattering efficiency, which is defined as the ratio of scattering cross section to geometrical cross section exceeds unity. Third, whereas both gold and silver are plasmonic, their scattering efficiencies show different behaviour, as the resonance of gold is more red-shifted, and the scattering of silver shows an extra peak around 418 nm. The red-shift originates from the different material response function of gold and silver that originates from their different electron density. The extra peak at short wavelengths generally occurs for larger particles, when there is not just a dipolar but also a quadrupolar resonance.

A commonly used approximation to describe scattering by objects much smaller than the wavelength is Rayleigh scattering [4]. If we deal with a nanoparticle that is very small compared to the wavelength, the so-called dipole approximation holds, which states that a scatterer can be viewed as an object that radiates as a dipole, with an induced dipole moment set according to a polarizability $\vec{p} = \alpha \vec{E}_0$. An approximate expression for the polarizability can be found in the so-called quasistatic limit for spheres, meaning that one takes the well known electrostatic (i.e., zero-frequency) polarizability of sphere, but substitutes the frequency dependent permittivities of the metal and its surrounding [1]:

$$\alpha(\omega) = 4\pi\epsilon_m\epsilon_0 r^3 \frac{\epsilon_r - \epsilon_m}{\epsilon_r(\omega) + 2\epsilon_m} \tag{1.3}$$

where ϵ_m is the permittivity of the surrounding medium, and ϵ_r is the permittivity of the metal. A resonance occurs when the real part of ϵ_r, which is negative for metals,

equals $-2\epsilon_m$. From this expression, observables such as the scattering and extinction cross section can be estimated. For instance, the power radiated by a dipole with dipole moment $\vec{p}$ is given by [39]

$$P = \frac{|p|^2}{12\pi\epsilon_0\epsilon_m}\omega k^3 \tag{1.4}$$

with $k = \frac{\omega n}{c}$, with c the speed of light in vacuum and $n = \sqrt{\epsilon_m}$ the refractive index of the medium surrounding the dipole. The ratio of radiated power divided by the incoming energy density gives the scattering cross section (units of area),

$$\sigma_{scatt} = \frac{k^4}{6\pi\epsilon_0^2}|\alpha(\omega)|^2 . \tag{1.5}$$

Likewise, the excintion cross section, which quantifies the sum of scattering and absorption is given by

$$\sigma_{ext} = \frac{k}{\epsilon_0} Im[\alpha(\omega)]. \tag{1.6}$$

From these equations we can observe that the scattered power scales with the size of the scatterer as r^6 whereas the absorbed power scales as r^3. Thus, bigger particles tend to be more efficient scatterers, whereas the interaction of very small particles with light is dominated by absorption. For particles that are between 20 nm and 100 nm in size, scattering is so strong that the quasistatic approximation fails. However, the dipole approximation, and Eqs. (1.5,1.6) for scattering and extinction still hold, provided one adapts the polarizability to contain radiative loss.

While single plasmonic particles interact very strongly with visible light in the sense that their scattering cross section exceeds their geometrical size, the interaction can be enhanced even more when using oligomers [40], or arrays [41–46] of plasmonic scatterers. Plasmonic particles couple to each other through a) far field and b) near field interactions. Near field interactions occur when the particle pitch is smaller than the wavelength of light and occurs because charges of the plasmon particles interact with each other through their quasistatic electric field. This is a phenomenon known in plasmonics as "plasmon hybridization", in analogy to the theory of hybridization of molecular orbitals [47]. Far field interactions are important for the scattering response of plasmon particles when particle array pitches are comparable to the wavelength of light. At these condition grating diffraction can occur, which typically creates strong (Fano) resonances in the far field [48]. Both near- and far field coupling effects in plasmon particle arrays can be qualitatively accounted for in a socalled coupled dipole model [48]. A coupled dipole model assumes that 1) all scatterers are dipole scatterers and 2) the electric field at each dipole is equal to the incident electric field plus the sum of the electric fields generated by all other dipoles in the array. In lattices of identical particles this leads to a renormalization of the polarizability such that when the lattice is irradiated with a parallel wave vector $\vec{k}_{||}$, the induced dipole at site $\vec{R}_n$ of the lattice reads $\vec{p}_n = \vec{p}e^{i\vec{k}_{||}\cdot\vec{R}_n}$, with

$$\vec{p} = \frac{1}{1/\alpha - S(\vec{k}_{||})}\vec{E}^{inc} \tag{1.7}$$

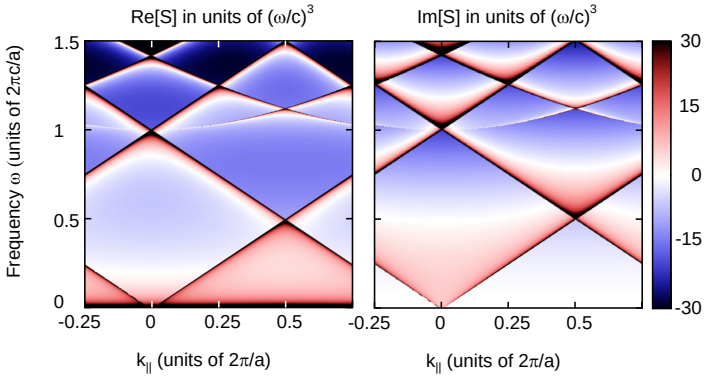

Figure 1.7: In a lattice, the polarizability of each particle is renormalized by a frequency and parallel wave vector dependent term S that is known as lattice sum, which quantifies all dipole-dipole interactions between particles. Shown here is the real and imaginary part of the lattice sum for a square lattice of pitch a, as calculated according to the receipe of de Abajo [48]. Strictly the lattice sum is a tensorial quantity - shown here is the xx-component, with $k_{||}$ taken as the k_x-axis. Note that the lattice sum has very sharp features exactly when frequency and wave vector match the folded dispersion relation of vacuum, or in other words, whenever a grating diffraction condition is matched.

Here the quantity $S(\vec{k}_{||})$ accounts for all the dipole-dipole interactions in the lattice. Generally, this "lattice sum" contains very strong features at diffraction conditions. Figure 1.7 shows such a lattice sum for a square lattice, calculated according to the method of de Abajo [48]. Interestingly, the lattice sum shows very strong, dispersive, features that exactly trace out the repeated zone scheme dispersion of a 2D system in the nearly-free photon approximation. From equation 1.7, we see that the largest response of the particle lattice is achieved when the denominator approaches zero. Thus, the combined effect of the single particle resonance, given by α, and the lattice sum can result in a very large lattice polarization. The combination of strongly plasmonic particles and diffraction resonances has been used in pursuits of high local fields for sensing [44], for outcoupling of light in solid-state lighting [49–51], and in 'quantum plasmonics' pursuits of strong coupling between plasmon modes and emitters [52].

1.3 What is a laser?

LASER is an acronym for Light Amplification by Stimulated Emission of Radiation. To obtain lasing three elements need to be present; 1) a gain medium, 2) an excitation source to excite the gain medium and 3) a cavity for feedback. When this requirement is met, stimulated emission gives rise to lasing. Lasers emit light that can reach very high powers and often exhibit a high degree of spatial and temporal coherence, therefore being monochromatic and very directional. These properties resulted in

lasers becoming one of the most successful inventions of the twentieth century, with applications varying from barcode readers to holography.

Laser research started with the MASER, which is an amplifier for microwave radiation, which Townes and his colleagues demonstrated experimentally in 1954 [53]. In the first MASER, ammonia was used as a gain medium and the resonator supported one resonant mode [54]. These MASERS were very limited in output power and practical applications where limited. Therefore, interest in amplification of radiation was declining. This changed as soon as the concept of amplification of radiation was applied to light, that is, the visible frequency range with wavelengths within the range of 400 nm-700 nm [54–57]. For this, Schawlow and Townes used the concept of the Fabry-Pérot cavity, i.e., a resonator composed of two parallel planar reflective surfaces with a separation of an integer number of wavelengths. Fabry-Pérot lasers are most familiar to everyone, not only because they where the first type of laser introduced in the sixties, but also because they are in general used for explaining basic laser physics concepts. In a Fabry-Pérot laser the cavity consists of two parallel mirrors, where the gain medium is located in between the mirrors. At least one of the mirrors has to be partially transmitting to couple out the laser light. Excitation can be done in various ways but in this thesis we only discuss optical excitation [58]. Excitation creates population inversion of the gain medium.

1.3.1 Spontaneous and stimulated emission

The gain medium of a laser generally consist of a dense ensemble of molecules, atoms, ions, quantum dots, or in case of semiconductor, quantum wells. We consider the gain medium as an ensemble of emitters that are henceforth called "(quantum)emitters". The radiative decay of a quantum emitter from an excited to a ground state can occur through two pathways. First, emitters can spontaneously decay from the excited state to the ground state, randomly emitting a photon in any of the available modes. Second,

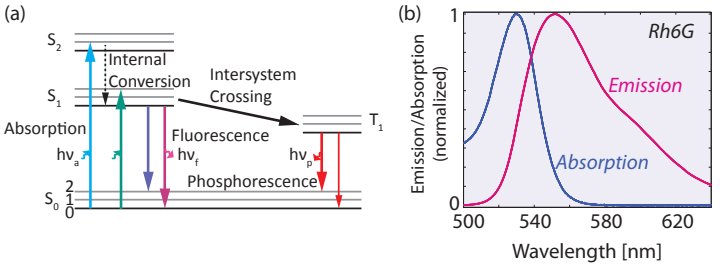

Figure 1.8: In (a) a schematic of a typical Jablonski diagram is shown, depicting optical transitions in a simple three level system. Absorption can cause a transition from S_0 to S_1 or S_2, whereas spontaneous or stimulated emission is generated when the emitter undergoes a transition from S_1 to S_0. Transitions from the triplet state T_1 to S_0 are spin forbidden and are irrelevant in lasing. Figure (b) shows a typical normalized absorption and emission spectrum for rhodamine 6G in methanol [59].

atoms can undergo a stimulated transition, in which the atom is driven by an external wave. The emitted photon will be in the same spatial and temporal mode as the incident photon. Finally, absorption may create a repopulation of the upper state again. These processes are illustrated in the Jablonski diagram for a three level system in figure 1.8 which we obtain from molecular physics. Stimulated emission and spontaneous emission are depicted by the pink and purple arrows, which are transition from level S_1 to S_0. Absorption excites the atom from the ground state S_0 to an excited state S_2, that is for instance a vibrationally excited sublevel of S_1, or even a higher lying electronic state [60]. Note that in molecules all levels have many vibrational/rotational sublevels indicated by the gray lines. Due to these rotational and vibrational sublevels, both the absorption spectrum as well as the spontaneous emission spectrum is broad. This can be seen in the emission/absorption spectrum of Rh6G in figure 1.8. Nonradiative decay is often also present and takes place either through vibrations (heat) or spin conversion. Spin conversion is the proces of flipping a spin, transforming the singlet spin state of the atom to a triplet state which is called intersystem crossing. The transition from T_1 to S_1 is spin forbidden and therefore occurs on a much longer time scale. The emission originating from this transition is called phosphorence instead of fluorescence.

The rates of spontaneous emission, stimulated emission and stimulated absorbtion can be calculated using quantum mechanics, by solving for the coupling between the electronic levels of a quantum emitter, and the quantized electromagnetic field [61, 62]. However, the ratio between spontaneous and stimulated emission and absorption was derived by Einstein before the formulation of quantum mechanics was developed. Einstein considered a so-called "rate-equation" [62]. Suppose that we deal with an ensemble of effective two level systems (levels S_0 and S_1), labelling the populations of the ground and excited state as N_0 and N_1, respectively. According to Einsteins argument, the rate equation must have the following form:

$$\frac{dN_1}{dt} = -N_1 A - N_1 B_{10} \rho(\omega_0) + N_0 B_{01} \rho(\omega_0) \tag{1.8}$$

where $\rho(\omega_0)$ is the energy density of the electromagnetic field at the emiter, as one would supply, for instance, by external illumination. A, B_{10} and B_{01} are constants known as the Einstein coefficients. The first term on the right hand side represents decay without any external field, while the other two terms represent population decay, respectively population growth in proportion to the surrounding energy density. To be able to relate the A and B coefficients, Einstein considered the ensemble of emitters in thermal equilibrium with its environment. The energy density (density of electromagnetic energy per unit volume, and per unit of angular frequency) is given by the well known expression proposed by Planck in 1900

$$\rho(\omega) = \frac{\hbar}{\pi^2 c^3} \frac{\omega^3}{e^{\hbar\omega / k_B T} - 1}. \tag{1.9}$$

where T is the temperature. At thermal equilibrium equilibrum, we can state the following

1. The population of each level is time-independent, $\frac{dN_1}{dt} = 0$. Rewriting equation (1.8) gives an expression for the energy density in terms of the Einstein coefficients,
$$\rho(\omega_0) = \frac{A}{(N_0/N_1)B_{01} - B_{10}} \tag{1.10}$$
2. The ratio of populations in the excited state and the ground state satisfy the Boltzmann distribution
$$\frac{N_0}{N_1} = \frac{e^{-E_0/k_BT}}{e^{-E_1/k_BT}} = e^{\hbar\omega_0/k_BT} \tag{1.11}$$

Combining these two results with Plancks law (Eq. 1.9) results in the following relations
$$B_{10} = \frac{\pi^2 c^3}{\hbar\omega^3} A \tag{1.12}$$
and
$$B_{01} = B_{10}. \tag{1.13}$$

Note how by using thermal equilibrium arguments, Einstein obtained a temperature-independent relation between coefficients. The conclusions are two-fold. First, since B_{01} and B_{10} are identical, the rates for absorption and stimulated emission are identical for a two-level system. Indeed, these coefficients can be calculated by quantum-mechanical perturbation theory where the optical field is treated entirely classically. This perturbation theory analysis results in a product of the intensity of the applied field, and a wavefunction dependent prefactor that quantifies the oscillator strength of the transition. The Einstein B coefficient can therefore also be cast in the form of an oscillator strength or an absorption/stimulated emission cross section. The second important conclusion that Einstein derived is that thermal equilibrium demands non-zero A, meaning that it demands population decay even in absence of any field. This is known as spontaneous emission.

1.3.2 Rate equations and gain

Lasing can occur if an ensemble of emitters is pumped to the excited state, and is coupled to an optical mode that provides feedback. In the simplest implementation this would be the "cavity" mode of a Fabry-Pérot laser cavity. Using the concepts of spontaneous and stimulated emission, we can derive a simple rate equation model that demonstrates important characteristics of lasing that are used in experiments to prove lasing [63]. To do this, first we rewrite equation (1.8) to a simplified rate equation for the excited state population N_1 of a gain medium in a laser. Generally, to obtain lasing one has to decouple the levels used for pumping, from the levels on which the system lases. Hence, one commonly derives lasing assuming an ensemble of N molecules that each are a four-level system, not a two-level system. In practice, one typically pumps from the vibrational ground state of the electronic ground state manifold S_0,

to some higher vibrationally excited state in the S_1 manifold. Lasing typically occurs from the vibrational ground state of S_1 to some vibrational level in the S_0 manifold, i.e., at some wavelength redshifted from the pump transition. For typical gain media one can use a separation of time scales, as vibrational relaxation is fast (picosecond time scales), while emission is slow (nanoseconds). Under these conditions, only the population N_0 of the lower level of the pump transition, and the population N_1 of the upper level of the lasing transition are relevant. Note that $N_0 + N_1 = N$. One can derive a rate equation for N_1:

$$\frac{dN_1}{dt} = r - \phi C N_1 - \Gamma N_1. \tag{1.14}$$

The absorption term has been replaced by a constant rate r, representing a constant pump rate of the gain medium to the excited state. Note that here we do not ask how this constant rate r is achieved. In our own experiments, as in many dye lasers, this is done by optically pumping molecules in the gain medium to higher vibrationally excited state (labelled S_2) in the S_1 band of Figure 1.8 using a pump laser that is significantly blue shifted from the lasing wavelength. The state that is meant with 'excited state population' is the vibrational ground state S_1 of the electronically first excited state, to which excited emitters quickly relax. The second term represents stimulated emission in proportion to the number of photons ϕ in the cavity mode, thereby being equivalent to $N_1 B_{01} \rho(\omega_0)$ in Eq. (1.8). The third term represents spontaneous emission, where Γ is the spontaneous decay rate. For the number of photons ϕ in the cavity, a complementary equation can be written

$$\frac{d\phi}{dt} = -\gamma_c \phi + \phi C N_1 + \beta \Gamma N_1 \tag{1.15}$$

where we include radiation loss from the cavity by including the term γ_c which represents the cavity decay rate. The constant β is included to represent the probability that spontaneous emission actually contributes to the cavity mode. Generally, this parameter that is famously known as "spontaneous emission beta-factor" is small. For instance if one considers a typical macroscopic laser resonator, the cavity mode is defined by mirrors at spacings of (tens of) centimeters, yet with a mode diameter of at best millimeters. Hence a solid-angle estimate immediately shows that an overwhelming fraction (1-β) of the isotropically radiated spontaneous emission will not contribute to the cavity [63].

These two rate equations are the starting point of any treatise on lasers, as they incorporate the basic feature of a lasing threshold, where below threshold emission is dominated by spontaneous emission into all directions, while above threshold stimulated emission ensures strong emission into the cavity mode. We can see how threshold behaviour arises from these equations by looking at steady state solutions. In steady state, we have $r = \phi C N_1 + \Gamma N_1$ and $\gamma_c \phi = \phi C N_1 + \beta \Gamma N_1$ which we can rewrite to

$$N_1 = \frac{r}{\phi C + \Gamma} \tag{1.16}$$

and

$$\phi = \frac{N_1 \beta \Gamma}{\gamma_c - N_1 C}. \tag{1.17}$$

First, below threshold, i.e., when the pump rate is small, we have $\phi C \ll \Gamma$ and $N_1 = \frac{r}{\Gamma}$. Thus, for low pump powers the number of emitters in the excited state increases linearly with pump power and is limited by spontaneous emission. Very different behavior is obtained for pump rates when a threshold is reached that is evident in Eq. (1.17), when N_1 approaches $\frac{\gamma_c}{C} = N_{th}$, at which point the number of photons in the cavity rapidly increases. When this threshold is reached, requiring a a pump rate exceeding a threshold value of r_{th}, population decays predominantly by stimulated emission in the cavity mode. These simplified rate equations for a gain medium in a resonator thus predict one canonical behavior of a laser, namely a laser threshold, below which the emission of the system is simply spontaneous emission (as if the resonator were not there), and above which emission is dominated by stimulated emission into the cavity mode. The threshold is reached when the round trip gain due to stimulated emission exceeds the round trip loss of the cavity. Both above and below threshold the output power is linear in pump rate, however with very different slopes. The sharpness of the transition between the two regimes is strongly dependent on the value of β. Since most lasers have very small β-factors, the threshold is generally easily observable as a kink in the output intensity versus input pump power [63]. Moreover, the fact that above threshold almost all emission is stimulated emission into the cavity mode is generally observable as a spectral narrowing and emergence of spatial coherence. This type of rate equation analysis is naturally just the starting point for understanding lasers, a full understanding of which requires further theory for, e.g., the commonly observed spectral narrowing, emergence of spatial coherence, photon statistics, and the spatial and temporal behavior in presence of multiple cavity modes that compete for gain.

1.4 Plasmonic lasers

1.4.1 Proposed and reported plasmon lasers

Plasmon lasers have been a topic of interest ever since the prediction by Bergman and Stockmann in 2003 [27] that plasmons can operate in the same way as photons regarding the lasing process. They posed the concept of Surface Plasmon Amplification by Stimulated Emission of Radiation, or spaser. Spasers are the plasmonic counterpart of lasers. Just as is the case for a laser, a spaser consists of three essential components; a gain medium, a resonator and an external excitation source. The difference with a laser is that the resonator is a cavity for Surface Plasmon Polaritons (SPP's) instead of photons. Because plasmons are bosons, they can accumulate in one mode just as photons, as is required to get stimulated emission. According to Stockman [27, 64], the spaser operates as a quantum amplifier of the deeply subdiffractive confined plasmon resonances that he envisions exist for metal particles in the "quasi-static" limit ($c = \infty$ or size$\ll \lambda$ limit). In this paradigm, a spaser would not create any radiative output, since

radiation loss is assumed negligible. This should be contrasted to the fact that actual plasmon particles usually have sizes exceeding $\lambda/2\pi$, meaning that they do show strong radiative loss. If lasing would occur with such plasmon particles, the resulting laser could also be viewed as a "scattering laser" as proposed by Savels and Lagendijk [28]. In their paradigm, the smallest possible laser would consist of three strong scatterers (resonant scattering cross section is $3\lambda^2/2\pi$, and a gain medium consisting of just one or a few atoms).

There are many approaches to using plasmonics in lasers [65]. A general problem in such lasers is that because plasmonic systems are so lossy, spasers need a substantial amount of gain. To obtain more gain, the round-trip gain can be increased either by using an emitter with a large gain coefficient, or by increasing the cavity length while reducing the confinement in the metal. In the first claimed demonstration of a spaser by Noginov et al [66] the SPP resonator consisted of a gold nanosphere with a diameter of only 14 nm for which the quality factor of the SPP is only 14.8. Noginov et al. claimed spectral narrowing and threshold behavior for such spheres, surrounded by a very dense shell of organic dye. It should be noted that to date the observation by Noginov has not been reproduced by any group, and is disputed on basis of theoretical and experimental considerations. Demands on gain are eleviated for the so-called hybrid photonic-plasmonic mode spasers with slightly weaker confinement and higher Q that were pioneered at Berkeley [67, 68]. In this type of laser one has typically used a mode that is tightly confined between a thin, flat, metal film, and a nanowire or nanoplatelet that provides both gain and a high refractive index. Between the high index gain medium and the plasmonic metal there is a spacer layer. In this type of configuration a hybrid mode between the plasmonic waveguide mode and the photonic nanowire mode is formed [67, 69, 70]. The EM fields of this hybrid plasmon mode concentrate in the spacer layer, instead of in the lossy metal, making even room temperature lasing operation possible [68]. Many demonstrations of spasers have utilized the hybrid plasmon laser approach in which a semiconductor gain material, a spacer layer and a waveguide are present [70–75]. More recently, non-hybrid subdiffractive plasmon mode lasing has also been demonstrated [76]. Another approach in which lasing was demonstrated used top-down fabrication of metal coated semiconductor lasers, where the gain medium (typically a III-V semiconductor) is clad by a metal to confine the laser mode volume [77–79]. Although for such systems lasing does not occur on a pure plasmonic mode, plasmonic effects cause high Purcell enhancements that in turn result in a very high β factor. In this context, an almost thresholdless laser has been demonstrated [80]. In this thesis we study diffractive plasmon particle array lasers that display distributed feedback lasing. The first diffractive metal particle array laser was demonstrated by Stehr et al. in 2003 [81]. Since then it has been shown that bow ties placed in a diffractive array embedded in a low index polymer with gain, show lasing, supposedly due to spaser action of the individual bowties [82, 83]. Also the inverse geometry, i.e., metal films with hole arrays that provide scattering has been shown to lase [84, 85].

1.4.2 How to recognize lasing in plasmonic systems

When claiming lasing emission in any type of photonic structure, two good questions to ask are, first, how one recognizes lasing, and second, if any characteristic of the laser is particular for the specific type of photonic structure. Applied to plasmonics one can hence ask: how does one recognize a plasmonic laser, and how does the plasmonic nature of the resonator enter the physics. Generally, when building a laser one first attempts to confirm threshold behavior in intensity. Next, laser emission is generally characterized by a high degree of spatial and temporal coherence. Temporal coherence is visible in the emission spectrum, as a distinct characteristic linewidth narrowing occurs when passing the lasing threshold. Spatial coherence can be investigated by observing interference effects of the direct laser emission, e.g. by performing a double slit experiment [86] or looking at intensity correlations in real space images. Finally it is also possible to investigate the photon statistics of the light output. For some plasmonic lasers these criteria will be difficult to apply. For instance, since plasmon resonators generally have quality factors between 5 and 50, the underlying mode need not be narrow in frequency, which could limit the line narrowing. Also, the high Purcell factors of plasmons can result in very high beta factors, meaning that one can obtain lasing without a threshold [80]. If a resonator is deeply subwavelength, laser output into the far field need not be directional. In this thesis we will study extended plasmon particle systems, that clearly evidence lasing on the criteria of threshold, line narrowing and spatial coherence, while photon statistics is not measurable for practical reasons. The remaining major debate for any plasmon laser is in how far the mode that lases is actually 'plasmonics', and if this means that the physics of the laser is different from that of a dielectric counterpart. This thesis will be devoted to unravelling if, and if so, how, the particle plasmon resonance is relevant for the lasing characteristics of our plasmonic counterpart of traditional dielectric distributed feedback lasers.

1.5 Outline of the thesis

In this thesis we study lasing in diffractive plasmon particle array systems. We utilize plasmonic particles as strong point dipole scatterers in a distributed feedback configuration. Using basic fluorescence microscopy we are able to demonstrate lasing and map dispersion diagrams. From the dispersion diagram we show how plasmonics changes the waveguide mode as a result of the huge scattering strength as compared to standard DFB lasers. In chapter 2, we prove lasing in simple square lattices of gold and silver disks and show how the stop gap on which it operates correlates with the pitch of the lattice. In addition, we perform a comparison between three different materials (silver, gold and titanium dioxide) and show that due to its strong scattering strength silver modifies the band structure noticeably, yet due to its loss simultaneously exhibits a much higher threshold with respect to the dielectric titanium dioxide system. In chapter 3 we explore the effect of increasing scattering strenght in much more depth. Whereas in chapter 2 the resonance frequency of the silver disk is quite stongly red shifted compared to the emission bandwidth of our dye, in chapter

3 we use a FRET-pair of dyes to obtain a gain window that lies exactly in the range of the resonance frequency of 100 nm diameter silver disks. We unravel from the dispersion diagram how the dispersion diagram changes as a function of detuning of the plasmon resonance with respect to the emission frequency of the dye. In chapter 4 we study lasing in randomized lattices of silver particles. The main focus is to answer the question: how much order do you need to obtain lasing? From the results we find that lasing on the second order Bragg diffraction on which Chapters 2 and 3 rely is very robust against introducing disorder. In addition, we use speckle intensity statistics to real-space fluorescence images and with this introduce a method to distinguish spontaneous emission from lasing. Finally, in chapter 5 we study an intermediate case between periodic and random systems and study quasi- and aperiodic lasers. We use deterministic generation sequences to generate lattices with a fourier spectrum that varies from discrete to increasingly continuous. We show that when the underlying particle pitch is the same as before, outcoupling of laser emission is determined by the underlying lattice, whereas the lasing frequency remains fixed at the 2nd order Bragg condition. Also new lasing conditions arise from diffractive resonances that are peculiar to aperiodic systems.

References

[1] J. D. Jackson, *Classical Electrodynamics*, Wiley, New York, 1999.

[2] D. K. Gramotnev and S. I. Bozhevolnyi, *Plasmonics beyond the diffraction limit*, Nature Photon. **4**, 83 (2010).

[3] W. L. Barnes, A. Dereux, and T. W. Ebbesen, *Surface plasmon subwavelength optics*, Nature **424**, 824 (2003).

[4] C. F. Bohren and D. R. Huffman, *Absorption and Scattering of Light by Small Particles*, Wiley-VCH Verlag GmbH, 1998.

[5] P. L. Stiles, J. A. Dieringer, N. C. Shah, and R. R. Van Duyne, *Surface-enhanced Raman spectroscopy*, Annu. Rev. Anal. Chem. **1**, 601 (2008).

[6] C. D'Andrea, J. Bochterle, A. Toma, C. Huck, F. Neubrech, E. Messina, B. Fazio, O. M. Marago, E. Di Fabrizio, M. L. de la Chapelle, P. G. Gucciardi, and A. Pucci, *Optical nanoantennas for multiband surface-enhanced infrared and Raman spectroscopy*, ACS Nano **7**, 3522 (2013).

[7] F. Le, D. W. Brandl, Y. A. Urzhumov, H. Wang, J. Kundu, N. J. Halas, J. Aizpurua, and P. Nordlander, *Metallic nanoparticle arrays: A common substrate for both -enhanced Raman scattering and -enhanced infrared absorption*, ACS Nano **2**, 707 (2008).

[8] J. N. Anker, W. P. Hall, O. Lyandres, N. C. Shah, J. Zhao, and R. P. Van Duyne, *Biosensing with plasmonic nanosensors*, Nat. Mater. **7**, 442 (2008).

[9] M. E. Stewart, C. R. Anderton, L. B. Thompson, J. Maria, S. K. Gray, J. A. Rogers, and R. G. Nuzzo, *Nanostructured plasmonic sensors*, Chem. Rev. **108**, 494 (2008).

[10] S. V. Boriskina and L. Dal Negro, *Sensitive label-free biosensing using critical modes in aperiodic photonic structures*, Opt. Express **16**, 12511 (2008).

[11] K.-S. Lee and M. A. El-Sayed, *Gold and silver nanoparticles in sensing and imaging: Sensitivity of plasmon response to size, shape, and metal composition*, J. Phys. Chem. B **110**, 19220 (2006).

[12] A. V. Kabashin, P. Evans, S. Pastkovsky, W. Hendren, G. A. Wurtz, R. Atkinson, R. Pollard, V. A. Podolskiy, and A. V. Zayats, *Plasmonic nanorod metamaterials for biosensing*, Nat. Mater. **8**, 867 (2009).

[13] S. Mokkapati and K. R. Catchpole, *Nanophotonic light trapping in solar cells*, J. Appl. Phys. **112**, 101101 (2012).

[14] H. A. Atwater and A. Polman, *Plasmonics for improved photovoltaic devices*, Nat. Mater. **9**, 205 (2010).

[15] M. L. Brongersma, Y. Cui, and S. Fan, *Light management for photovoltaics using high-index nanostructures*, Nat. Mater. **13**, 451 (2014).

[16] K. R. Catchpole and A. Polman, *Plasmonic solar cells*, Opt. Express **16**, 21793 (2008).
[17] L. Novotny and B. Hecht, *Principles of Nano-Optics (p. 374)*, Cambridge University Press, 2007.
[18] P. R. West, S. Ishii, G. V. Naik, N. K. Emani, V. M. Shalaev, and A. Boltasseva, *Searching for better plasmonic materials*, Laser Photonics Rev. **4**, 795 (2010).
[19] A. Boltasseva and H. A. Atwater, *Low-loss plasmonic metamaterials*, Science **331**, 290 (2011).
[20] G. V. Naik, J. Kim, and A. Boltasseva, *Oxides and nitrides as alternative plasmonic materials in the optical range [invited]*, Opt. Mater. Express **1**, 1090 (2011).
[21] A. Paul, Y.-R. Zhen, Y. Wang, W.-S. Chang, Y. Xia, P. Nordlander, and S. Link, *Dye-assisted gain of strongly confined surface plasmon polaritons in silver nanowires*, Nano Lett. **14**, 3628 (2014).
[22] M. Ambati, S. H. Nam, E. Ulin-Avila, D. A. Genov, G. Bartal, and X. Zhang, *Observation of stimulated emission of surface plasmon polaritons*, Nano Lett. **8**, 3998 (2008).
[23] J. Grandidier, G. C. D. Francs, S. Massenot, A. Bouhelier, L. Markey, J. C. Weeber, C. Finot, and A. Dereux, *Gain-assisted propagation in a plasmonic waveguide at telecom wavelength*, Nano Lett. **9**, 2935 (2009).
[24] M. C. Gather, K. Meerholz, N. Danz, and K. Leosson, *Net optical gain in a plasmonic waveguide embedded in a fluorescent polymer*, Nat. Photonics **4**, 457 (2010).
[25] N. P. de Leon, B. J. Shields, C. L. Yu, D. E. Englund, A. V. Akimov, M. D. Lukin, and H. Park, *Tailoring light-matter interaction with a nanoscale plasmon resonator*, Phys. Rev. Lett. **108**, 226803 (2012).
[26] J. Seidel, S. Grafstrom, and L. Eng, *Stimulated emission of surface plasmons at the interface between a silver film and an optically pumped dye solution*, Phys. Rev. Lett. **94**, 177401 (2005).
[27] D. J. Bergman and M. I. Stockman, *Surface plasmon amplification by stimulated emission of radiation: Quantum generation of coherent plasmons in nanosystems*, Phys. Rev. Lett **90**, 027402 (2003).
[28] T. Savels, A. P. Mosk, and A. Lagendijk, *Gain narrowing in few-atom systems*, Phys. Rev. Lett. **98**, 103601 (2007).
[29] H. P. Urbach and G. L. J. A. Rikken, *Spontaneous emission from a dielectric slab*, Phys. Rev. A **57**, 3913 (1998).
[30] J. D. Joannopoulos, S. G. Johnson, J. N. Winn, and R. D. Meade, *Photonic Crystals, Molding the flow of light*, Princeton University Press, 2008.
[31] C. Kittel, *Introduction to Solid State Physics*, Wiley, 2005.
[32] C. C. Katsidis and D. I. Siapkas, *General transfer-matrix method for optical multilayer systems with coherent, partially coherent, and incoherent interference*, Appl. Opt. **41**, 3978 (2002).
[33] C. M. Soukoulis, *Photonic Crystals and Light Localization in the 21st Century (p. 51)*, Kluwer, Dordrecht, 2008.
[34] G. A. Turnbull, P. Andrew, W. L. Barnes, and I. D. W. Samuel, *Photonic mode dispersion of a two-dimensional distributed feedback polymer laser*, Phys. Rev. B **67**, 165107 (2003).
[35] C. Kallinger, M. Hilmer, A. Haugeneder, M. Perner, W. Spirkl, U. Lemmer, J. Feldmann, U. Scherf, K. Mullen, A. Gombert, and V. Wittwer, *A flexible conjugated polymer laser*, Adv. Mater. **10**, 3913 (1998).
[36] I. D. W. Samuel and G. A. Turnbull, *Organic semiconductor lasers*, Chem. Rev. **107**, 1272 (2007).
[37] H. Kogelnik and C. Shank, *Stimulated emission in a periodic structure*, Appl. Phys. Lett.

18, 152 (1971).

[38] P. K. Jain, S. Eustis, and M. A. El-Sayed, *Plasmon coupling in nanorod assemblies: Optical absorption, discrete dipole approximation simulation, and exciton-coupling model*, J. Phys. Chem. B **110**, 18243 (2006).

[39] L. Novotny and B. Hecht, *Principles of Nano-Optics (p. 239)*, Cambridge University Press, 2007.

[40] M. Hentschel, M. Saliba, R. Vogelgesang, H. Giessen, A. P. Alivisatos, and N. Liu, *Transition from isolated to collective modes in plasmonic oligomers*, Nano Lett. **10**, 2721 (2010).

[41] A. A. Penzkofer and Y. Lu, *Fluorescence quenching of rhodamine 6g in methanol at high concentration*, Chem. Phys. **103**, 399 (1986).

[42] L. Zhao, K. L. Kelly, and G. C. Schatz, *The extinction spectra of silver nanoparticle arrays: Influence of array structure on plasmon resonance wavelength and width*, J. Phys. Chem. B **107**, 7343 (2003).

[43] A. Bouhelier, R. Bachelot, J. Im, G. Wiederrecht, G. Lerondel, S. Kostcheev, and P. Royer, *Electromagnetic interactions in plasmonic nanoparticle arrays*, J. Phys. Chem. B **109**, 3195 (2005).

[44] C. L. Haynes, A. D. McFarland, L. L. Zhao, R. P. Van Duyne, G. C. Schatz, L. Gunnarsson, J. Prikulis, B. Kasemo, and M. Käll, *Nanoparticle optics: The importance of radiative dipole coupling in two-dimensional nanoparticle arrays*, J. Phys. Chem. B **107**, 7337 (2003).

[45] A. G. Nikitin, A. V. Kabashin, and H. Dallaporta, *Plasmonic resonances in diffractive arrays of gold nanoantennas: near and far field effects*, Opt. Express **20**, 27941 (2012).

[46] L. A. Sweatlock, S. A. Maier, H. A. Atwater, J. J. Penninkhof, and A. Polman, *Highly confined electromagnetic fields in arrays of strongly coupled ag nanoparticles*, Phys. Rev. B **71**, 235408 (2005).

[47] E. Prodan, C. Radloff, N. Halas, and P. Nordlander, *A hybridization model for the plasmon response of complex nanostructures*, Science **302**, 419 (2003).

[48] F. J. García de Abajo, *Colloquium: Light scattering by particle and hole arrays*, Rev. Mod. Phys. **79**, 1267 (2007).

[49] G. Vecchi, V. Giannini, and J. Gómez Rivas, *Shaping the fluorescent emission by lattice resonances in plasmonic crystals of nanoantennas*, Phys. Rev. Lett. **102**, 146807 (2009).

[50] G. Lozano, D. J. Louwers, S. R. K. Rodriguez, S. Murai, O. T. A. Jansen, M. A. Verschuuren, and J. Gómez Rivas, *Plasmonics for solid-state lighting: enhanced excitation and directional emission of highly efficient light sources*, Light. Sci. Appl. **2**, e66 (2013).

[51] S. R. K. Rodriguez, S. Murai, M. A. Verschuuren, and J. Gómez Rivas, *Light-emitting waveguide-plasmon polaritons*, Phys. Rev. Lett. **109**, 166803 (2012).

[52] L. Shi, T. K. Hakala, H. T. Rekola, J. P. Martikainen, R. J. Moerland, and P. Torma, *Spatial coherence properties of organic molecules coupled to plasmonic surface lattice resonances in the weak and strong coupling regimes*, Phys. Rev. Lett. **112**, 153002 (2014).

[53] B. A. Lengyel, *Evolution of masers and lasers*, American Journal of Physics **34**, 903 (1966).

[54] A. L. Schawlow and C. H. Townes, *Infrared and optical masers*, Phys. Rev. **112**, 1940 (1958).

[55] L. Hoddeson, *The laser in America*, Minerva **32**, 228 (1994).

[56] J. Hecht, *Short history of laser development*, Opt. Eng. **49**, 091002 (2010).

[57] A. J. Gross and T. R. Herrmann, *History of lasers*, World journal of urology **25**, 217 (2007).

[58] W. T. Silfvast, *Laser Fundamentals*, Cambridge University Press, New York, 2004.

[59] J. Dixon, M. Taniguchi, and J. Lindsey, *PhotochemCAD 2: A refined program with accompanying spectral databases for photochemical calculations*, Photochem. Photobiol. **81**, 212 (2005).
[60] J. R. Lakowicz, *Principles of Fluorescence Spectroscopy*, Springer, 2006.
[61] D. Griffiths, *Introduction to Quantum Mechanics*, Prentice Hall, 1994.
[62] R. Loudon, *The Quantum Theory of Light*, Oxford Science Publications, 1983.
[63] A. E. Siegman, *Lasers*, University Science Books, 1986.
[64] M. I. Stockman, *The spaser as a nanoscale quantum generator and ultrafast amplifier*, J. Opt. **12**, 024004 (2010).
[65] M. T. Hill and M. C. Gather, *Advances in small lasers*, Nat. Photonics **8**, 908 (2014).
[66] M. A. Noginov, G. Zhu, A. M. Belgrave, R. Bakker, V. M. Shalaev, E. E. Narimanov, S. Stout, E. Herz, T. Suteewong, and U. Wiesner, *Demonstration of a spaser-based nanolaser*, Nature **460**, 1110 (2009).
[67] R. F. Oulton, V. J. Sorger, T. Zentgraf, R.-M. Ma, C. Gladden, L. Dai, G. Bartal, and X. Zhang, *Plasmon lasers at deep subwavelength scale*, Nature **461**, 629 (2009).
[68] Y.-J. Lu, J. Kim, H.-Y. Chen, C. Wu, N. Dabidian, C. E. Sanders, C.-Y. Wang, M.-Y. Lu, B.-H. Li, X. Qiu, W.-H. Chang, L.-J. Chen, G. Shvets, C.-K. Shih, and S. Gwo, *Plasmonic nanolaser using epitaxially grown silver film*, Science **337**, 450 (2012).
[69] V. J. Sorger, R. F. Oulton, R.-M. Ma, and X. Zhang, *Toward integrated plasmonic circuits*, MRS Bull. **37**, 728 (2012).
[70] R.-M. Ma, R. F. Oulton, V. J. Sorger, G. Bartal, and X. Zhang, *Room-temperature sub-diffraction-limited plasmon laser by total internal reflection*, Nat. Mater. **10**, 110 (2011).
[71] C.-Y. Wu, C.-T. Kuo, C.-Y. Wang, C.-L. He, M.-H. Lin, H. Ahn, and S. Gwo, *Plasmonic green nanolaser based on a metal-oxide-semiconductor structure*, Nano Lett. **11**, 4256 (2011).
[72] T.-T. Wu, S.-H. Wu, T.-C. Lu, and S.-C. Wang, *GaN-based high contrast grating surface-emitting lasers*, Appl. Phys. Lett. **102**, 081111 (2013).
[73] G. Y. Li, X. F. Liu, X. Wang, Y. W. Yuan, T. C. Sum, and Q. H. Xiong, *Purified plasmonic lasing with strong polarization selectivity by reflection*, Opt. Express **23**, 15657 (2015).
[74] R. Perahia, T. P. M. Alegre, A. H. Safavi-Naeini, and O. Painter, *Surface-plasmon mode hybridization in subwavelength microdisk lasers*, Appl. Phys. Lett. **95**, 201114 (2009).
[75] S.-H. Kwon, J.-H. Kang, C. Seassal, S.-K. Kim, P. Regreny, Y.-H. Lee, C. M. Lieber, and H.-G. Park, *Subwavelength plasmonic lasing from a semiconductor nanodisk with silver nanopan cavity*, Nano Lett. **10**, 3679 (2010).
[76] J. F. Ho, J. Tatebayashi, S. Sergent, C. F. Fong, S. Iwamoto, and Y. Arakawa, *Low-threshold near-infrared GaAs-AlGaAs core-shell nanowire plasmon laser*, ACS Photonics **2**, 165 (2015).
[77] Y. C. Hsu, K. P. Sou, S. P. Chang, K. S. Hsu, M. H. Shih, H. C. Kuo, Y. J. Cheng, and C. Y. Chang, *Room temperature ultraviolet GaN metal-coated nanorod laser*, Appl. Phys. Lett. **103**, 191102 (2013).
[78] M. T. Hill, Y.-S. Oei, B. Smalbrugge, Y. Zhu, T. De Vries, P. J. Van Veldhoven, F. W. M. Van Otten, T. J. Eijkemans, J. P. Turkiewicz, H. De Waardt, E. J. Geluk, S.-H. Kwon, Y.-H. Lee, R. Notzel, and M. K. Smit, *Lasing in metallic-coated nanocavities*, Nat. Photonics **1**, 589 (2007).
[79] M. T. Hill, M. Marell, E. S. P. Leong, B. Smalbrugge, Y. Zhu, M. Sun, P. J. van Veldhoven, E. J. Geluk, F. Karouta, Y.-S. Oei, R. Notzel, C.-Z. Ning, and M. K. Smit, *Lasing in metal-insulator-metal sub-wavelength plasmonic waveguides*, Opt. Express **17**, 11107 (2009).

[80] M. Khajavikhan, A. Simic, M. Katz, J. H. Lee, B. Slutsky, A. Mizrahi, V. Lomakin, and Y. Fainman, *Thresholdless nanoscale coaxial lasers*, Nature **482**, 204 (2012).

[81] J. Stehr, J. Crewett, F. Schindler, R. Sperling, G. von Plessen, U. Lemmer, J. M. Lupton, T. A. Klar, J. Feldmann, A. W. Holleitner, M. Forster, and U. Scherf, *A low threshold polymer laser based on metallic nanoparticle gratings*, Adv. Mater. **15**, 1726 (2003).

[82] J. Y. Suh, C. H. Kim, W. Zhou, M. D. Huntington, D. T. Co, M. R. Wasielewski, and T. W. Odom, *Plasmonic bowtie nanolaser arrays*, Nano Lett. **12**, 5769 (2012).

[83] W. Zhou, M. Dridi, J. Y. Suh, C. H. Kim, D. T. Co, M. R. Wasielewski, G. C. Schatz, and T. W. Odom, *Lasing action in strongly coupled plasmonic nanocavity arrays*, Nat. Nanotechnol. **8**, 506 (2013).

[84] F. van Beijnum, P. J. van Veldhoven, E. J. Geluk, M. J. A. de Dood, G. W. 't Hooft, and M. P. van Exter, *Surface plasmon lasing observed in metal hole arrays*, Phys. Rev. Lett. **110**, 206802 (2013).

[85] X. G. Meng, J. J. Liu, A. V. Kildishev, and V. M. Shalaev, *Highly directional spaser array for the red wavelength region*, Laser Photonics Rev. **8**, 896 (2014).

[86] B. Redding, M. A. Choma, and H. Cao, *Spatial coherence of random laser emission*, Opt. Lett. **36**, 3404 (2011).

2

Lasing at the band edges of plasmonic lattices

We report room temperature lasing in two-dimensional diffractive lattices of silver and gold plasmon particle arrays embedded in a dye-doped polymer that acts both as waveguide and gain medium. As compared to conventional dielectric distributed feedback lasers, a central question is how the underlying band structure from which lasing emerges is modified by both the much stronger scattering and the disadvantageous loss of metal. We use spectrally resolved back-focal plane imaging to measure the wavelength- and angle dependence of emission below and above threshold, thereby mapping the band structure. We find that for silver particles, the band structure is strongly modified compared to dielectric reference DFB lasers, since the strong scattering gives large stop gaps. In contrast, gold particles scatter weakly and absorb strongly, so that thresholds are higher, but the band structure is not strongly modified. The experimental findings are supported by finite element and fourier modal method calculations of the single particle scattering strength and lattice extinction.

2.1 Introduction

In the past decade, plasmonics has become a very active field of research within optics owing to the unique opportunities for broadband strongly enhanced light matter interaction in precisely fabricated metal nanostructures [1]. Enhanced light matter

interaction arises from the fact that plasmons, as hybrids of photons and charge density oscillations, are not restricted to the conventional diffraction limit. In addition, it has been shown that plasmon particles can enhance emission decay rates of fluorophores due to high Purcell factors over large bandwidths [2–6]. In fact, for low quantum efficiency fluorphores up to 1000-fold brightness enhancements per molecule have been reported near bow tie antennas [3–8]. Huge field enhancements (of order 10^3 in electric field) have further been evidenced in surface enhanced Raman and surface enhanced infrared spectroscopy [9, 10]. Interest in exploiting plasmonics for lasing was sparked by the seminal paper by Bergman and Stockman in 2003 [11], where plasmonics was proposed for reaching deeply sub-diffraction sized lasers, ultralow thresholds, ultrafast laser dynamics, and unique properties due to the fact that only a few gain molecules and intracavity photons participate [12]. This vision of a 'spaser' where lasing occurs due to nanoscale amplification of dark plasmons has led to a suite of recent experiments focusing on the smallest plasmonic lasers, targeting colloidal metal particles with gain [13] as well as hybrid plasmon modes confined in a narrow gap between a metal film and II-VI or III-V nanowires that provided the gain [14–19].

Aside from efforts to realize the highest possible field enhancements in narrow gaps of single structures, many efforts in plasmonics have been devoted to light-matter interaction in oligomers of scatterers and periodic lattices. Indeed Yagi-Uda phased array antennas [20–24], Fano resonant oligomers [25–29] and periodic lattices [30–36] are among the most practical structures not only to control field enhancement but also to obtain a balanced trade off between enhancement, Ohmic loss, and directivity control for emitters. In particular, in diffractive lattices single particle plasmon resonances can hybridize with Rayleigh anomalies or with planar waveguide modes to form extended collective modes [37]. These systems have been shown to be very practical for improving broad area emission devices such as LEDs and phosphors, allowing simultaneous control over emission directivity and rate, at much lower losses than offered by single particle resonances [30–33]. The picture that has emerged is that plasmonic structures can on one hand significantly enhance emission brightness from intrinsically very inefficient emitters by use of Purcell enhancement as a means to help radiative decay to outcompete nonradiative processes. On the other hand, in realistic application scenarios for solid-state lighting, already very efficient emitters can not benefit from plasmonics through Purcell enhancement, but do benefit through plasmonic band structure effects that ensure redirection of light into select angles. In this case, the most efficient redirection is obtained through extended, not strongly localized, plasmon modes.

In the context of lasing, diffractive plasmon lattices were first studied by Stehr et al. [38], who reported a metallic particle grating based laser and showed linewidth narrowing and threshold behavior in these systems. A complementary geometry was reported very recently by van Beijnum et al. [39] who demonstrated a plasmon lattice laser based on hole arrays in gold paired to a III-V quantum well gain medium. Suh et al., and Zhou et al. [40, 41], finally, reported on lasing in bow tie and nanodisk arrays, i.e., in particle arrays similar to those reported by Stehr et al. [38] As in the case of spontaneous emission enhancement, plasmonic effects can impact lasing through two

effects. On one hand, Purcell enhancements and near field enhancement can accelerate emission dynamics. On the other hand, even in absence of strong Purcell enhancements the formation of a plasmonic band structure with large stop gaps could modify the distributed feedback mechanism. The work of Suh et al. and Zhou *et al.* [40, 41] focused particularly on the role of plasmonic Purcell enhancements in lasing, for which reason an intrinsically very poor efficiency gain medium was chosen. Thereby, only the dye in very close proximity to the metal that experienced rate enhancement participated in the lasing. Here we focus on the more application relevant scenario of plasmonic lasing in an efficient gain medium, in which case the main questions that arise are how the band structure of plasmonic lattice lasers differs from that of conventional 2D distributed feedback (DFB) lasers due to the plasmonic nature of its constituents, and how the trade off between much larger scattering strength and disadvantageously large loss of metal particles influences the lasing behavior.

In this Chapter we report a comprehensive lasing study on particle array lasers fabricated from square lattices of silver (Ag), gold (Au) and as non-plasmonic reference titanium dioxide (TiO_2) embedded in a dye-doped polymer that at the same time acts as gain medium and supports a waveguide mode. We aim at uncovering what the band structure and lasing conditions of such systems are as a function of scattering strength (highest for Ag particles) and loss (highest for Au particles). Therefore we use a high efficiency dye as would be used in prospective solid-state applications, and operate in a regime where the effects of Purcell enhancements are expected to be small. To answer these questions we have implemented a new measurement technique to map below-threshold emission and lasing in energy-momentum diagrams that can be acquired in a single shot in our sub-nanosecond optically-pumped setup, and that span the entire angular collection range of a high-NA objective. We analyze the plasmonic band structure and for Ag arrays find stop gap widths far in excess of those in dielectric DFB lasers and similar to those in the reported metal hole array laser of van Beijnum [39]. The Chapter is structured as follows. In section 2.2 we explain the setup, materials and measurement procedure. In section 2.3 we present emission spectra, measured 2D Fourier space distributions of emission and energy-momentum diagrams, all below and above threshold. In section 2.4 we interpret our band structure measurements in terms of calculated single particle scattering properties obtained from finite element simulations, and in terms of calculated angle-dependent extinction obtained with a rigorous coupled wave analysis (RCWA) method.

2.2 Experiment

Sample fabrication

We use Menzel glass cover slides of 24 x 24 x 0.17 mm that have been cleaned in a solution of H_2O, H_2O_2 and NH_4OH at 75 °C. After cleaning, we spincoat a positive resist to define our structures. For this we use the electron beam resist ZEP520 diluted in a ratio of 5:2 with anisole for which spincoating at 1500 rpm results in a layer

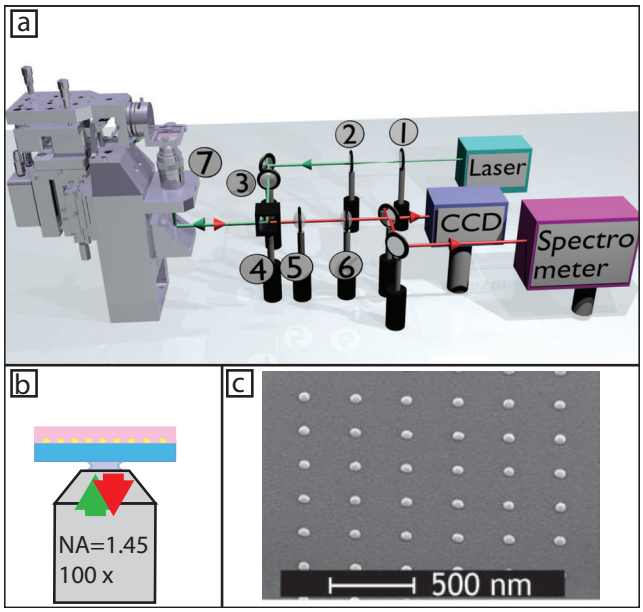

Figure 2.1: (a) Schematic of the setup. We illuminate the sample with laser light (λ=532 nm) from the glass side. We measure the fluorescence using the CCD and spectrometer. Right after the laser there are two lenses (1 and 2) that constitute a telescope to increase the beam diameter. After reflection of a mirror, there is an epi-lens (3) followed by a filter cube (4) that contains the dichroic mirror and a long pass filter, allowing only fluorescent red light on the detector side. On the right side of the filter cube there is a flippable fourier lens (f=200 mm)(5) followed by a tube lens (f=200 mm)(6). The objective is mounted in a specially designed microscope mount (7). Not shown in the image are the AOM, together with a polarizer just in front of the telescope, to tune the laser power. In (b) we show a schematic of the objective with the sample. In (c) a scanning electron micrograph of one of the fabricated particle arrays is shown.

thickness of 150 nm. With electron beam lithography we define hole arrays in a square pattern using dot exposures between 0.001 pC and 0.002 pC using an electron gun voltage of 20 kV and a current of 0.031 nA. We vary the lattice constant from 350 nm to 500 nm in steps of 10 nm. The hole size is 100 nm. The hole arrays are 200 μm in size so that in optical experiments explained below, the arrays exceed the optical pump spot in diameter. To fabricate silver particle arrays we subsequently deposit 2 nm of chromium followed by 30 nm of silver by thermal evaporation, performed at a pressure of $< 10^{-6}$ at an evaporation rate of 0.5-1 Å/s. For the titanium dioxide samples we directly deposit 30 nm of titanium dioxide using electron beam deposition. We perform lift-off by immersing the samples in N-methyl pyrrolidone (NMP) at 65° for 5 minutes. For silver, lift-off is achieved by leaving them overnight at 50° in anisole, as NMP degrades silver. After lift off the samples are rinsed in isopropanol and blow dried with nitrogen. Figure 3.1c shows an Ag particle array resulting from the fabrication procedure.

To obtain a waveguide with gain, we use the negative photoresist SU8 and dope it with rhodamine 6G by mixing 5.25 mg of Rh6G perchlorate with 1 mL of cyclopentanone (the solvent for SU8). The cyclopentanone with Rh6G is added to 1 ml of SU8-2005, after which we ultrasonicate the solution for 10 minutes. The final solution has a Rh6G perchlorate concentration of 0.25 wt%. We spincoat the SU8 solution on the particle array samples at 3000 rpm, resulting in a 450 nm thick SU8 layer. This thickness results from a tradeoff between two requirements: on one hand sufficiently small thickness to ensure single waveguide mode operation, and on the other hand sufficiently large thickness to ensure good mode overlap with the gain medium. After spincoating, we bake the samples for 2 minutes at 95 °C to evaporate the excess cyclopentanone. Prepared as such, the SU8 is not cross-linked, enabling removal of the SU8 layer with acetone after performing measurements on the samples.

Experimental setup

We use an inverted fluorescence microscope as shown in figure 3.1(a). In this setup, the sample is mounted with the glass side down (close up sketch panel (b)), and both pump and detection occur through the objective, i.e. from the glass side. We use a home-built microscope tower, the most important pieces of which are an objective (Nikon, Plan Apo λ 100x /1.45 NA) fixed to the microscope frame and a sample mount that can be translated in XYZ relative to the objective using micromechanical and piezo controls. The sample is pumped using a 532 nm pulsed laser (Teem Photonics, type STG-03E-1S0) which has a pulse width of 500 ps and a maximum energy per pulse of 4.5 μJ. We use an epi-lens in the pump path, resulting in a parallel beam with a diameter of 70 μm emerging from the objective. The laser power is computer controlled by an acousto-optical modulator (AOM). We monitor the resulting pump power in real time with a home built pulse integrator. To filter out unwanted reflected pump light the fluorescence is sent through a long pass filter (Chroma, HHQ545lp) after passing the dichroic mirror (Semrock, Di01-R532-25x36). Fluorescence is detected by either a thermoelectrically cooled (Andor CLARA) Si CCD camera or a Shamrock303i spectrometer with an (Andor Ivac) Si CCD detector. To focus the light on the CCD and spectrometer entrance slit, we use an f=200 mm tube lens. The pump laser can fire single pulses allowing single shot measurements when triggering the laser, CCD and spectrometer simultaneously. Single shot exposure minimizes sample damage caused by bleaching of the Rh6G when performing a sequence of measurements for varying pump power. In addition to collecting images and spectra in real space, we do fourier imaging by adding a lens on a flip mount at a focal distance from the back focal plane of the objective [42–47].

Fourier imaging maps the back focal plane of the objective onto the CCD camera, providing direct information on angular emission. The high NA objective (NA=1.45) allows for a large maximum collection angle of $\theta = 73°$ in glass, enabling us to image a large part of $k_{||}$ space. We note that the 2D back focal plane images we collect in this fashion on the Clara CCD camera are panchromatic images, i.e., not separated in spectral components. Ideally one would measure a spectrally resolved Fourier image,

since a spectrally resolved fourier image would be a direct map of the dispersion diagram. This can be done by scanning a fiber which is coupled to a spectrometer through the entire fourier image, or by imaging a slice of the fourier image centered at k_x=0 onto the slit of an imaging spectrometer [48]. As we aim at single-shot measurements the latter method is preferred. The Andor IVAC camera contains a CCD chip with 200 x 1650 pixels. To make spectral fourier images we set the spectrometer imaging mode to full imaging resulting in a full spectrum for 200 points along the k_y axis.

For every particle array we start by taking fourier images of the fluorescence of single pump pulses as a function of input power by increasing the AOM voltage linearly in 200 steps from 0% to 50% of its maximum value. Subsequently, we flip in the mirror, sending the light to the spectrometer. We center the fourier image on the spectrometer slit by fully opening the slit, observing the image in 0^{th} order and moving the fourier lens transversally until the circular fourier image is in the center of the image of the slit. For fourier spectra, we need to add the fluorescence resulting from 50 pulses because the light is spread over a large detector area. We find that 50 pump pulses do bleach the sample noticeably for higher pump powers. To make sure we see clear signs of lasing before the sample has bleached, we start with high pump powers (above lasing threshold) at an AOM percentage of 50% and go down in 200 steps to 0%. From the fourier spectra we calculate real space spectra by integrating over k_y for each wavelength. Because of bleaching the threshold pump powers deduced from the fourier images are slightly lower than the threshold we find from the fourier spectra.

2.3 Results

Spectra

Figure 2.2(a) shows a waterfall plot of spectra for increasing pump pulse power for a silver particle array with a pitch of 380 nm and particle diameter of 100 nm. These spectra are obtained by applying full vertical binning over the central part of the fourier image, thus including all angles along the k_y axis. At a pump pulse energy of 59 nJ (corresponding to a pulse irradiance of 1.53 mJ/cm^2) a clear peak emerges at a wavelength of 589 nm which dominates the emission spectrum for all higher pump powers. This can be seen more clearly from the inset of figure 2.2 where we plot a spectrum just below (red graph) and just above lasing threshold. The onset of the sharp peak is characteristic of lasing and the pump power at which it occurs is the lasing threshold. From the inset it can be seen that the lasing peak linewidth is on the order of a nanometer which is limited by the resolution of the spectrometer.

To construct a threshold curve, we define emission power as the total number of CCD counts under the lasing peak visible in figure 2.2(a), where we integrate over three spectral bins, corresponding to a total bandwidth of 0.5 nm. Figure 2.2(b) shows the emission power versus pump power. The lasing threshold can be recognized by a sharp kink at a pulse energy just below 60 nJ. The pulse energy density required to

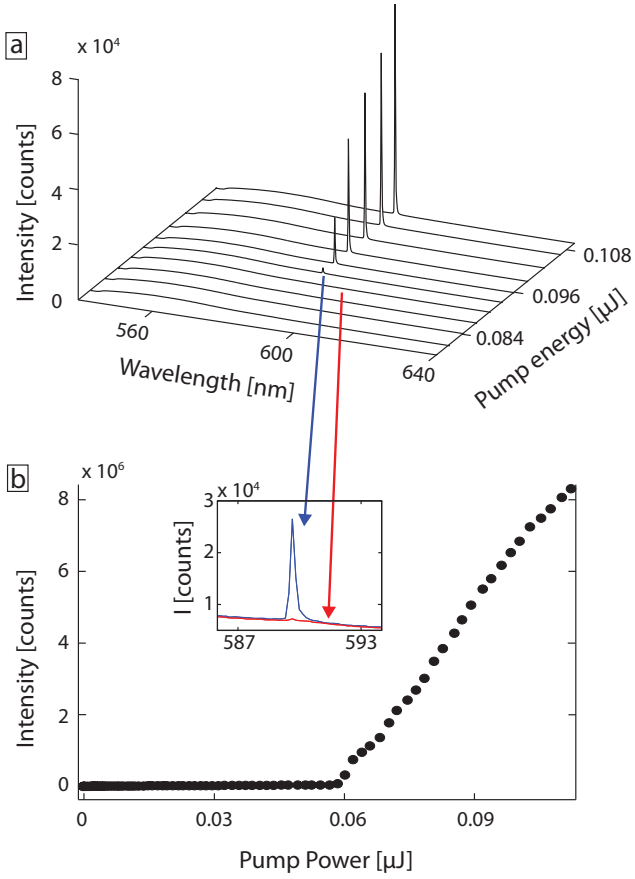

Figure 2.2: (a) Plot of emission spectra for different pump powers measured by imaging an Ag particle array (pitch 380 nm, particle diameter 100 nm) onto the spectrometer slit measured upon excitation with a single pump pulse. A clear threshold behaviour can be seen from the sharp peak occurring for pump powers above 59 nJ. Panel (b) threshold curve, plotting the area under the lasing peak versus pump pulse enery. The inset shows two spectra just above and just below threshold.

reach threshold is thus around 1.53 mJ/cm^2. This pulse energy density is comparable to that reported for plasmon particle arrays in a non-waveguiding polymeric gain layer by Zhou et al. [41], although that laser operated much further into the infrared. These thresholds are approximately 10 times above those typically required for purely polymeric DFB lasers, such as the 2D MEH PPV DFB laser reported by Turnbull [49]. Finally we note that Stehr et al. [38] reported thresholds about equal to those of Turnbull et al.[49] for a gold particle array plasmon laser in a poly paraphenylene matrix. Besides possible differences in gain coefficient, two possible explanations are the presence of ohmic damping in the plasmonic particles and the much stronger outcoupling through scattering that plasmon particles offer.

Fourier images

In addition to measuring spectra as a function of pump power, we collect fourier images of the fluorescence as shown in figure 2.3 and 2.4, which report Fourier images just below and just above threshold respectively, for four particle lattices with pitches d=360, 370, 380 and 390 nm (panels a-d in both figures). In each figure, two features stand out independent of particle pitch. First, we see a high intensity ring where most of the emission exists, indicating that most below-threshold emission exits at large angles.

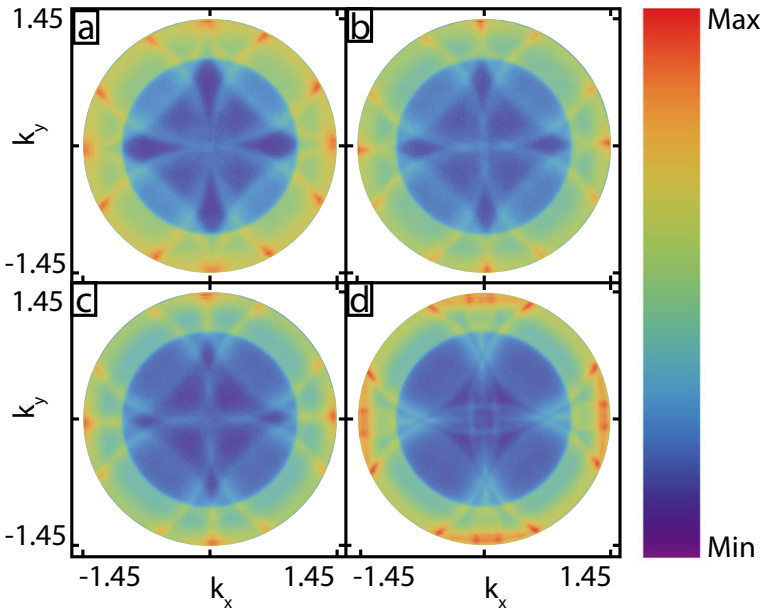

Figure 2.3: Fourier images below the lasing threshold for a pitch of a) 360 nm, b) 370 nm, c) 380 nm and d) 400 nm. The color map ranges are [223, 1196], resp. [102, 739], [128, 941] and [319, 1948]. The reported wave vector axes are normalized to ω/c.

The inner edge of this ring corresponds to an NA of 1 or equivalently, to the critical angle of the glass-air interface. The outer edge is set by the NA of the immersion oil objective. That fluorescence is preferentially emitted at angles just above an NA=1 is a well known feature for emitters on a glass-air interface [43, 48, 50], and consistent with radiation pattern calculations according to chapter 10 of Ref. [50], which show radiation patterns peaking at the critical angle of the glass-air interface.

Second, we see higher intensity circles, displaced from the center and repeating in the k_x and k_y direction with a fixed period that changes with particle pitch. Indeed based on the wave vector scale calibration of our images we can confirm that the Fourier space periodicity corresponds to a square lattice with $\frac{2\pi}{d}$ period, i.e., to the reciprocal lattice of our structure. Based on the absolute wave vector scale calibration of our images, we can also convert the radius of the circles into a propagation constant. We find $k_{\text{circle}}/(\omega/c) = 1.52 \pm 0.03$, where the factor 1.52 corresponds very well with the calculated mode index for the fundamental TE and TM guided mode of the SU8 layer as calculated from Eq. 4.4 and 4.17 in Ref. [51].

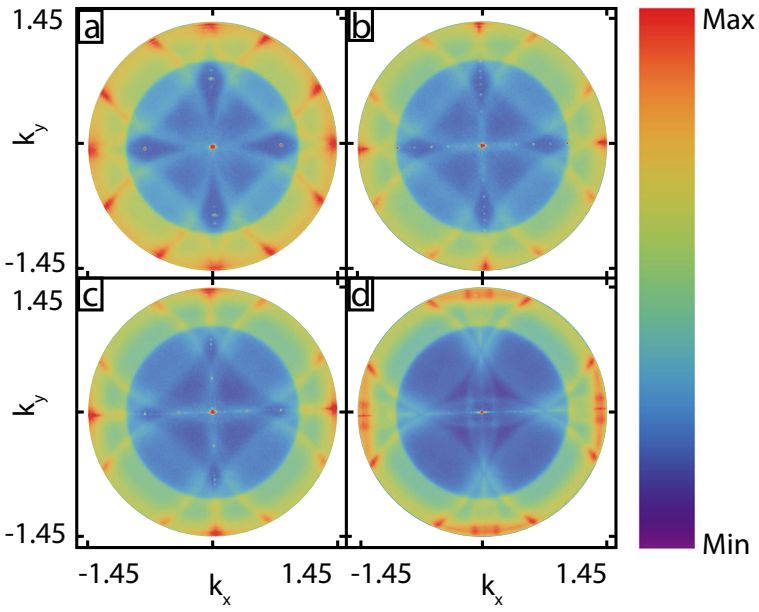

Figure 2.4: Fourier images *just* above the lasing threshold for a pitch of a) 360 nm, b) 370 nm, c) 380 nm and d) 400 nm. The color map ranges are the same as in figure 2.3. Note the appearance of the narrow feature in the center of all images, which shows the onset of lasing emission. The reported wave vector axes are normalized to ω/c.

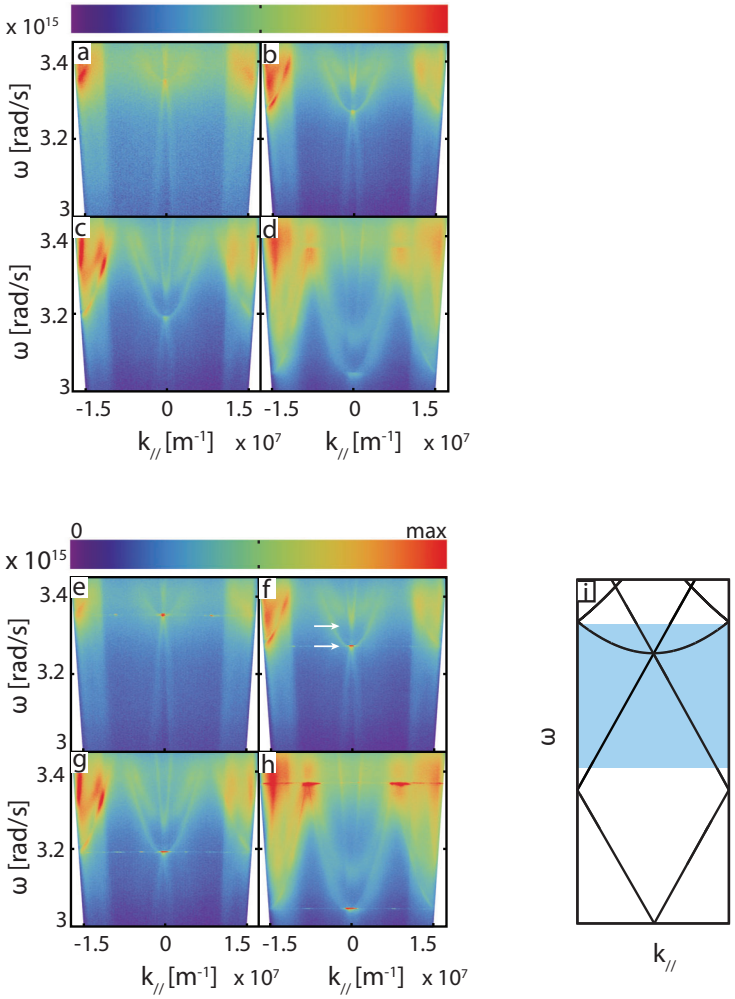

Figure 2.5: Fourier spectra for 4 different pitches, just below threshold (a-d) and just above threshold (e-h), and a schematic of a general banddiagram (i). Measurements are for a pitch of 360 nm (a and e), 370 nm (b and f), 380 nm (c and g) and 400 nm (d and h). The maximum value of the color bar are set at 230, 200, 200 and 250 counts respectively, in (a-d). Above threshold the maximum value of the colorbar is 230, 250, 200 and 300 counts, respectively (panels e-h). All colorbars start at 0. Note the lasing emission that appears as a narrow feature at $k_{||} = 0$ (The horizontal lines across the diagram, surrounding the lasing peak, are CCD blooming artifacts). For clarity we have indicated the lower and upper stop band edge for second order diffraction by white arrows in panel (f). Lasing occurs at the lower edge.

Band diagrams

Overall the fluorescence Fourier pattern is a direct, single-shot CCD image of the repeated zone scheme iso-frequency surface of the waveguide mode dispersion that is well known to occur for periodically corrugated waveguides [52–55]. In other words, due to in-plane Bragg scattering that couples any $\mathbf{k}_{||}$ into $\mathbf{k}_{||} + \mathbf{G}$, the circular dispersion relation ω, $\mathbf{k}_{||}$ of the waveguide mode of index n=1.52 repeats at every reciprocal lattice point $\mathbf{G}$. We expect that for each intersection of circles an anti-crossing should be visible, as the finite scattering strength of the plasmon particles should open up noticeable stop gaps in the nearly free photon dispersion approximation. However, any stop gaps that may occur at the crossing points are obscured in these images due to the fact that spectral averaging limits their sharpness. To overcome this problem we use the spectral imaging procedure described in the experimental section which gives us full dispersion diagrams of the emission over the entire detectable $\mathbf{k}_y$ range. The resulting ω, k_y diagrams are shown in figure 2.5(a-d, just below threshold) and figure 2.5(e-f, just above threshold). Again we can see high intensity bands corresponding to the high intensity ring in the fourier image. In addition, we distinguish a pair of steep straight lines that cross at the Γ point ($k_y = 0$) at a frequency of $3.4 \cdot 10^{15}$ rad·s^{-1} for $d = 360$ nm. Furthermore, a parabolic band with minimum at (or just above) the crossing of steep lines is evident, that has its minimum at or just above the crossing of steep lines. These features can be understood by looking at a generic dispersion diagram respresenting the folded free-photon dispersion, as indicated in figure 2.5i. The straight lines that begin at the origin are the linear waveguide dispersion.

At the first order Bragg condition $k_y = \frac{\pi}{d}$, the free-photon dispersion copies shifted along k_y by $\frac{2\pi}{d}$ fold back into the first Brillouin zone. At twice this frequency the second order diffraction condition is met, as is evident from the fact that the folded dispersions again cross (straight lines). For a square lattice at the same frequency the diffraction condition is met from the grating vector $\mathbf{G} = (\frac{2\pi}{d}, 0)$ perpendicular to the k_y axis. This diffraction leads to the parabola. When the particle pitch increases, the first order Bragg condition is met at a lower frequency and all features move down as the waveguide mode circles repeat with a larger period. In figure 2.5(e-h) we show fourier spectra just above the lasing threshold. Lasing spots are visible as high intensity spots that occur exactly at the crossing point of the lines with the parabola. This corresponds to the second order bragg diffraction condition. Qualitatively this behavior is exactly as generally observed for 2D DFB lasers [38, 41, 49]). In figure 2.5(h) we can see that there is also lasing on the third order bragg condition, as the frequency for the 3rd order condition has moved down into the gain window of Rh6G for a pitch of 400 nm. Polarization dependent measurements reveal that the lasing mode is a TE mode, corresponding to what has been reported in literature for dielectric DFB lasers [56, 57].

Broadly speaking, it appears that the Ag particle array laser is close to a standard DFB laser in that it operates at the lower edge of the second diffraction stopgap at $\mathbf{k}_{||} = 0$ (stop gap edges indicated by white ticks in panel 2.5(f)). We now ask how the plasmonic nature of the Ag particles modify the DFB characteristics compared to a dielectric DFB laser [30, 59]. In order to probe this question we compare three

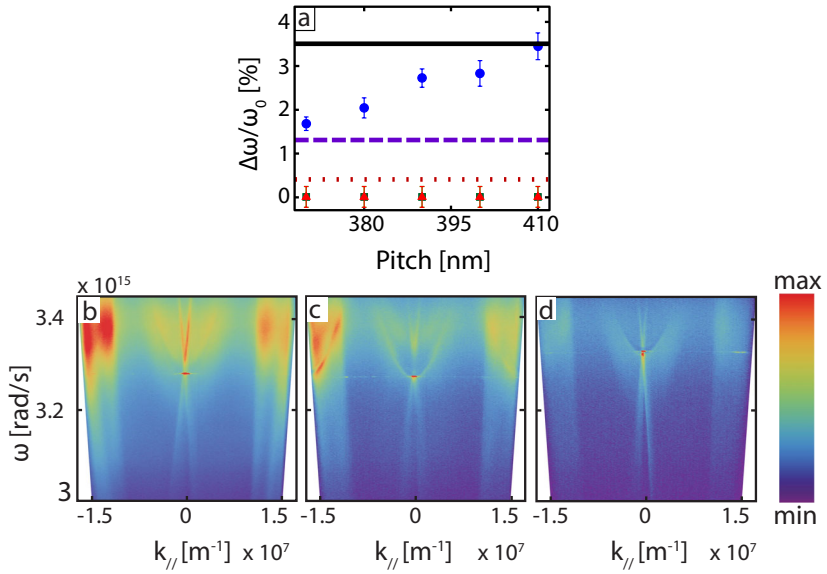

Figure 2.6: In a) the relative size of the stopgap is plotted for Ag (blue dots), Au (red triangles) and TiO_2 (green squares) together with literature values of van Beijnum [39] (black), Turnbull [49] (purple) and Noda [58] (red). In addition, fluorescence in the ω, k_y plane is plotted for Au (b), Ag (c) and TiO_2 (d) for a pitch of 370 nm. The maximum values of the colorbar are 550, resp. 250 and 300 counts in panels (b-e), with colorbars starting at 0. The plots are made just above the lasing threshold, meaning pump powers differ from panel to panel. The pump powers are 944 nJ (Au), 99.5 nJ (Ag), and 38 nJ (TiO_2), respectively. The noteably larger pump power for Au results in a much higher background fluorescence level as is visible for a frequency range centered at the the Rh6G emission peak in figure b.

systems, namely (1) the Ag particle arrays, (2) arrays of the same pitch of dielectric TiO_2 particles, and (3) Au particles that should show stronger absorption yet weaker scattering than the Ag particles. In figure 2.6 we compare the dispersion diagram for a DFB laser with silver scatterers with a DFB laser that uses TiO_2 and Au particles, for a particle pitch of 380 nm and a particle size of 150 nm and 100 nm, respectively. For TiO_2 we used larger particles of 150 nm diameter, as the TiO_2 particle arrays with particle sizes of 100 nm did not show lasing. This we assign to the weak scattering strength of 100 nm TiO_2 disks. Indeed, numerical analysis reported below of scattering cross sections show that TiO2 scatterers of the same volume have a scattering strength at least 10 times lower than metal particles. Two clear differences are visible between figure 2.6(c) and figure 2.6(d). For the TiO_2 sample, the parabolic band appears to be a single feature, as expected from figure 2.5(c). However, strictly speaking the parabolic band is degenerate, originating from both the (1,0) and (-1,0) diffraction order. Remarkably, for the Ag particle array this degeneracy is distinctly split, pointing at the strong scattering strength of Ag particles. Figure 2.6(b) shows the measured

dispersion diagram for an Au array. Evidently, the bands are broad, at least as much as in the Ag case, but not clearly split, as in the TiO_2 case. This points at the higher loss, yet weak scattering strength at 590 nm, of Au particles compared to Ag.

For dielectric photonic crystals, relative stop gap width $\Delta\omega/\omega_0$ is frequently used as a dimensionless parameter to sort photonic crystals by their photonic interaction strength [60–62]. In that case the relative stop gap width is proportional to the ratio of scatterer polarizability to unit cell volume. In real space terms, the stop gap width provides a direct measure for the Bragg length (number of lattice planes required for 1/e diffraction efficiency), the crystal size needed to develop a significant LDOS suppression, and the crystal size required to achieve LDOS enhancement of mode density at a band edge of any significant magnitude and over significant bandwidth [60–62]. On this basis, we use the width of the stopgap to quantify differences in the dispersion diagram for different plasmonic laser systems. Figure 2.6(a) shows a plot of the relative size of this stopgap as a function of particle pitch for Ag, Au and TiO_2. The horizontal lines indicate relative stopgap values reported by van Beijnum [39] (black), Turnbull [49] (purple) and Noda [58] (red)for a plasmonic hole array laser, a non-plasmonic DFB laser, and a photonic crystal band edge laser in a 2D semiconductor membrane. The blue dots for Ag show that the relative bandgaps are large compared to reported values for dielectric systems and approach the value reported for the plasmonic laser of van Beijnum [39]. The red triangles and green squares represent relative bandgaps for TiO_2 and Au. For these two materials the stopgaps are smaller than the width of the band and therefore are essentially zero. To conclude, the Ag particle array DFB lasers are markedly different from the nonplasmonic lasing systems, and due to the strong scattering the diffractive coupling in the dispersion relation is as strong as in the plasmonic hole array laser. Ideally to verify if the correlation between stop gap width and sample geometry is exclusively with scattering strength (or 'polarizability', as in the photonic crystal case) one would need to independently vary physical particle volume at fixed optical volume (polarizability), or vice versa, in an otherwise fixed gain medium. Unfortunately, this will be difficult to realize: while our data clearly show that the nonplasmonic TiO_2 particles of equal physical volume are so weakly scattering as to give neither stop gap nor lasing, a larger optical volume at fixed physical size than for the silver particles can not be realized in the gain window of our dye. Somewhat larger optical volume could be reached with either Ag or Au particles by increasing their size, however only at strongly redshifted resonance frequencies.

Finally we note that in order to cross the lasing threshold, the Au samples typically require at least ten times higher pump fluence (0.066 mJ/cm^2 versus 1.107 mJ/cm^2 for the example in figure 2.6). This finding is consistent with the much more advantageous Ohmic loss of Ag versus Au, which for Au nanodisks means a much lower scattering strength and a much lower albedo. Regarding the comparison between thresholds of the TiO_2 sample with the thresholds of Ag and Au samples, we have to note that a direct comparison is hampered by the fact that the much lower scattering strength of TiO_2 disks means that much larger particles were required than for the plasmonic samples to reach the lasing transition at all. Generally, most all-dielectric samples that actually lased (particle diameters above 150 nm) had lower thresholds than their plasmonic

counterparts. This finding indicates that TiO_2 offers low loss, yet also a much weaker per-particle cross section contributing to feedback.

2.4 Theory

Single particle scattering

We use COMSOL to determine the extinction cross sections for single particles. In figure 2.7 we plot the extinction cross section for Ag, Au and TiO_2 for two different incidence conditions. In figure 2.7(a) an x-polarized plane wave is incident along the z-direction (parallel to the symmetry axis of the particle disk). In figure 2.7(b) an x-polarized plane wave is incident along the y-axis. We used an index of $n = 1.65$ for SU8 as the surrounding medium. For the permitivity we use a modified Drude model fitted to the optical constants of Johnson and Christy [63]:

$$\epsilon_r = \epsilon_\infty - \frac{\omega_p^2}{\omega \cdot (\omega + i\gamma)} \tag{2.1}$$

For Au we use $\epsilon_\infty = 9.54$, $\omega_p = 1.35 \cdot 10^{15}$ rad/s, and $\gamma = 1.25 \cdot 10^{14}$ rad/s and for Ag we use $\epsilon_\infty = 5.43 + 0.55i$, $\omega_p = 1.39 \cdot 10^{16}$ rad/s, and $\gamma = 8.21 \cdot 10^{13}$ rad/s, as reported in Ref. [64].

Both Ag and Au exhibit a clear resonance which is completely absent for TiO_2. In addition, one can see that the peak of Ag is blue shifted with respect to the resonance peak of Au. The lasing frequencies for the studied 4 particle pitches are indicated by the squares. For a plane wave along the y-direction we can distinguish 2 peaks, where the smallest peak (at higher frequencies) corresponds to the quadrupolar resonance.

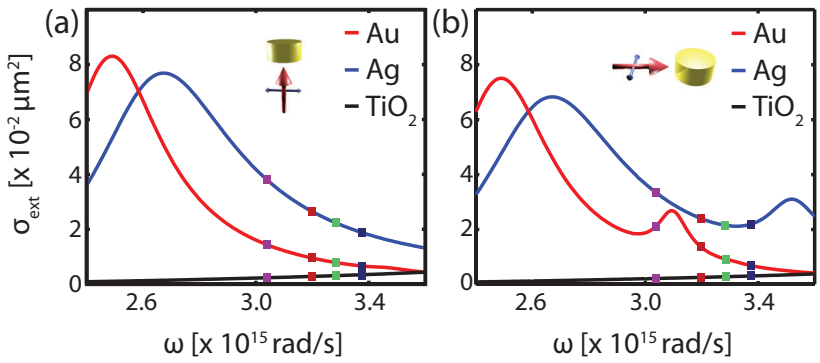

Figure 2.7: Extinction cross sections for Ag, Au and TiO_2 as a function of ω obtained using COMSOL. The z-axis is defined as the axis parallel to the symmetry axis of the particle disks. In plot a) the plane wave is incident along the z-axis and in plot b) the plane wave is incident from the side of the particle, with polarization in the plane of the particle. For clarity the curves for TiO_2 are scaled by a factor 10 as indicated.

For incidence normal to the disks, as would be the case in transmission experiments that probe the sample under normal incidence, no quadrupole response is noticeable. However, for the distributed feedback in-plane scattering of the TE-polarized waveguide mode is important. This distributed feedback hence might benefit from the quadrupole response for enhanced scattering and near fields.

Band structure

Finally we have calculated the band structures of the plasmon gratings embedded in the waveguide structures as they would appear in extinction, using rigorous coupled wave analysis (RCWA) that is optimized for 2D periodic and stratified problems. In particular, we have used the freely available implementation "S^4" by Liu and Fan [65] of the Fourier Modal Method developed by Li [66, 67], that uses the appropriate factorization rules for high index contrast gratings. While convergence can be notoriously poor for metallic gratings, we found excellent convergence when using parallelogrammic truncation. We used a truncation to 361 plane waves. We set $n_{SU8} = 1.65$ and take the particle sizes and dielectric constants as in COMSOL. The index of the glass substrate is set to n=1.51, while we take as waveguide thickness 450 nm. Again, we use the Drude model to describe the permittivity of Ag and Au. We obtain extinction as a function of incidence angle, resulting in the extinction dispersion diagrams shown in figure 2.8. While the Fourier modal method is a fully vectorial method that takes coupling between Bloch harmonics of all polarizations into account, here we report specifically on extinction in the case of s-polarized incidence, corresponding to coupling to TE-waveguide modes. This choice is motivated by our observation of the polarization of the lasing mode, and is commensurate with 2D DFB lasing in dielectric structures [56, 57]. Both the Ag and Au lattice show a band of high extinction at $k_{||} = 0$ close to $\omega = 2.5{\cdot}10^{15}$ rad/s, where as expected the gold array is redshifted compared to the Ag array. This extinction band corresponds to the single particle dipole resonance. Compared to figure 2.7, figure 2.8 shows single particle resonances slightly red shifted as in S^4 simulations infinite particle arrays are considered. When the interparticle distance is comparable to the wavelength, longitudinal coupling between the individual dipole scatterers is known to cause the observed red shift [68]. The higher extinction due to the single particle resonance couples to the waveguide mode [59], leading to anticrossings at $k_{||}$ along the straight lines corresponding to the backfolded waveguide mode dispersion. This anticrossing was observed experimentally by Rodriguez et al. [32]. At $3.2 \cdot 10^{15}$ rad/s and above there are the expected parabola and straight lines from the folded free-photon dispersion discussed in the experimental results. In this part, we can see two clear differences between Au and Ag. First, the parabola for silver is broader than that of gold. Second, at the crossing point of the parabola with the straight lines a clear avoided crossing can be seen for silver, whereas for gold the Γ point does not show a gap and corresponds with the folded free-photon dispersion. The complex avoided crossing that lifts the degeneracy between the two parabolas for silver can be seen more closely in the inset in figure 2.8(b). While the single particle resonance is broad (Q=4.4), the hybrid modes resulting from coupling of waveguide mode and plasmon

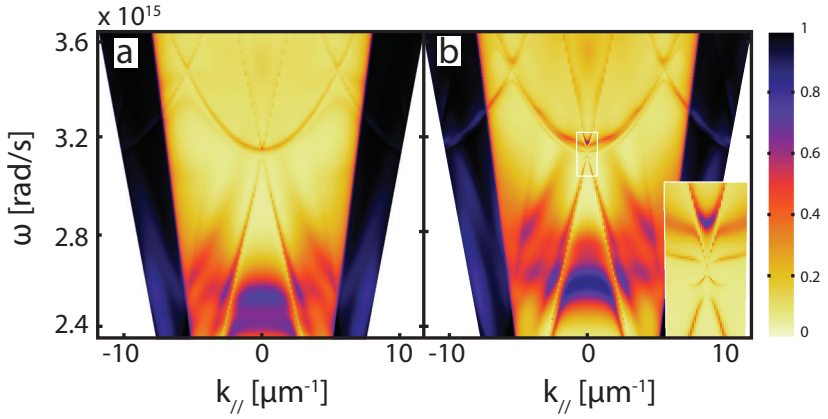

Figure 2.8: Extinction as a function of $k_{||}$ and ω for gold (a) and silver (b) calculated with S^4. Evident for both diagrams are 1) the high extinction region for lower ω, corresponding to the single particle resonance, and 2) the generic folded band diagram features (lines and parabola's). For silver a clear stop gap is visible at the Γ point ($\mathbf{k}_{||} = 0$) that is not apparent in the diagram for gold. The inset shows a zoom in of this region, highlighting the intricate anticrossing with the two parabolic bands.

have Q> 150, i.e., damping much less than the single particle radiative damping.

Returning to a comparison with the measurements we conclude that the theory reproduces all the salient features. For the gold particle lattices, the scattering strength per particle is low. Consequently in both theory and data, the stop gap width is small. For the silver particle lattice, however, the scattering strength per particle is much higher and consequently in both theory and experiment a clear stop gap opens up at the second order diffraction, and the degenerate parabolas split, and broaden. Based on the single particle response we surmise that the precise coupling strength that splits the bands at $3.2 \cdot 10^{15}$ rad/s and above is dependent on the quadrupole response. Finally we note that we also calculated dispersion for TiO_2 particle lattices. As in experiment, the calculated dispersion (not shown) only shows narrow features that essentially coincide with the folded SU8 waveguide dispersion.

2.5 Conclusion and outlook

Overall, it is remarkable that despite their loss, silver particle array lasers provide lasing characteristics reasonably competitive with dielectric DFB systems, commensurate with the established notion that the extended diffractive modes that plasmon arrays support well off their individual resonance frequencies are promising for balancing loss and light matter interaction strength. Furthermore, our results and experimental methods open up many questions for further study. To start, it would be very interesting to sweep the diffraction condition and gain window onto the plasmon resonance frequency. This

allows to continuously trace how lasing occurs along the transition from a weakly coupled plasmon-waveguide hybrid system to a purely plasmonic mode. Second, if one could probe lasing in a given system for gain media of different quantum efficiencies, one could further clarify the role of high Purcell factors near metal particles in lasing plasmonic lattices. In our work, we estimate that less than 1% of emitters is within 20 nm of metal, i.e., is in a position where Purcell enhancement might occur. Since we use an intrinsically already highly efficient, bright, emitter, there is no measurable Purcell enhancement, and in fact those dyes that experience rate enhancement likely are rendered *less* efficient contributors to the lasing process due to quenching. This should be contrasted to the work of Suh et al. and Zhou et al. [40, 41]. Third, by significantly reducing the pitch, one enters the 'lasing spaser' regime proposed by Zheludev et al. Zheludev et al.[69] proposed that when plasmon resonators with gain are arrayed with pitch much smaller than the wavelength, lasing will not occur on a diffraction condition, yet coherence will be established to give lasing emission normal to the lattice plane. Generally we expect that if a dense metasurface would lase, it would do so on the lowest loss mode in the wave vector diagram. Hence this regime directly necessitates a deep study of the dispersion relation of collective modes in metamaterials. Finally, an obvious extension of our work is to study aperiodic systems [70–72]. Previous studies have shown that aperiodic and quasiperiodic systems, as an intermediate state between order and disorder, have modes that are neither Bloch states as in a periodic lattice, nor exponentially localized states as in a random array, but exhibit 'critical modes' that show strong spatial fluctuations in field amplitude [70, 73]. It would be interesting to study these critical modes in the context of lasing.

References

[1] S. A. Maier, *Plasmonics: Fundamentals and Applications*, Springer, 2007.

[2] M. Agio and A. Alù, *Optical Antennas*, Cambridge University Press, 2013.

[3] P. Anger, P. Bharadwaj, and L. Novotny, *Enhancement and quenching of single-molecule fluorescence*, Phys. Rev. Lett. **96**, 113002 (2006).

[4] S. Kühn, U. Håkanson, L. Rogobete, and V. Sandoghdar, *Enhancement of single-molecule fluorescence using a gold nanoparticle as an optical nanoantenna*, Phys. Rev. Lett **97**, 017402 (2006).

[5] H. Mertens, A. F. Koenderink, and A. Polman, *Plasmon-enhanced luminescence near noble-metal nanospheres: Comparison of exact theory and an improved Gersten and Nitzan model*, Phys. Rev. B **76**, 115123 (2007).

[6] V. Giannini, A. I. Fernandez-Dominguez, S. C. Heck, and S. A. Maier, *Plasmonic nanoantennas: Fundamentals and their use in controlling the radiative properties of nanoemitters*, Chem. Rev. **111**, 3888 (2011).

[7] D. Punj, M. Mivelle, S. B. Moparthi, T. S. van Zanten, H. Rigneault, N. F. van Hulst, M. F. García-Parajo, and J. Wenger, *A plasmonic 'antenna-in-box' platform for enhanced single-molecule analysis at micromolar concentrations*, Nat. Nanotechnol. **8**, 512 (2013).

[8] A. Kinkhabwala, Z. Yu, S. Fan, Y. Avlasevich, K. Muellen, and W. E. Moerner, *Large single-molecule fluorescence enhancements produced by a bowtie nanoantenna*, Nat. Photonics **3**, 654 (2009).

[9] P. L. Stiles, J. A. Dieringer, N. C. Shah, and R. R. Van Duyne, *Surface-enhanced Raman spectroscopy*, Annu. Rev. Anal. Chem. **1**, 601 (2008).

[10] F. Le, D. W. Brandl, Y. A. Urzhumov, H. Wang, J. Kundu, N. J. Halas, J. Aizpurua, and P. Nordlander, *Metallic nanoparticle arrays: A common substrate for both -enhanced Raman scattering and -enhanced infrared absorption*, ACS Nano **2**, 707 (2008).

[11] D. J. Bergman and M. I. Stockman, *Surface plasmon amplification by stimulated emission of radiation: Quantum generation of coherent plasmons in nanosystems*, Phys. Rev. Lett **90**, 027402 (2003).

[12] M. I. Stockman, *The spaser as a nanoscale quantum generator and ultrafast amplifier*, J. Opt. **12**, 024004 (2010).

[13] M. A. Noginov, G. Zhu, A. M. Belgrave, R. Bakker, V. M. Shalaev, E. E. Narimanov, S. Stout, E. Herz, T. Suteewong, and U. Wiesner, *Demonstration of a spaser-based nanolaser*, Nature **460**, 1110 (2009).

[14] R. F. Oulton, V. J. Sorger, T. Zentgraf, R.-M. Ma, C. Gladden, L. Dai, G. Bartal, and X. Zhang, *Plasmon lasers at deep subwavelength scale*, Nature **461**, 629 (2009).

[15] R.-M. Ma, R. F. Oulton, V. J. Sorger, G. Bartal, and X. Zhang, *Room-temperature sub-diffraction-limited plasmon laser by total internal reflection*, Nat. Mater. **10**, 110 (2011).

[16] S.-H. Kwon, J.-H. Kang, C. Seassal, S.-K. Kim, P. Regreny, Y.-H. Lee, C. M. Lieber, and H.-G. Park, *Subwavelength plasmonic lasing from a semiconductor nanodisk with silver nanopan cavity*, Nano Lett. **10**, 3679 (2010).

[17] Y.-J. Lu, J. Kim, H.-Y. Chen, C. Wu, N. Dabidian, C. E. Sanders, C.-Y. Wang, M.-Y. Lu, B.-H. Li, X. Qiu, W.-H. Chang, L.-J. Chen, G. Shvets, C.-K. Shih, and S. Gwo, *Plasmonic nanolaser using epitaxially grown silver film*, Science **337**, 450 (2012).

[18] M. T. Hill, Y.-S. Oei, B. Smalbrugge, Y. Zhu, T. De Vries, P. J. Van Veldhoven, F. W. M. Van Otten, T. J. Eijkemans, J. P. Turkiewicz, H. De Waardt, E. J. Geluk, S.-H. Kwon, Y.-H. Lee, R. Notzel, and M. K. Smit, *Lasing in metallic-coated nanocavities*, Nat. Photonics **1**, 589 (2007).

[19] M. Khajavikhan, A. Simic, M. Katz, J. H. Lee, B. Slutsky, A. Mizrahi, V. Lomakin, and Y. Fainman, *Thresholdless nanoscale coaxial lasers*, Nature **482**, 204 (2012).

[20] J. Li, A. Salandrino, and N. Engheta, *Shaping light beams in the nanometer scale: A Yagi-Uda nanoantenna in the optical domain*, Phys. Rev. B **76**, 245403 (2007).

[21] A. F. Koenderink, *Plasmon nanoparticle array waveguides for single photon and single plasmon sources*, Nano Lett. **9**, 4228 (2009).

[22] T. Kosako, Y. Kadoya, and H. F. Hofmann, *Directional control of light by a nano-optical Yagi-Uda antenna*, Nat. Photonics **4**, 312 (2010).

[23] A. G. Curto, G. Volpe, T. H. Taminiau, M. P. Kreuzer, R. Quidant, and N. F. van Hulst, *Unidirectional emission of a quantum dot coupled to a nanoantenna*, Science **329**, 930 (2010).

[24] F. B. Arango, A. Kwadrin, and A. F. Koenderink, *Plasmonic antennas hybridized with dielectric waveguides*, ACS Nano **6**, 10156 (2012).

[25] S. Zhang, D. A. Genov, Y. Wang, M. Liu, and X. Zhang, *Plasmon-induced transparency in metamaterials*, Phys. Rev. Lett. **101**, 047401 (2008).

[26] B. Luk'yanchuk, N. I. Zheludev, S. A. Maier, N. J. Halas, P. Nordlander, H. Giessen, and C. T. Chong, *The Fano resonance in plasmonic nanostructures and metamaterials*, Nat. Mater. **9**, 707 (2010).

[27] N. Verellen, Y. Sonnefraud, H. Sobhani, F. Hao, V. V. Moshchalkov, P. Van Dorpe, P. Nordlander, and S. A. Maier, *Fano resonances in individual coherent plasmonic nanocavities*, Nano Lett. **9**, 1663 (2009).

[28] M. Hentschel, M. Saliba, R. Vogelgesang, H. Giessen, A. P. Alivisatos, and N. Liu, *Transition from isolated to collective modes in plasmonic oligomers*, Nano Lett. **10**, 2721 (2010).

[29] J. B. Lassiter, H. Sobhani, J. A. Fan, J. Kundu, F. Capasso, P. Nordlander, and N. J. Halas, *Fano resonances in plasmonic nanoclusters: Geometrical and chemical tunability*, Nano Lett. **10**, 3184 (2010).

[30] G. Lozano, D. J. Louwers, S. R. K. Rodriguez, S. Murai, O. T. A. Jansen, M. A. Verschuuren, and J. Gómez Rivas, *Plasmonics for solid-state lighting: enhanced excitation and directional emission of highly efficient light sources*, Light. Sci. Appl. **2**, e66 (2013).

[31] S. Murai, M. A. Verschuuren, G. Lozano, G. Pirruccio, S. R. K. Rodriguez, and J. Gómez Rivas, *Hybrid plasmonic-photonic modes in diffractive arrays of nanoparticles coupled to light-emitting optical waveguides*, Opt. Express **21**, 4250 (2013).

[32] S. R. K. Rodriguez, S. Murai, M. A. Verschuuren, and J. Gómez Rivas, *Light-emitting waveguide-plasmon polaritons*, Phys. Rev. Lett. **109**, 166803 (2012).

[33] G. Vecchi, V. Giannini, and J. Gómez Rivas, *Shaping the fluorescent emission by lattice*

resonances in plasmonic crystals of nanoantennas, Phys. Rev. Lett. **102**, 146807 (2009).

[34] C. L. Haynes, A. D. McFarland, L. L. Zhao, R. P. Van Duyne, G. C. Schatz, L. Gunnarsson, J. Prikulis, B. Kasemo, and M. Käll, *Nanoparticle optics: The importance of radiative dipole coupling in two-dimensional nanoparticle arrays*, J. Phys. Chem. B **107**, 7337 (2003).

[35] A. A. Penzkofer and Y. Lu, *Fluorescence quenching of rhodamine 6g in methanol at high concentration*, Chem. Phys. **103**, 399 (1986).

[36] F. J. García de Abajo, *Colloquium: Light scattering by particle and hole arrays*, Rev. Mod. Phys. **79**, 1267 (2007).

[37] R. de Waele, A. F. Koenderink, and A. Polman, *Tunable nanoscale localization of energy on plasmon particle arrays*, Nano Lett. **7**, 2004 (2007).

[38] J. Stehr, J. Crewett, F. Schindler, R. Sperling, G. von Plessen, U. Lemmer, J. M. Lupton, T. A. Klar, J. Feldmann, A. W. Holleitner, M. Forster, and U. Scherf, *A low threshold polymer laser based on metallic nanoparticle gratings*, Adv. Mater. **15**, 1726 (2003).

[39] F. van Beijnum, P. J. van Veldhoven, E. J. Geluk, M. J. A. de Dood, G. W. 't Hooft, and M. P. van Exter, *Surface plasmon lasing observed in metal hole arrays*, Phys. Rev. Lett. **110**, 206802 (2013).

[40] J. Y. Suh, C. H. Kim, W. Zhou, M. D. Huntington, D. T. Co, M. R. Wasielewski, and T. W. Odom, *Plasmonic bowtie nanolaser arrays*, Nano Lett. **12**, 5769 (2012).

[41] W. Zhou, M. Dridi, J. Y. Suh, C. H. Kim, D. T. Co, M. R. Wasielewski, G. C. Schatz, and T. W. Odom, *Lasing action in strongly coupled plasmonic nanocavity arrays*, Nat. Nanotechnol. **8**, 506 (2013).

[42] I. Sersic, C. Tuambilangana, and A. F. Koenderink, *Fourier microscopy of single plasmonic scatterers*, New J. Phys. **13**, 083019 (2011).

[43] M. A. Lieb, J. M. Zavislan, and L. Novotny, *Single-molecule orientations determined by direct emission pattern imaging*, J. Opt. Soc. Am. B **21**, 1210 (2004).

[44] N. Le Thomas, R. Houdré, M. V. Kotlyar, D. O'Brien, and T. F. Krauss, *Exploring light propagating in photonic crystals with Fourier optics*, J. Opt. Soc. Am. B **24**, 2964 (2007).

[45] S. Randhawa, M. Ujue Gonzalez, J. Renger, S. Enoch, and R. Quidant, *Design and properties of dielectric surface plasmon Bragg mirrors*, Opt. Express **18**, 14496 (2010).

[46] Y. Alaverdyan, E.-M. Hempe, A. N. Vamivakas, H. E, S. A. Maier, and M. Atatüre, *Spectral and angular distribution of Rayleigh scattering from plasmon-coupled nanohole chains*, Appl. Phys. Lett. **94**, 021112 (2009).

[47] C. Huang, A. Bouhelier, G. C. des Francs, A. Bruyant, A. Guenot, E. Finot, J. C. Weeber, and A. Dereux, *Gain, detuning, and radiation patterns of nanoparticle optical antennas*, Phys. Rev. B **78**, 155407 (2008).

[48] T. H. Taminiau, S. Karaveli, N. F. van Hulst, and R. Zia, *Quantifying the magnetic nature of light emission*, Nat. Commun. **3**, 979 (2012).

[49] G. A. Turnbull, P. Andrew, W. L. Barnes, and I. D. W. Samuel, *Photonic mode dispersion of a two-dimensional distributed feedback polymer laser*, Phys. Rev. B **67**, 165107 (2003).

[50] L. Novotny and B. Hecht, *Principles of Nano-Optics*, Cambridge University Press, 2007.

[51] H. P. Urbach and G. L. J. A. Rikken, *Spontaneous emission from a dielectric slab*, Phys. Rev. A **57**, 3913 (1998).

[52] H. Rigneault, F. Lemarchand, A. Sentenac, and H. Giovannini, *Extraction of light from sources located inside waveguide grating structures*, Opt. Lett. **24**, 148 (1999).

[53] W. A. Harrison, *Solid State Theory*, Dover Publications, 1970.

[54] M. Kretschmann and A. A. Maradudin, *Band structures of two-dimensional surface-plasmon polaritonic crystals*, Phys. Rev. B **66**, 245408 (2002).

[55] L. Langguth, D. Punj, J. Wenger, and A. F. Koenderink, *Plasmonic band structure controls single-molecule fluorescence*, ACS Nano **7**, 8840 (2013).

[56] G. A. Turnbull, P. Andrew, M. Jory, W. Barnes, and I. D. W. Samuel, *Relationship between photonic band structure and emission characteristics of a polymer distributed feedback laser*, Phys. Rev. B **64**, 125122 (2001).

[57] G. Heliotis, R. D. Xia, G. A. Turnbull, P. Andrew, W. L. Barnes, I. D. W. Samuel, and D. D. C. Bradley, *Emission characteristics and performance comparison of polyfluorene lasers with one- and two-dimensional distributed feedback*, Adv. Funct. Mater. **14**, 91 (2004).

[58] S. Noda, *Photonic crystal lasers-ultimate nanolasers and broad-area coherent lasers*, J. Opt. Soc. Am. B **27**, B1 (2010).

[59] S. Murai, Y. Tokuda, K. Fujita, and K. Tanaka, *Tuning the wavelength of amplified spontaneous emission coupled to localized plasmon*, Appl. Phys. Lett. **101**, 031117 (2012).

[60] W. L. Vos, R. Sprik, A. van Blaaderen, A. Imhof, A. Lagendijk, and G. H. Wegdam, *Strong effects of photonic band structures on the diffraction of colloidal crystals*, Phys. Rev. B **53**, 16231 (1996).

[61] C. M. Soukoulis, *Photonic Crystals and Light Localization in the 21st Century (p. 194)*, Kluwer, Dordrecht, 2001.

[62] H. Benisty and C. Weisbuch, *Progress in Optics*, chapter Photonic Crystals, pages 177–313, Elsevier, 2006.

[63] P. B. Johnson and P. W. Christy, *Optical constants of the noble metals*, Phys. Rev. B **6**, 4370 (1972).

[64] J. J. Penninkhof, L. A. Sweatlock, A. Moroz, H. A. Atwater, A. van Blaaderen, and A. Polman, *Optical cavity modes in gold shell colloids*, J. Appl. Phys. **103**, 123105 (2008).

[65] V. Liu and S. Fan, *S^4 : A free electromagnetic solver for layered periodic structures*, Comput. Phys. Commun. **183**, 2233 (2012).

[66] L. F. Li, *New formulation of the Fourier modal method for crossed surface-relief gratings*, J. Opt. Soc. Am. A **14**, 2758 (1997).

[67] L. F. Li, *Use of Fourier series in the analysis of discontinuous periodic structures*, J. Opt. Soc. Am. A **13**, 1870 (1996).

[68] I. Sersic, M. Frimmer, E. Verhagen, and A. F. Koenderink, *Electric and magnetic dipole coupling in near-infrared split-ring metamaterial arrays*, Phys. Rev. Lett. **103**, 213902 (2009).

[69] N. I. Zheludev, S. L. Prosvirnin, N. Papasimakis, and V. A. Fedotov, *Lasing spaser*, Nat. Photonics **2**, 351 (2008).

[70] Z. V. Vardeny, A. Nahata, and A. Agrawal, *Optics of photonic quasicrystals*, Nat. Photonics **7**, 177 (2013).

[71] A. Gopinath, S. V. Boriskina, N.-N. Feng, B. M. Reinhard, and L. Dal Negro, *Photonic-plasmonic scattering resonances in deterministic aperiodic structures*, Nano Lett. **8**, 2423 (2008).

[72] S. M. Lubin, A. J. Hryn, M. D. Huntington, C. J. Engel, and T. W. Odom, *Quasiperiodic Moire plasmonic crystals*, ACS Nano **7**, 11035 (2013).

[73] E. Maciá, *Exploiting aperiodic designs in nanophotonic devices*, Rep. Prog. Phys. **75**, 036502 (2012).

3

Band structure in plasmonic lattice lasers

We study lasing in distributed feedback lasers made from square lattices of silver particles in a dye-doped waveguide. We present a systematic experimental study of the band structure underlying the lasing process as a function of the detuning between the particle plasmon resonance and the lattice Bragg diffraction condition. To this end, we use as gain medium either polymer doped with Rh6G only, or polymer doped with a pair of dyes (Rh6G and Rh700) that act as Förster energy transfer (FRET)-pair. This allows for gain at either 590 nm, or near 700 nm when pumped at 532 nm, compatible with the achievable size-tunability of silver particles embedded in the polymer. By polarization-resolved spectroscopic Fourier microscopy we measure the plasmonic/photonic band structure, unravelling both the stop gap width, as well as the loss properties of the 4 involved bands, at fixed lattice Bragg diffraction condition and as function of detuning to the plasmon resonance.

3.1 Introduction

Organic distributed feedback lasers have been widely studied since the mid-nineties for their ability to provide broad area lasing upon optical or electrical pumping, while being cheap to fabricate [1]. Such lasers generally consist of an organic gain medium that is deposited as a thin layer on a dielectric periodically corrugated surface, with a periodicity chosen such that if offers an in-plane Bragg diffraction condition within the

gain window [2, 3]. A wide range of emission wavelengths can be chosen through the availability of a vast range of organic fluorophores and fluorescent polymers, while the relevant, usually weak, perturbative, corrugations can be realized, e.g., through optical lithography, or soft imprint lithography [4, 5].

More recently a different class of lasers was proposed in the domain of plasmonics. Plasmonics revolves around the fact that free electrons in metals offer a collective resonance at optical frequencies [6]. This causes metal nanoparticles or nanostructured surfaces to provide highly enhanced and strongly localized electromagnetic fields upon irradiation, and to provide large spontaneous emission rate enhancements when coupled to nearby fluorescent sources [7–9]. When such plasmonic particles are placed in two-dimensional diffractive periodic arrays, they further provide control over emission directivity and brightness due to a hybridization of localized plasmonic resonances, and grating anomalies associated with the array [10–12]. In particular, these systems have been studied as substrates for Surface Enhanced Raman Scattering (SERS) [13], for sensing [14, 15] and for solid-state lighting [16]. Recently, several groups [17, 18] have shown distributed feedback lasing in such plasmonic periodic systems. A main difference with conventional dielectric feedback lasers is that while conventionally the dielectric perturbation is weak and non-resonant, for plasmonic systems the scattering strength per unit cell of the lattice is very strong, and moreover presents a resonance. For a periodically corrugated waveguide with a weak periodic grating the mode structure is well understood through coupled mode theory as a "nearly-free photon" bandstructure with very narrow stop gaps [19]. However, for plasmonics the strong scattering strongly modifies the band structure. One practical advantage is that strong scattering implies broader stop gaps, which corresponds to smaller Bragg scattering lengths, or equivalently, much smaller required device sizes for lasing, and large robustness to disorder.

In Chapter 2 we presented the first experimental observation of the plasmonic band structure underlying lasing in a plasmonic lattice laser. However, in that study, the plasmonic particles were off resonance with the gain window and with the lasing condition set by the lattice periodicity. Here we overcome this limitation, and present a systematic study of the band structure underlying lasing as the plasmon resonance is tuned to the lasing condition. We identify a systematic dependence of the stop gap width on scattering strength of the particles. Moreover, we find that as the plasmon resonance crosses through the lasing condition, the loss characteristics of bands interchanges, and as a consequence also the stop gap edge at which lasing condition occurs moves from the low to the high end of the gap. These findings are in excellent accord with an electrodynamic point dipole model that accounts for near field and far field interactions between the particles as mediated by the waveguide structure.

3.2 Choice of sample geometry

Our experimental system (Fig. 3.1) is composed of silver particle arrays in a square periodic array, that have been fabricated by electron beam lithography on standard

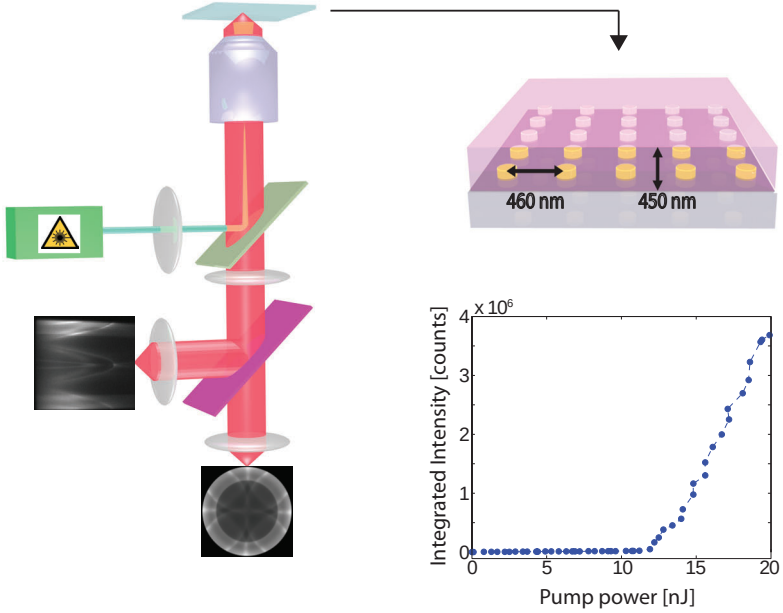

Figure 3.1: Schematic of the set up (left), a sample (upper right), and a typical threshold plot (lower right image). The set up is a simple fluorescence microscope. The simplified sketch shows the objective through which we excite and detect, the dichroic mirror (green), the fourier lens, a flip mirror to select either the spectrometer or the CCD camera and the tube lenses. Single shot excitation is done with a green laser (532 nm). An epilens is used to focus the excitation light into the back focal plane of the objective, so that we obtain wide field illumination at the sample. The resulting excitation spot has a diameter of 70 μm. The samples consist of square silver particle nanodisk arrays fabricated on a coverslip, embedded in a dye doped photoresist. The plot shows integrated emission intensity as a function of excitation power for the case of a Rh6G:Rh700 dye mixture, pitch of 460 nm (lasing at 710 nm), and a particle of 74 nm in diameter. A clear lasing threshold is visible at 12 nJ.

glass coverslip (Menzel, borosilicate), and that are embedded in a high index polymer layer (SU8). We study cylindrical particles with varying diameter (about 60 to 120 nm), and a height of about 30 nm, deposited by thermal evaporation (rate 0.5 Å/s) and defined through a standard lithography and liftoff process using ZEP. After fabrication the particles are covered in an approximately 450 nm thick film of SU8 that is first doped with dye. By ellipsometry we verified that the dye doped films have a refractive index of around 1.60. According to a waveguide mode calculation, the slab supports a single TE and a single TM mode that both have an effective index of about 1.55. The dye-doped SU8 film is prepared by spincoating from a solution that is prepared by mixing equal parts of SU8-2005 (SU8 in cyclopentanone, 45% solids, Microchem) and

cyclopentanone in which the dye is mixed. The dye solutions were prepared to contain 5 mM of Rh6G, as well as Rh700 in 0, 0.5, 3, 5 and 10 mM concentration. If one assumes that after spincoating only the cyclopentanone remains, this means that dye concentrations in the film are approximately 2.2 times the nominal dye concentrations we start with. This chapter mainly considers the 5mM/5mM Rh6G+Rh700 samples, meaning that the gain medium lies just above 700 nm wavelength. For these samples we use a pitch of 460 nm. We also discuss selected data for samples with Rh6G only, taken from Chapter 2 with pitches from 360 to 400 nm.

The rationale of these choices is that according to second order Bragg diffraction the lasing condition will occur at $\lambda_{\mathrm{Bragg}} = n_{\mathrm{WG}} d$, where λ stands for wavelength in vacuum, and n_{WG} for waveguide mode index. Thus the $d = 460$nm samples should provide lasing near 700 nm, at the maximum Rh700 emission. As we tune the particle diameter from 50 to 120 nm, the plasmon resonance will sweep from just above 600 nm towards, and through (diameter 110 nm) the lasing condition. Thus, by tuning the particle diameter, we will sweep from a strong red detuning between lasing condition and plasmon resonance to zero detuning. We note that as the particle diameter is changed, this changes the scattering strength at the lasing condition *both* because there is simply more polarizable matter per particle *and* because the resonance shifts. Since previously we established that only silver gives advantageous results for plasmon lasers, owing to the much higher loss in other metals such as gold, this study focuses on silver particles. We note that with the Rh700 dye, blue detunings are not accessible in the sense that for even larger particles, the resonance shifts no further, scattering strength saturates, and multipolar effects set in. As an additional dataset, therefore, we also present data where we sweep the lasing condition over the blue flank of the resonance, and use Rhh6G as gain medium.

3.3 Spectroscopy setup

We perform fluorescence microscopy measurements that are wave vector resolved [20]. The sample is placed on an inverted optical microscope (Sketch Fig. 3.1). We use a 100× Nikon objective, NA=1.45, Plan Apo) and excite in an epi-illumination configuration (spot size 40 μm) using 532 nm light that is offered in a 0.5 ns pulse (Teem Photonics, type STG-03E-1S0). The energy per pulse used to excite the sample is computer-controlled via an acousto-optical modulator in the range 0-20 nJ. We collect wavelength-resolved fluorescence Fourier images by imaging the objective back focal plane on the entrance plane of an imaging spectrometer (Shamrock 303i), making sure that the back focal plane image is centered on the slit. A sensitive silicon CCD camera (Andor iVAC) of 200 by 1650 pixels triggered by the laser pulse controller allows to collect single shot images of fluorescence as function of emission frequency $\omega = 2\pi c/\lambda$ and as function of emission wave vector k_x (at $k_y = 0$). In addition to single-shot Fourier imaging above and below threshold, we have also performed reference spectroscopy and fluorescence lifetime measurements on dye-doped films without plasmon particles to calibrate the dye system. In these measurements the light source

was a ps-pulsed, 10 MHz repetition rate Nd:YVO_4 laser (Time Bandwidth products), and we used a silicon CCD-spectrometer system (Acton 2303i, Pixis 100B) to collect spectra, and IdQuantique silicon avalanche photodiodes connected to a Becker-Hickl DPC230 correlator for time-correlated single-photon counting.

It should be noted that in this Chapter we will not deeply discuss any *above*-threshold data. As example to show that lasing does occur, Fig. 3.1 shows an exemplary input-output curve, for a sample with particle size $2r = 74$ nm in diameter, lasing at 710 nm, using the Rh6G:Rh700 dye mixture as gain medium. We have verified that for all particle sizes, the systems lased, with a lasing threshold that does not depend strongly on particle size. Below we will discuss the underlying below-threshold band structure.

3.4 Spectroscopy of constituents & FRET

Figure 3.2 shows reference results for the gain medium as well as for the plasmon particles. Figure 3.2 (a) shows the calculated extinction cross section for silver particles in the glass/SU8/air system of interest, that we performed using finite difference time domain software (Lumerical), using a Drude-Lorentz fit to the 200-800 nm range of optical constants for silver measured by Weaver et al. [21]. Results shown are for normal incidence from the glass slide, using perfectly matched layer absorbing boundary conditions on all sides of the domain. Notably, as the particle size increases the scattering strength drastically increases, and furthermore exhibits the well-known shift to longer wavelengths due to dynamic depolarization effects [22–24]. For $d >$ 60nm, the dipolar resonance has a distinct Lorentzian shape, and is well separated from the features at wavelengths $\lambda < 500$ nm, that are not due to the material free electron response. Comparison of the cross sections at the expected lasing condition $n_{\mathrm{WG}} d \approx 710$ nm shows that sweeping particle size will sweep the scattering and extinction cross section from below 0.01 to almost 0.07 μm^2. To put it in perspective, this cross section goes from 5% to 30% of the unit cell area, and becomes comparable to the largest scattering strength $3/2\pi(\lambda/n)^2 \approx 0.09$ μm^2 possible for a dipole scatterer.

Regarding the spectral properties of the dye mixture, Figure 3.2(b) shows emission spectra at fixed Rh6G concentration, and various Rh700 nm concentrations. Emission at the short wavelength end is clipped by a 540 nm longpass filter that blocks the 532 nm excitation light. Evidently the strong Rh6G emission band (550 to 620 nm) rapidly decreases in intensity as Rh700 is mixed into the film, while at the same time strong emission of the Rh700 dye (650 to 750 nm band) arises. At a one-to-one ratio (where the nominal dye concentrations prior to mixing with SU8 is 5 mM) the Rh6G emission has almost completely vanished. For larger concentration of Rh700, the Rh700 emission decreases, and redshifts. We hypothesize that the disappearance of Rh6G emission and the appearance of Rh700 fluorescence, that is poorly pumped by 532 nm directly, is a consequence of Förster Resonance Energy Transfer" (FRET), while the concentration quenching of Rh700 at elevated concentration is due to energy

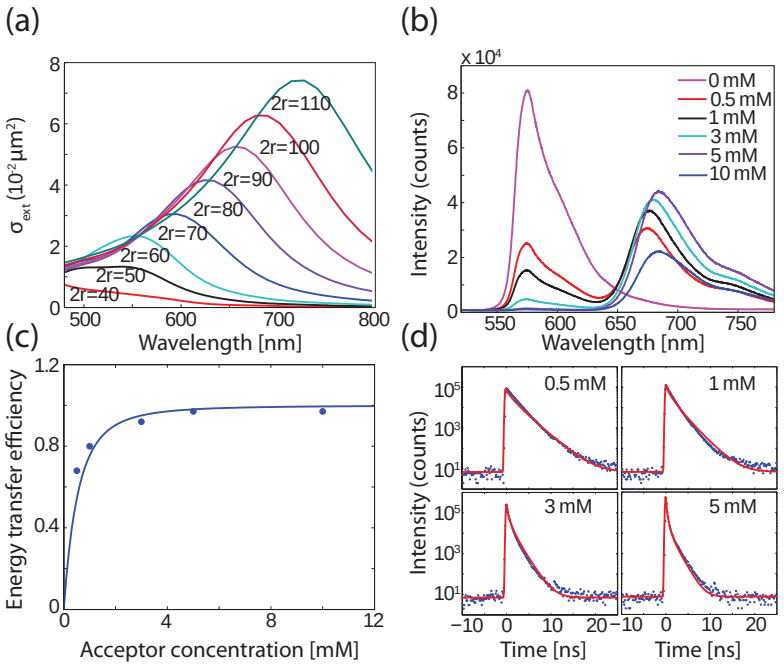

Figure 3.2: (a) Extinction cross sections for Ag disks of 30 nm height in SU8 on glass, according to Lumerical, using tabulated optical constants. (b) Spectra of dye mixtures. Here the concentration of Rh6G is fixed to 5 mM and the concentrations given in the figure represent Rh700 concentrations. (c) FRET efficiency curve. The horizontal axis represents the concentration of Rh700, and the vertical axis represents energy transfer efficiency from the donor to the acceptor. The data points are for a Rh700 concentration of 0.5 mM, 1 mM, 3 mM and 5 mM, resp. where the Rh6G concentration is kept at 5 mM. (d) Lifetime traces. The solid curves plotted through the data points are FRET theory where no adjustable parameter is used except a vertical scaling.

transfer between Rh700 fluorophores, after they have received their excitation from Rh6G.

To verify that excitation of Rh700 is indeed via FRET, we examine spectra and fluorescence decays. As usual [25] we define the energy transfer efficiency as

$$E = 1 - \frac{F_{DA}}{F_D}$$

where F_D is the integrated (detector-corrected) spectral intensity of the donor-only sample, while F_{DA} is the integrated spectral intensity of the acceptor. Figure 3.2(c) shows the energy transfer efficiency deduced from the data in (b) as a function of the nominal concentration (symbols) alongside the textbook prediction for E that is appropriate for FRET in 3D homogeneous random ensembles [25–27]

$$E = -\sqrt{\pi}\gamma e^{\gamma^2}(1 - \mathrm{erf}\gamma).$$

This expression depends only the dimensionless concentration C/C_0

$$\gamma = \frac{\Gamma(1/2)}{2}\frac{C}{C_0} \quad \text{with} \quad C_0 = \left(\frac{4}{\pi}R_0^3\right)^{-1},$$

where Γ represents the Gamma-function. This expression provides a reasonable fit to the data for a critical concentration $C_0 = 0.9$ mM. Since we quote nominal concentrations in the dye solution *before* spincoating and solvent evaporation, the critical concentration can not be directly translated into a Förster radius R_0 for the Rh6G:Rh700 donor-acceptor pair in SU8. However, assuming that after evaporation the SU8:dye ratio remains constant, we can convert the critical concentration to a critical concentration of 2.2×0.9mM *in* the SU8, which in turn translates to a Förster radius of about 5.5 nm. Since this is on par with expected Förster radii [25], we thus conclude that the concentration dependence of spectra is consistent with FRET.

As independent check, we have also measured fluorescence decay traces of the donor emission (donor emission selected by a bandpass filter). If energy transfer is due to FRET, decays should be given by [26]

$$I_D(t) = I_0 \exp\left[-t/\tau_D - 2\gamma(t/\tau_D)^{1/2}\right] \tag{3.1}$$

where τ_D is the donor decay time. Figure 3.2(d) shows measured decay traces at the various concentrations alongside the prediction Eq. 3.1 convoluted with the instrument response function of our setup. We note that for this comparison we only adjust the overall scaling I_0, but adjust neither $\tau_D = 3.4$ ns which is taken from a donor-only measurement, nor γ, which is taken from the spectral data. We note excellent correspondence, especially given that no parameter except overall scaling was adjusted, further confirming FRET.

To summarize this comparison of numerical analysis and data, we identify the one-to-one 5 mM sample as most suited for our gain measurements as it provides strong Rh700 emission by FRET from Rh6G pumped by our 532 nm pump laser.

3.5 Polarization resolved band diagrams

Distributed feedback lasing in our samples is understood to originate from lasing into a waveguide mode of the polymer slab that enjoys Bragg diffraction from the particles [1, 28]. Since the polymer slab supports two modes, the fundamental TE and fundamental TM mode, it is important to determine on which waveguide mode the system operates. To this end we have performed band structure measurements on many samples using a linear polarizer in front of the spectrometer slit. To understand the measurement scheme, we refer to a sketch of the expected repeated zone scheme dispersion relation in the limit of weak scattering. Fluorescence is expected to dominantly be emitted into the waveguide mode, i.e., at (parallel, in plane) wave vector $|\mathbf{k}_{||}| = n_{\mathrm{WG}}\omega/c$. Since back focal plane imaging directly maps $\mathbf{k}_{||}/k_0$, this would appear on our detector as a ring that is $n_{\mathrm{WG}} = 1.55$ times bigger then the free space light cone, if it weren't for the fact that the

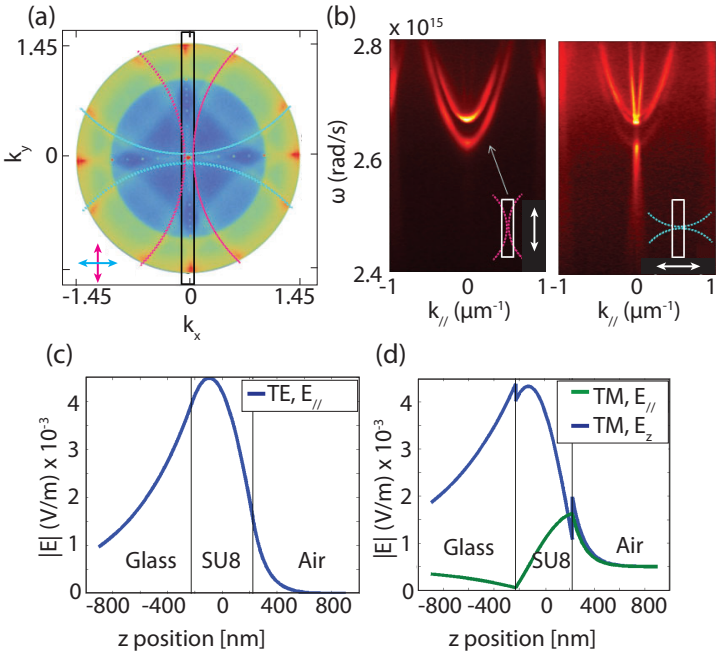

Figure 3.3: (a) Sketch of the measurement geometry: using the spectrometer slit (overlaid as elongated black frame on a typical 2D Fourier image), we collect a slice at $k_x = 0$ of $k_{||}$-space. Diffracted modes appear as circles centered at reciprocal lattice vectors in the back focal plane. As function of frequency the magenta circles will form the parabola, while the cirles indicated in blue trace out straight lines in the measured $\omega - k$ diagrams. If features are due to TE-waveguide modes, the polarization vector is tangential to the circles. (b) Polarization-resolved dispersion measurements. Figure (a) and (b) show measurements for a particle pitch of 460 nm and a particle diameter of 86 nm. Panel (c) shows the electric field of the TE-waveguided mode, while panel (d) shows the electric field distribution of the TM-waveguided mode. The latter has field E_z perpendicular to the layers, and in-plane field $E_{||}$ along the wave vector.

objective clips the signal to $\mathbf{k}_{||}/k_0 < 1.45$. Bragg diffraction causes the waveguide mode circle to be replicated every reciprocal lattice vector $\mathbf{G} = 2\pi/d(m,n)$ (with m,n integer), so that the back focal plane image appears as a set of intersecting circles of radius $1.55k_0$. In our measurement we only collect a slice along one axis (labelled k_y), spectrally dispersing the fluorescence from this slice over the other axis of our CCD camera. In such a measurement, the diffracted orders $\delta(|\mathbf{k}| - k_0 n_{\mathrm{mode}}) \pm 2\pi/d(0,1)$ appear as straight lines that intersect at $k_y = 0$ for the 2nd order Bragg diffraction conditions. In contrast, the diffracted orders $\delta(|\mathbf{k}| - k_0 n_{\mathrm{WG}}) \pm 2\pi/d(1,0)$ appear as (two degenerate) parabola's, that have their minimum at the 2nd order Bragg diffraction condition. If the dominant waveguide mode is TE (TM) polarized, i.e., tangential (radial) to the mode circles, this reasoning implies that a polarizer along the spectrometer slit will only pass

through the parabolic (linear) bands, while conversely the crossed polarizer setting will select the linear (parabolic) bands.

Figure 3.3(b,c) shows measured ω, k diagrams of fluorescence emission below threshold for polarization settings along and crossed to the spectrometer slit. As expected, the measurements (summed together) display two linear bands, as well as the expected parabolic feature, with the area of the band (anticrossing) centered around $2.63 \cdot 10^{15}$ s^{-1} (715 nm, in accord with $1.55d$). The measurements show that only the crossed polarizer setting passes the linear bands, whereas the parabolic bands are most distinct when the polarizer is along the spectrometer slit. This observation confirms that while emission might occur into both TE and TM modes, the emission that is coupled out to free space by the plasmon particles dominantly originates from the TE mode. This observation is consistent with our earlier observation that *above* threshold the lasing appears as a TE-polarized donut beam, and can furthermore be explained using mode profile calculations [29]. As 3.3(d,e) show, both the TE and TM mode present a strong field near the glass/SU8 boundary where the particles are situated. However, only the TE mode has a strong electric field component in the plane of the particles, along the main polarizability tensor axes of the plasmon particles. The TM mode only provides field along the sample normal, i.e., along which the silver disks are not polarizable.

3.6 Band structure and stop gap width

The most notable feature in Fig. 3.3(b,c) that is distinct from the sketched free photon folded dispersion relation is that the two parabolic bands are not degenerate but distinctly split. In addition, the linear bands also show a stop gap, with band edges coincident with the minima of the parabola. Figure 3.4(a-f) shows the progression of this band structure as we increase particle size. Clearly, the band structure stays qualitatively identical up to a particle size of 86 nm diameter, however, with a distinct increase in stop gap width. For particles above 95 nm in diameter, the band structure develops a qualitatively different appearance, both in terms of avoided crossing geometry, and in terms of the widths of the various bands.

Before discussing these more subtle features, we plot the stop gap width versus particle diameter (figure 3.4g). In this diagram error bars on particle size are taking as the standard error from many electron microscopy size determinations, while the error in stop gap width represents a conservative estimate of the error in reading of the band edges from the CCD images. Evidently the stop gap width systematically rises with particle diameter (data shown for two distinct sample substrates). Plotted alongside the data (red curve, rightmost axis) we display the extinction cross section according to Lumerical at the wavelength of the band anticrossing. We conclude that there is a strong correlation between the calculated cross section and the measured stop gap width.

Such a relation between stop gap width and a scattering parameter such as cross section is not unexpected, in the sense that it has been well known since the late 1990's

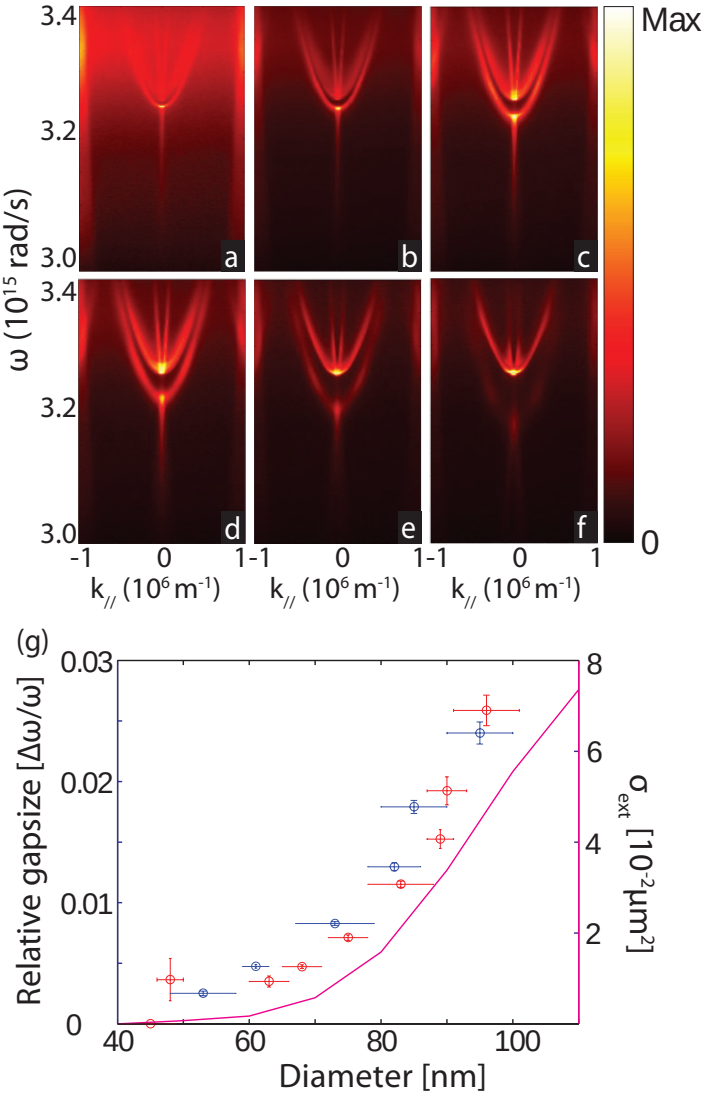

Figure 3.4: Measured $\omega - k$ diagrams as function of plasmon particle diameter, where the diameter varies from 53 (a), 61 (b), 74 (c), 82 (d), 86 (e) to 95 ± 5 (f) nm, for samples with pitch $d = 460$ nm, using the Rh6G:Rh700 dye mixture, taken below threshold. Maxima are 5350 (a), 8600 (b), 11650 (c), 14300 (d), 25200 (e), and 27950 (f) counts/μJ/shot, respectively. Panel g represents measured relative gapsize versus particle diameter (blue and red points, referring to two separate data sets). The line indicates the extinction cross section per particle (right-hand y-axis) calculated with Lumerical, evaluated at the lasing wavelength.

that in dielectric photonic crystals of spheres the relative stop gap width is given by [30]

$$\frac{\Delta\omega}{\omega} = 4\pi\frac{\alpha}{V} \tag{3.2}$$

where α stands for polarizability (real and positive for dielectric spheres), and V for the unit cell volume. At first sight it stands to reason that a similar relation holds in 2D plasmonic systems. However, we remind the reader that in the plasmonic case the physics is much richer, since α is a complex quantity, while stop gap widths must obviously be real and positive. There is no currently available theory that reports the equivalent of Eq. 3.2 for stop gap width in terms of scattering parameters of plasmon particles.

In an attempt to bring out the dependence of stop gap width on scattering strength more clearly, we have constructed a "master diagram" that combines the data obtained here with the Rh6G-Rh700 FRET pair, and the data obtained earlier with just Rh6G. For the master diagram we use a normalized frequency detuning parameter, i.e., the detuning between particle plasmon and lasing wavelength $\omega_{\mathrm{LSPR}} - \omega_{\mathrm{lasing}}$, normalized to the bandwidth of the plasmon resonance (FWHM Γ_{LSPR}). Note that this is the only apparent relevant linewidth to normalize to in our system. The relevant single-particle frequency and linewidth are obtained by fitting a Lorentzian to the simulated particle response (specifically, to $\sigma_{\mathrm{scat}}\lambda^4$, which should be proportional to $|\alpha|^2$.) The data in Fig. 3.4 taken with the Rh700 as gain medium, appears at negative detuning, and we remind the reader that to take it we kept lasing frequency ω_{lasing} fixed (fixed pitch), and particle size tuned the plasmon resonance ω_{lasing} from the blue side onto the lasing condition. For positive detuning, we plot data taken with a fixed particle size of 110 nm, varying pitch from 360 to 400 nm and using Rh6G as gain medium, reported in Chapter 2. In this second set, the particle size was fixed and the lasing wavelength was swept over the blue edge of the plasmon resonance by varying pitch.

The resulting stop gap width clearly drops when detuning in either direction away from zero detuning, however, in an asymmetric fashion. Stop gap widths are about three times higher for detunings to the blue of the resonance, then for equal detuning to the red of the resonance. Such an asymmetry could be expected, in the sense that if even if one starts with a Lorentzian polarizability $\alpha(\omega)$, the scattering response of a plasmon particle is asymmetric in frequency. In particular, suppose we take

$$\alpha_{\mathrm{static}}(\omega) = \frac{V\omega_0^2}{\omega^2 - \omega_0^2 - i\omega\gamma}$$

(in CGS units, with ω angular frequency, ω_0 the particle resonance, γ an Ohmic damping rate, and V an (effective) particle volume) to describe the electrostatic polarizability of a small particle that is composed of a Drude model [31] To turn this polarizability into that of a physical scatterer one must include radiation damping [32]

$$\frac{1}{\alpha} = \frac{1}{\alpha_{\mathrm{static}}} - i\frac{2}{3}k^3$$

(with $k = n\omega/c$), from which one can then calculate the scattering cross section

$$\sigma_{\text{scatt}} = \frac{8\pi}{3} k^4 |\alpha|^2$$

Fig. 3.5 shows data alongside this scattering cross section, plotted taking an archetypical Ohmic damping for silver ($\gamma = 0.05\omega_0$) and particle volume chosen to obtain a scattering cross section at 80% of the unitary limit ($3/2\pi\lambda^2$), which is on par with the scattering strength of plasmon particles of sufficient size (diameter above 50 nm). The stop gap width correlates well with the scattering cross section (as well as with the extinction cross section, since for this choice of parameters scattering dominates extinction) which shows a similar asymmetry. For reference, in blue the cross section from simulations is reproduced.

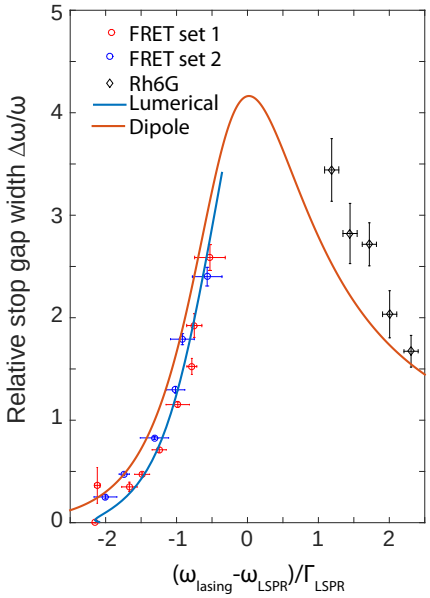

Figure 3.5: Stop gap width versus normalized detuning between plasmon resonance and Bragg diffraction wavelength. Points in red and blue have been taken from Fig. 3.4 (Rh700 sample, large pitch), while the black points at positive detuning are obtained from Chapter 2. The red line represents the scattering cross section expected in a dipole model, while in blue the cross section versus diameter from Lumerical calculations is shown that is also plotted in Fig. 3.4. Note that the cross sections have been scaled. At its peak, the cross section of the red curve equals 80% of the unitary limit.

3.7 Band structure topology versus detuning

We now turn to discussing more detailed features of the measured dispersion relations beyond just the stop gap width. Figure 3.6 shows three measured dispersion diagrams. Panel a, shows a dispersion diagram taken from Chapter 2, obtained on a sample that has the lasing condition well to the blue of the localized surface plasmon resonance (Rh6G sample, $d = 380$ nm, 55 nm diameter particle). Panel c shows a dispersion diagram for the converse case, i.e., with the lasing condition well to the red of the plasmon resonance (case (e), Fig. 3.4). The panel in the middle, finally, corresponds to a case where the lasing condition is aligned to the plasmon resonance (Rh700 sample, particle diameter 129 nm).

We note the following progression in the data. First, when lasing is well to the red of the localized surface plasmon resonance, the lower and upper parabola have their minima coincident with the maximum and minimum of the anticrossing linear dispersion relations. Lasing in these samples dominantly occurs on the upper band edge. The fact that the parabola and the anticrossing lines share a common gap is consistent with the scalar coupled mode theory for dielectric DFB lasers (outlined for plasmon lasers by van Exter et al. [33, Fig. 4b] in the limit that coupling by $\mathbf{G} = 2\pi/d(0,\pm1)$ and $(\pm1,0)$ dominates, and $(\pm1,\pm1)$ scattering is weak. For small particles and large red detunings the upper parabolic band is slightly broader than the lower parabolic band is narrow. For the opposite-detuning case, i.e., panel (a) in which lasing occurs to the blue of the particle resonance, again two split parabola, and two anticrossing linear bands are retrieved, now with the upper parabola consistently very broad. For these samples lasing occurs on the lower stop gap edge instead of the upper stop gap edge.

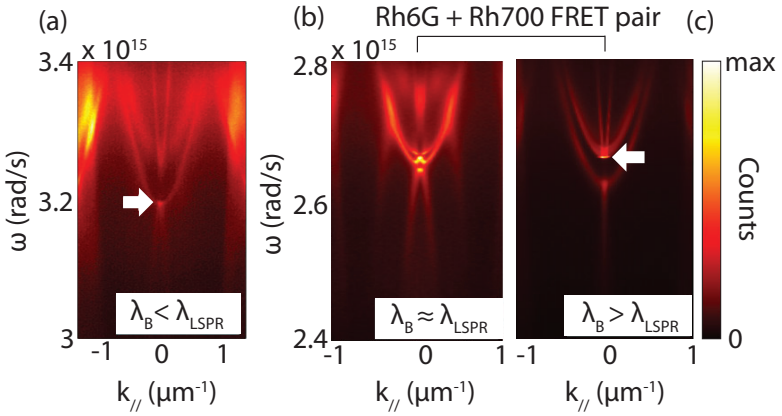

Figure 3.6: Generic $\omega - k$ diagrams for three cases: lasing condition blue-detuned, red-detuned, and centered on the plasmon resonance (panels a, c and b). These concern $d = 380, 2r = 55$ nm (panel (a)), $d = 460, 2r = 129$ nm (b), and (c) $d = 460, 2r = 86$ nm. For panel (a) we used Rh6G only, while the other panels used the $Rh6G : Rh700$ FRET mixture. White arrows indicate the $\omega - k$-point on which the system lases first.

Finally, when the particle plasmon and lasing condition coincide, i.e. panel b in Figure 3.6 the band structure is markedly different. The minimum of the lower parabola is pushed below the frequency range of the measurement, and a set of additional features has appeared that can not be trivially traced to the original four-band crossing in a coupled-mode/slightly perturbed free-photon picture.

3.8 Theoretical considerations

To summarize these phenomenological observations, we have established the following facts that any theory must address:

1. Lasing occurs at the 2nd Bragg diffraction order stop gap on the TE waveguide mode.
2. For detunings of at least half a linewidth away from the plasmon resonance, whether to the blue or red of the resonance, the dispersion relation is reasonably described by a perturbed free photon dispersion relation (best correspondence in the red detuning case).
3. In this regime the stop gap scales with scattering strength, as quantified by an extinction or scattering cross section.
4. The lasing condition is on the stop gap edge closest to the plasmon particle resonance, meaning it swaps edge when flipping the sign of the detuning.
5. When Bragg condition and localized plasmon resonance coincide, the dispersion relation is far from close to a perturbed free photon dispersion relation.

We note that it is a surprisingly challenging problem to build a theory for this system. Coupled mode theory [19, 33] would treat the particles as a weak perturbation, and is essentially valid only for small dielectric perturbations. Hence it will certainly not deal with the case of plasmon resonance and Bragg condition aligned. Also it is unclear how to connect mode coupling parameters to single particle scattering strengths. In principle, the response of 2D lattices of plasmon particles has been succesfully modelled by point-dipole methods [32], where retarded dipole-dipole interactions are accounted for using Ewald lattice summation. Extending this method to deal with stratified background media, i.e., the glass/waveguide/air system, is a challenge in itself, but has been accomplished by several workers [34–36]. This method, however, only provides the response in terms of transmission, reflection, and diffraction, to external driving. If one would want to model lasing, one should include actual gain in the system, as well as spontaneous emission noise to kickstart the lasing process [37]. Slightly less ambitious would be to not model the lasing itself, but to model the passive-system band structure [38]. A dispersion relation by definition is the set of frequency-wave vector points at which the system has a finite response to infinitesimal driving. However, here one should realize that we are working with a system that has radiative and strong

absorptive loss. In presence of loss, no real-frequency, real-wave vector dispersion exists [39, 40]. In fact, for the emission experiment, it is a challenge to define how the observable relates to a generalized dispersion relation in which either frequency or wave vector is chosen real [41].

The regime that seems most amenable for theoretical interpretation is that of large detuning. The most unique aspect that appears is that the stop gap edge on which lasing occurs swaps from being at the red to the blue stop gap edge, when detuning the lasing condition from the red to the blue of the plasmon resonance. A likely explanation comes from the field of photonic crystals, where it is well known that the modes at the stop gap edges are standing waves that have their field energy density at different locations in the unit cell. For photonic crystals the band defining the lower edge is generally known as "dielectric band", while the upper band is called "air band" to reflect that the associated modes reside primarily in the high, resp. low index layer. Similarly one can hypothesize that in plasmonic crystals near the band edge one band will reside at, and one band will reside away from the plasmon particles. The energetic ordering of these two bands could then be expected to flip when the sign of the scattering potential,

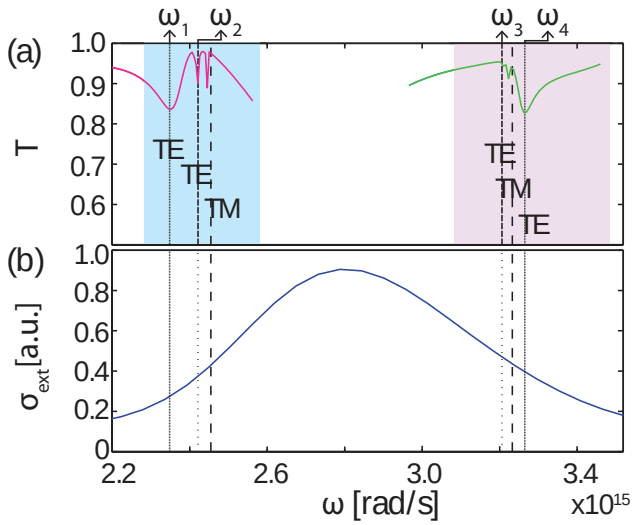

Figure 3.7: The blue curve in the lower panel shows the extinction cross section for a single silver disk with a height of 30 nm and a diameter of 100 nm on a substrate with index n=1.46, embedded in a waveguide with a refractive index of 1.65 and a thickness of 450 nm. The curves in the upper panel show transmission for an array of these particles with a pitch of 500 nm (pink) and 370 nm (green). The pink and blue areas represent the frequencies limited by $\omega = 2\pi c n_{mat} d$ with n_{mat} =1.65 and 1.46 for both pitches, that would correspond to grazing angle grating coupling into solid SU8, or the glass. The dotted lines show the frequencies for which the waveguide mode without particles has a TE and a TM mode, as indicated. The broad dip at ω_1 and ω_4 is associated to the lower band edge for a pitch of 500 nm and to the higher band edge for a pitch of 370. We indicate their complementary band edge by ω_2 and ω_3, respectively.

i.e., the polarizability α flips, which occurs as one goes from negative to positive detuning. Lasing would then likely occur at the band with the least loss, that resides away from the particles. In this picture it is also evident that common photonic crystal, i.e., free-photon dispersion perturbation theory, fails at zero detuning, as it can not deal with imaginary polarizability.

As example of the merits and difficulties of interpreting numerical simulations to understand the band structure physics, we consider a COMSOL 3D finite element simulation. In this simulation we assume as structure a square lattice of silver particles in a glass/waveguide/air system. As indices we take 1.46/1.65/1.0 - although the actual glass we use is not quartz but fused silica (n=1.52), and the SU8 index from ellipsometry is actually 1.60, not the datasheet value of 1.65. The reason for this choice is that it provides much easier interpretation of diffraction calculations, in that it provides a larger separation between the waveguide mode indices, and the glass index. We found that otherwise it is difficult to separate diffractive coupling into glass, resp. into the waveguide. As particles we assume silver disks of height 30 nm and diameter 100 nm, using the modified Drude model discussed in Chapter 2, Eq. (2.1). We have performed calculations on three systems. First, we have calculated the scattering and extinction cross section under normal incidence illumination as function of frequency for a single particle, using a total field/scattered field simulation with scattering boundary conditions. We find a strong resonance at $\omega = 2.76 \cdot 10^{15}$ s^{-1}, i.e., about 680 nm. Next, we implemented Bloch-Floquet boundary conditions to obtain the diffractive properties of periodic systems driven by a plane wave incident from the glass side. In this simulation we simulate approximately two wavelengths deep into the air and glass, now using so called periodic port boundary conditions for all the propagating diffracted orders. It should be noted that these simulations need about 10 minutes per frequency point. We have studied two pitches, i.e. 500 nm and 370 nm, to obtain diffractive coupling to the waveguide, i.e., to hit the 2nd order Bragg condition, on either side of the resonance. Figure 3.7 shows the transmission in a small frequency range around the diffractive coupling condition for both pitches. The curves present the following three features. First, the generally high transmission is dominated by a relative broad (though still narrow compared to the plasmon resonance) asymmetric minimum that has the appearance of a Fano lineshape. Second, the spectra show two extremely narrow features. The frequency at which the two narrow features occur match very well with diffractive coupling to the TE and TM waveguide mode, i.e., to $\lambda_0 = n_{\mathrm{WG}} d$ with n_{WG} the TE and the TM waveguide mode index from a waveguide mode solver (1.588 resp 1.575 and 1.5561 resp 1.53 for the TE resp. TM mode for the cases $d = 370$ nm, resp $d = 500$ nm). This analysis, of transmission in itself already highlights an interesting difficulty. The spectra plotted in figure 3.7 have been calculated assuming slightly off-normal incidence (angle of 0.5° in air). At *exactly* normal incidence the narrow TE feature exactly vanishes, evidently not because the mode vanishes but because coupling to it is forbidden by symmetry. It is a general problem of any analysis tool like COMSOL that it is difficult to obtain "eigenmodes" without reference to a driving field.

Our interpretation of the result is the following. The lasing features we observe are, according to our experiment, due to the TE mode. Hence the TM feature is of no relevance, but the other two features in the spectrum apparently indicate the lower, and upper stop gap edge for the TE dispersion relation that we measured. In this interpretation, which we validate below, it is relevant to note that for the large-pitch case $d = 500$ nm, the broad minimum occurs at lowest frequency ($2.34{\cdot}10^{15}$ s^{-1}), while the narrow TE feature occurs at a frequency that is about 3% higher ($2.42{\cdot}10^{15}$ s^{-1}). For the small-pitch case, where the Bragg condition is to the blue of the plasmon resonance, the ordering is reversed. The tentative interpretation is that lasing always occurs on the narrower band of the two, and that in both cases the narrow band has its corresponding mode profile away from the particle (away from Ohmic loss), while the broad band edge has its corresponding Bloch mode at the particles. This claim then implies that as one goes through the polarizability resonance the energetic ordering of the mode swaps.

To verify the assertion regarding the nature of the narrow and broad mode, one would want to examine eigenmode field profiles. However, these are not accessible as we examine a driven system. Instead, we need to plot either a vector component of the full field we calculated at the resonance frequencies, or to consider scattered field. We found examining scattered fields (i.e., full field, minus the field that we calculate in absence of the particle) brings out the physics best, as one is not distracted by the trivial standing wave patterns in thin film interference that the incident field itself contains. However, we warn the reader that scattered fields by themselves are *not* solutions of the Maxwell equations. Only for cases where a strong resonance is excited, is a scattered field approximately an eigenmode solution.

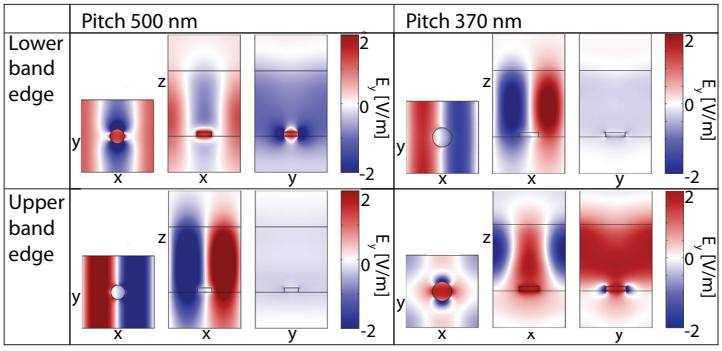

Figure 3.8: Crosscuts in the xy plane and xz plane through a particle which is in a particle array. Shown are the field plots for frequencies at the lower and upper band edge, for a pitch of 370 nm and 500 nm. Plotted is $E_y - E_{y,in}$. The incident field strength is 1 V/m. These frequencies are obtained from the plot in 3.7, where they are denoted as $\omega_1 = 2.35 \cdot 10^{15}$ s^{-1} (upper left plots), $\omega_2 = 2.42 \cdot 10^{15}$ s^{-1} (lower left plots), $\omega_3 = 3.21 \cdot 10^{15}$ s^{-1} (upper right plots) and $\omega_4 = 3.27 \cdot 10^{15}$ s^{-1} (lower right plots).

Figure 3.8 shows field profiles in the xy-plane through the particle, as well as vertical xz and yz cuts through the system, for both pitches and for both the sharp and narrow TE feature. We plot the field component E_y along the incident polarization. The resulting diagrams confirm the hypothesis about the field distribution that we posed. First, the vertical cuts show the typical mode profile of a TE mode in the transverse direction, indicating that our mode assignment was correct. This is not surprising for the narrow feature that exactly coincides with $\lambda_0 = n_{\mathrm{TE}} d$, but it validates that the broad minimum in transmission is the other TE-mode stop gap edge. At the frequency of the narrow feature, the scattered field has a nodal plane at the particle, and resides mainly away from it. Conversely, at the broad minimum in transmission, the associated field plot shows strong excitation of the particle.

To conclude, in our measurement we have observed that lasing occurs on the blue stop gap edge when the lasing condition is on the red flank of the particle resonance, and vice versa lasing occurs on the red stop gap edge when the Bragg condition is to the blue of the particle resonance. The COMSOL simulation corroborates the interpretation that lasing simply selects the stop gap edge that corresponds to the Bloch mode that forms a standing wave with energy density away from the particle. As one goes through resonance, the stop gap edge to which this standing wave corresponds is reversed. This stands to reasons when one realizes that going through resonance, the real part of the polarizability flips sign. We note that an interesting follow up study would be to analyze also coincidence of the Bragg condition with the polarizability resonance. Likely this would require mapping not just frequency, but also incident angle, to disentangle the various effects, especially as the TE and TM mode structure could mix, and as the splitting could get so large that the polarizability can no longer be seen as approximately constant over the bandwidth of the gap.

3.9 Conclusions & outlook

In summary, we have shown how the optical response of plasmonic scatterers affects the band diagram of a system of plasmonic scatterers embedded in a dye doped waveguide layer. We have used a FRET pair to be able to excite our gain medium at 532 nm while obtaining emission around 700 nm. We have shown that the process facilitating this is FRET by measuring lifetime curves as a function of dye concentrations. We have performed polarization selective measurements regarding the band diagrams and found that emission is mainly TE polarized. In addition we have measured band diagrams as a function of particle size and found a strong dependence of stop gap size on particle diameter. Finally, we support our measurements using comsol simulations. Our work gives a clear agenda for theoretical efforts. These must at least account for the scaling of stop gap with scattering strength for large detunings, for the qualitatively very different band structure at zero detuning, and for more subtle features such as where the mode resides and what mode has least loss, depending on the choice of detuning. Experiments that could guide these theoretical efforts would for instance include studying variations in particle material, to independently vary loss and scattering.

References

[1] I. D. W. Samuel and G. A. Turnbull, *Organic semiconductor lasers*, Chem. Rev. **107**, 1272 (2007).

[2] G. Heliotis, R. D. Xia, G. A. Turnbull, P. Andrew, W. L. Barnes, I. D. W. Samuel, and D. D. C. Bradley, *Emission characteristics and performance comparison of polyfluorene lasers with one- and two-dimensional distributed feedback*, Adv. Funct. Mater. **14**, 91 (2004).

[3] G. A. Turnbull, P. Andrew, M. Jory, W. Barnes, and I. D. W. Samuel, *Relationship between photonic band structure and emission characteristics of a polymer distributed feedback laser*, Phys. Rev. B **64**, 125122 (2001).

[4] P. Del Carro, A. Camposeo, R. Stabile, E. Mele, L. Persano, R. Cingolani, and D. Pisignano, *Near-infrared imprinted distributed feedback lasers*, Appl. Phys. Lett. **89**, 201105 (2006).

[5] E. Mele, A. Camposeo, R. Stabile, P. Del Carro, F. Di Benedetto, L. Persano, R. Cingolani, and D. Pisignano, *Polymeric distributed feedback lasers by room-temperature nanoimprint lithography*, Appl. Phys. Lett **89**, 131109 (2006).

[6] S. A. Maier, *Plasmonics: Fundamentals and Applications*, Springer, 2007.

[7] G. M. Akselrod, C. Argyropoulos, T. B. Hoang, C. Cirac, C. Fang, J. Huang, D. R. Smith, and M. H. Mikkelsen, *Probing the mechanisms of large Purcell enhancement in plasmonic nanoantennas*, Nat. Photonics **8**, 835 (2014).

[8] C. Belacel, B. Habert, F. Bigourdan, F. Marquier, J.-P. Hugonin, S. Michaelis de Vasconcellos, X. Lafosse, L. Coolen, C. Schwob, C. Javaux, B. Dubertret, J.-J. Greffet, P. Senellart, and A. Maitre, *Controlling spontaneous emission with plasmonic optical patch antennas*, Nano Lett. **13**, 1516 (2013).

[9] E. J. R. Vesseur, J. F. Garcia de Abajo, and A. Polman, *Broadband Purcell enhancement in plasmonic ring cavities*, Phys. Rev. B **82**, 165419 (2010).

[10] S. Murai, M. A. Verschuuren, G. Lozano, G. Pirruccio, S. R. K. Rodriguez, and J. Gómez Rivas, *Hybrid plasmonic-photonic modes in diffractive arrays of nanoparticles coupled to light-emitting optical waveguides*, Opt. Express **21**, 4250 (2013).

[11] G. Vecchi, V. Giannini, and J. Gómez Rivas, *Shaping the fluorescent emission by lattice resonances in plasmonic crystals of nanoantennas*, Phys. Rev. Lett. **102**, 146807 (2009).

[12] A. G. Nikitin, A. V. Kabashin, and H. Dallaporta, *Plasmonic resonances in diffractive arrays of gold nanoantennas: near and far field effects*, Opt. Express **20**, 27941 (2012).

[13] P. L. Stiles, J. A. Dieringer, N. C. Shah, and R. R. Van Duyne, *Surface-enhanced Raman spectroscopy*, Annu. Rev. Anal. Chem. **1**, 601 (2008).

[14] M. E. Stewart, C. R. Anderton, L. B. Thompson, J. Maria, S. K. Gray, J. A. Rogers, and R. G. Nuzzo, *Nanostructured plasmonic sensors*, Chem. Rev. **108**, 494 (2008).

[15] J. N. Anker, W. P. Hall, O. Lyandres, N. C. Shah, J. Zhao, and R. P. Van Duyne, *Biosensing with plasmonic nanosensors*, Nat. Mater. **7**, 442 (2008).

[16] G. Lozano, D. J. Louwers, S. R. K. Rodriguez, S. Murai, O. T. A. Jansen, M. A. Verschuuren, and J. Gómez Rivas, *Plasmonics for solid-state lighting: enhanced excitation and directional emission of highly efficient light sources*, Light. Sci. Appl. **2**, e66 (2013).

[17] W. Zhou, M. Dridi, J. Y. Suh, C. H. Kim, D. T. Co, M. R. Wasielewski, G. C. Schatz, and T. W. Odom, *Lasing action in strongly coupled plasmonic nanocavity arrays*, Nat. Nanotechnol. **8**, 506 (2013).

[18] A. H. Schokker and A. F. Koenderink, *Lasing at the band edges of plasmonic lattices*, Phys. Rev. B **90**, 155452 (2014).

[19] H. Kogelnik and C. Shank, *Stimulated emission in a periodic structure*, Appl. Phys. Lett. **18**, 152 (1971).

[20] I. Sersic, C. Tuambilangana, and A. F. Koenderink, *Fourier microscopy of single plasmonic scatterers*, New J. Phys. **13**, 083019 (2011).

[21] J. H. Weaver and H. P. R. Frederikse, *CRC Handbook of Chemistry and Physics, Optical properties of metals and semiconductors* ;Weaver, J. H., and Frederikse, H. P. R., David RCRC Press, Florida, 1993-1994.

[22] L. Zhao, K. L. Kelly, and G. C. Schatz, *The extinction spectra of silver nanoparticle arrays: Influence of array structure on plasmon resonance wavelength and width*, J. Phys. Chem. B **107**, 7343 (2003).

[23] A. Bouhelier, R. Bachelot, J. Im, G. Wiederrecht, G. Lerondel, S. Kostcheev, and P. Royer, *Electromagnetic interactions in plasmonic nanoparticle arrays*, J. Phys. Chem. B **109**, 3195 (2005).

[24] M. Meier and A. Wokaun, *Enhanced fields on large metal particles: dynamic depolarization*, Opt. Lett. **8**, 581 (1983).

[25] J. R. Lakowicz, *Principles of Fluorescence Spectroscopy*, Springer, 2006.

[26] K. B. Eisenthal and S. Siegel, *Influence of resonance transfer on luminescence decay*, J. Chem. Phys. **41**, 652 (1964).

[27] T. Förster, *Zwischenmolekulare energiewanderung und fluoreszenz*, Ann. Phys. **437**, 55 (1948).

[28] J. Stehr, J. Crewett, F. Schindler, R. Sperling, G. von Plessen, U. Lemmer, J. M. Lupton, T. A. Klar, J. Feldmann, A. W. Holleitner, M. Forster, and U. Scherf, *A low threshold polymer laser based on metallic nanoparticle gratings*, Adv. Mater. **15**, 1726 (2003).

[29] H. P. Urbach and G. L. J. A. Rikken, *Spontaneous emission from a dielectric slab*, Phys. Rev. A **57**, 3913 (1998).

[30] W. Vos, R. Sprik, A. van Blaaderen, A. Imhof, A. Lagendijk, and G. Wegdam, *Strong effects of photonic band structures on the diffraction ofcolloidal crystals*, Phys. Rev. B **55**, 1903 (1997).

[31] M. Agio and A. Alù, *Optical Antennas*, Cambridge University Press, 2013.

[32] F. J. García de Abajo, *Colloquium: Light scattering by particle and hole arrays*, Rev. Mod. Phys. **79**, 1267 (2007).

[33] M. P. van Exter, V. T. Tenner, F. van Beijnum, M. J. A. de Dood, P. J. van Veldhoven, E. J. Geluk, and G. W. 't Hooft, *Surface plasmon dispersion in metal hole array lasers*, Opt. Express **21**, 27422 (2013).

[34] M. Paulus, P. Cay-Balmaz, and O. Martin, *Accurate and efficient computation of the Green's tensor for stratified media*, Phys. Rev. E **62**, 5797 (2000).

[35] J. Jung, T. Søndergaard, T. G. Pedersen, K. Pedersen, A. N. Larsen, and B. B. Nielsen, *Dyadic green's functions of thin films: Applications within plasmonic solar cells*, Phys. Rev. B **83**, 085419 (2011).

[36] A. B. Evlyukhin, C. Reinhardt, and B. N. Evlyukhin, Egor andChichkov, *Multipole analysis of light scattering by arbitrary-shaped nanoparticleson a plane surface*, J. Opt. Soc. Am. B **30**, 2589 (2013).

[37] A. E. Siegman, *Lasers*, University Science Books, 1986.

[38] M. P. van Exter, V. T. Tenner, F. van Beijnum, M. J. A. de Dood, P. J. van Veldhoven, E. J. Geluk, and G. W. 't Hooft, *Surface plasmon dispersion in metal hole array lasers*, Opt. Express **21**, 27422 (2013).

[39] J. B. Pendry, *Photonic band structures*, J. Mod. Opt. **41**, 209 (1994).

[40] M. M. Sigalas, C. T. Chan, K.-M. Ho, and C. M. Soukoulis, *Metallic photonic band-gap materials*, Phys. Rev. B **52**, 11744 (1995).

[41] C. M. Soukoulis, *Localization of light: Theory of photonic band gap materials*, Kluwer Academic Publisher, 1995.

4

Statistics of randomized plasmonic lattice lasers

We study lasing in randomized lattices of silver particles in a dye doped waveguide. We set out to answer a basic question, triggered by earlier observations of distributed feedback lasing in 2D periodic plasmonic particle lattices: how much order do you need to obtain lasing? We start from a diffractive 2D square lattice of silver nanoparticles with a pitch that satisfies the 2^{nd} order Bragg diffraction condition at the emission wavelength of the dye. By randomly removing particles, and by displacing particles we increase disorder. We observe that lasing at the 2^{nd} order Bragg diffraction condition is very robust, with lasing even persisting when 99% of particles is removed. Above a certain amount of disorder new features appear in the spectrum as well as in the fourier image that are due to random lasing. We classify fourier space output on the basis of structure factor calculations. In addition we apply speckle intensity statistics analysis to real space fluorescence images and introduce a new method to differentiate between spontaneous emission and lasing emission.

4.1 Introduction

In plasmonics the interaction between light and free electrons in metal is used to obtain highly localized electromagnetic fields [1]. Over the past years plasmonics has received widespread interest because of the potential to confine light in sub-diffraction

limited volumes for nanoscopy [2], and optical information processing [3], and to create huge near field enhancement for light-matter interaction [4]. Plasmonic particles not only carry strong near fields, but also scatter light much more strongly than dielectric particles of equal size. Plasmonic particles have been used as nanoscale antennas that provide up to thousand-fold fluorophore emission rate enhancement [5–7], emission directivity [8, 9], and opportunities for surface-enhanced Raman and surface-enhanced infrared spectroscopy [10]. The properties of individual plasmon particles may be enhanced by placing particles in periodic arrays [11], with demonstrated uses in e.g. solar cells and light emitting diodes [12, 13]. In view of the strong field enhancement effects, the interplay of gain with plasmon particles to form lasing systems is of large interest.

There are three different ways of using gain in a plasmonic system. First, propagating surface plasmons may be coupled to a gain medium so that loss compensation may be achieved [14]. Second, stimulated emission may trigger lasing into the surface plasmon or plasmon polariton mode of a single nanoparticle when sufficient feedback is provided by a plasmonic resonator [15, 16]. This is known as SPASER (Surface Plasmon Amplification by stimulated Emission of Radiation) [17]. Third, by embedding plasmonic particle clusters in a gain medium, near field enhancement and multiple scattering can combine to give distributed feedback lasing [18]. Several groups [19–21] showed that periodic lattices of plasmonic scatterers can yield lasing at frequencies determined by the pitch of the array through second order Bragg diffraction, as is also the case in dielectric distributed feedback lasers. Dielectric DFB lasers, whether as semiconductor laser, or as organic DFB laser, are widely applied devices that provide large area, and low-threshold lasing using a low index-contrast periodic grating for feedback by Bragg diffraction, that is embedded in a medium that is at the same time the gain medium and a planar waveguide [22]. In a typical DFB laser, the index contrast is small, so that the waveguide dispersion is folded due to the introduced periodicity, but is otherwise hardly changed in the sense that stop gaps are narrow in spectral bandwidth. Associated to the absence of wide stop gaps is the need for DFB lasers to span large areas to build up feedback. In contrast, in the recently reported plasmon systems a characteristic large stop gap occurs in the hybridized dispersion of waveguide and plasmon lattice, as we discussed in Chapters 2 and 3. This results from the much larger scattering strength of metal particles. Given the unique properties of plasmonic particles in terms of their huge scattering strength compared to dielectric DFB constituents, a question that naturally arises is how robust plasmonic particle array lasers are to disorder. In between the extremes of a nominally perfectly periodic laser and a completely random laser, this question encompasses a large spectrum of "correlated disorder" cases [23–25], in which particles are for instance progressively shuffled compared to ideal positions in a lattice, or where random configurations are made by randomly removing scatterers from a perfect lattice. In this Chapter first we treat the problem from the viewpoint of DFB lasers, in particular unravelling how much disorder a plasmon DFB laser can suffer, and how disorder affects figures of merit like threshold, outcoupling, and angular profile. In the second part of the Chapter we rather view the system from the viewpoint of disorder lasers, in particular applying speckle

statistics analysis. We demonstrate that a plasmonic DFB laser is a useful platform to explore lasing in correlated disorder systems.

4.2 Lasing in disordered samples

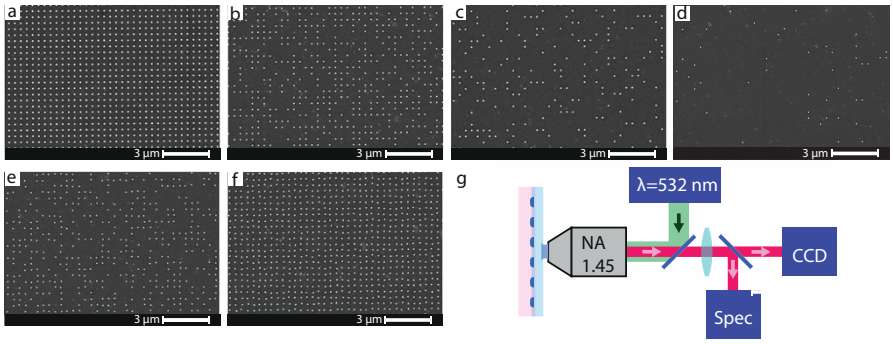

Figure 4.1: SEM images of randomized particle arrays (a-f) and a schematic of the setup (g). The top row (a-d) shows particle arrays in which particles have been randomly removed to leave fill factors of 100%, 50%, 20% and 5%. Panels (e-f) are for fill factor 50% and 100%, with particles randomly placed in a box of 100 nm centered on each perfect-lattice site. Scale bars in all SEM images are 3 μm. The setup diagram (g) highlights that we use a high NA fluorescence microscope with 532 nm pulsed pump laser (0.5 ns), and single shot collection of spectra, or alternatively CCD images in a real-space, or Fourier-space imaging plane.

We fabricate silver particle arrays on glass using the electron beam lithography procedure reported in Chapter 2. The particles are 30 nm high silver particles of radius about 50 nm arranged (in case of a sample without intentional disorder) in a square lattice with an interparticle separation of 380 nm. Subsequently the array is embedded in a SU8 layer (refractive index about 1.65) of 450 nm thick that simultaneously acts as single mode TE waveguide and as gain medium, through incorporation of 0.25 wt% Rhodamine 6G. We start with a perfect periodic lattice which we randomize using two methods. First, we knock out particles randomly from the periodic lattice. The randomness is increased by decreasing the probability to leave a particle in the lattice, where probabilities for each site are drawn independently. For our samples we use a probability P of 100% (periodic lattice), 50%, 20%, 10%, 5%, 2% and 1%. As a second randomization method, we displace each particle by choosing for each a random position in a box of size l centered at their initial lattice position. We choose l to be 0 nm, 20 nm, 40 nm, 60 nm, 80 nm and 100 nm. Finally, we use combinations of all values of P and l. While for each lattice site the probability to keep a particle is drawn independently, we note that strong spatial correlations remain, based on the fact that particles remain situated on (or near, for $l > 0$) the ideal lattice sites. A select subset of disordered particle arrays is shown in figure 5.1a-f that highlights the progression

from perfect to strongly diluted samples, as well as the effect of particle shuffling. In discussing our optical measurement data throughout this Chapter we will limit ourselves to presenting complete data for a select set of samples that highlight the salient features. These are the samples with varying fill factor (presenting P= 100, 50, 5 and 1%) at zero shuffle (l=0), and conversely maximum random particle displacement (l=100 nm) at a fixed fill factor of P=50%.

We use the inverted fluorescence microscope explained in Chapter 2, in which the sample is excited through a high NA objective using a pulsed 532 nm laser. A schematic of the setup is shown in figure 5.1g. The schematic shows the green pump laser, and the excitation and collection paths wich use the same objective. In particular we perform real space and Fourier microscopy in an NA=1.45 (Objective Nikon Plan Apo λ 100×) fluorescence microscope, where sample excitation is realized from the glass side using 0.5 ns pulses in the range of 0–250 nJ (0—10 mJ/cm^2). Figure 4.2(a) shows lasing spectra for a selection of samples with progressively increasing degrees of disorder, starting from the perfect lattice (P=100%, l=0) in Fig. 4.2a that lases at 590 nm, as expected from its second order Bragg condition for the waveguide mode, set by $\lambda = n_{\text{waveguide}} d$, with $d = 380$ nm the pitch, and $n_{\text{waveguide}} \approx 1.55$ the waveguide mode index. The mode index of $n = 1.55$ matches calculations and can be directly read off from Fourier images (see below). As in Chapter 2, the threshold is at around 1 mJ/cm^2. When diluting the lattice, from 100% to 50% and even down to fill factor $P = 5\%$ the lasing condition clearly remains, and in fact the threshold remains approximately constant as compared to the perfect lattice (input-output curves in Fig. 4.2(b)). In absolute terms, the lattices with particles removed actually offer *more* output emission at a given pump power, both for the spontaneous emission background and the lasing peak. This indicates that disorder by moderate removal of particles aids outcoupling, but does not hamper feedback. When fixing the fill factor to P=50% and shuffling the remaining particles by as much as 100 nm, i.e., over 25% of the pitch, lasing remains robust in the sense that a single sharp lasing peak occurs at the second order Bragg condition of the original perfect lattice, albeit that in this case the threshold is about five times higher. Finally, it is particularly surprising that even at a fill factor of 1%, when as many as 99% of the particles have been removed from the lattice, lasing persists at the Bragg condition of the perfect lattice.

The fact that the primary lasing condition remains at the second order Bragg condition does not imply that the lasing characteristics remain unaffected by the disorder. In particular, we observe several distinct phenomena. First, as regards the lasing peak one could expect changes in center wavelength or width. For shuffling of particles we find hardly any variation in lasing peak wavelength, while upon dilution of the lattices, the peak laser wavelength varies by around 2 nm. The width of the lasing peak, as determined from the first spectrum above threshold, is at the spectrometer resolution for all cases. Second, the lasing threshold (plotted in Figure 4.3 gradually increases by up to a factor of 3 as we increase the random displacement l from 0 to 100 nm, at fixed lattice fill factor of 50%. In Figure 4.3 we plot thresholds for several independent experiment runs on different samples with nominally identical parameters, where in each run we normalized thresholds to that of the sample with

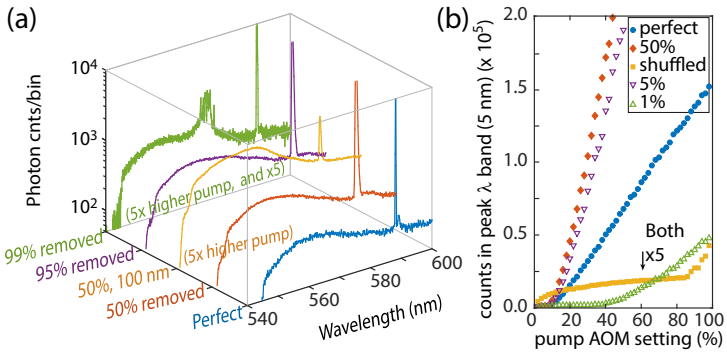

Figure 4.2: (a) Spectra for a nominally perfect sample (100% fill factor, blue curve), 50% diluted sample (red), a 50% diluted sample with 100 nm shuffle (orange), and a sample with 95%, and 99% of particles removed (purple and green, resp.). Spectra are averaged over three shots, and plotted on a log scale. All spectra are taken at 25 nJ pump energy, except for the two cases with a much higher threshold (50% with 100 nm shuffle, and 99% removal, spectra at 240 nJ). For the case where 99% of the particles was removed, the signal is furthermore multiplied by 5 to be visible on the same scale. In (b) we plot output (lasing plus spontaneous emission) in a 5 nm band around the 2nd order Bragg condition as function of input power, as controlled by the AOM where the x-axis represents percentage of maximum excitation power of 250 nJ. Only for the very dilute sample (99%) and the sample with large shuffle do we find a much larger threshold than for the other cases. Note that the perfect sample has a smaller slope above threshold, indicating poorer outcoupling.

50% fill factor and no shuffle (arbitrarily chosen as our reference sample). This normalization procedure reduces variations between samples that are due to difference in polymer thickness or doping that might occur between different sample fabrication runs. That the thresholds are immune to displacement of particles up to between 20 and 40 nm is common among all samples, as is the fact that the threshold rises for higher displacement. For the case of decreasing fill factor P (at no shuffle), the threshold behavior is less intuitive. Thresholds for the lattices with fill factor 100% down to 20% are all comparable. We attribute this remarkable result to the fact that the particles on one hand are required to provide feedback by scattering, yet on the other hand constitute a loss channel through absorption. Since the particles are very strongly scattering compared to those that suffice to achieve lasing in DFB lasers, it is reasonable that removing 50% to 80% of them leaves sufficient feedback by scattering, and in fact may even reduce threshold by reducing absorption. We find a marked increase in threshold only for fill factors below 20%, from which point on we find not only an increase, but also a wide spread in threshold. We attribute the much increased spread in lasing thresholds observed for very low fill factors to a third change in the lasing behavior that is evident from examining the spectra. The spectra themselves at very low fill factor show the appearance of extra emission peaks distinct from the $\lambda = 590$ nm Bragg condition at markedly blue-shifted wavelengths that are much closer to the main emission band of Rh6G (Fig. 4.2(a), green spectrum). We hypothesize that at large fill

factors, above 20%, the randomized lasers essentially remain DFB lasers that function near the original diffraction condition, but with thresholds that increase with increasing particle shuffle. At very low fill factors qualitatively different behavior emerges, where 2D DFB lasing competes with behavior reminiscent of random lasing [26, 27].

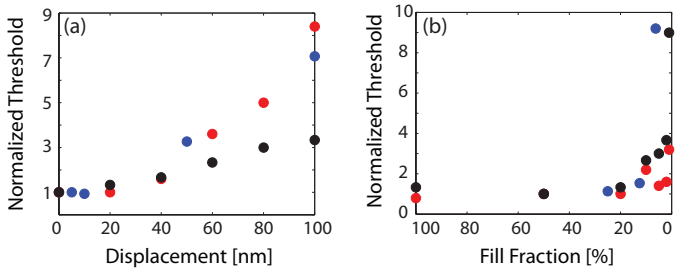

Figure 4.3: Threshold values normalized to the threshold for fill fraction 50% and shuffle 0 nm as a function of shuffle (a) and fill fraction (b). We report three data sets (black, blue red for the three series), taken on different sample substrates. Due to differences in SU8 preparation, absolute thresholds between runs are not comparable, the threshold differences show the same trends from run to run. For increasing shuffle, the lasing threshold steadily rises by at least a factor three. For decreasing fill fraction, we first see no threshold variation, or even a threshold reduction, until very low fill factors < 20% are reached. The spread in threshold is remarkably large for low densities.

To rationalize the fact that lasing persists even at very large levels of disorder, especially in terms of lattice dilution, we consider the structure factors of the various (dis)ordered lattices. The structure factor is defined as the Fourier transform of the lattice of particle center coordinates. Figure 4.4 shows structure factors for the perfect, periodic, lattice as well as a 50% diluted lattice, a 50% diluted lattice with maximum shuffle (100 nm), and a lattice of fill factor 5%. Evidently, when diluting the lattice by 50%, even at maximum particle displacement the structure factor still shows clear Fourier peaks at the ideal-lattice reciprocal lattice vectors. At maximum shuffle, the Fourier peaks reduce moderately in intensity, and a background appears of speckle that is especially evident at larger k. In contrast, at very low fill factor the Fourier peaks are only just evident above the speckled background that is typical for a completely random system. To conclude, by 'merely' reducing the lattice fill factor to 50% or 20%, very strong spatial correlations remain, explaining why the original 2nd order Bragg condition is clearly available for lasing. Likewise, randomizing particle locations by l=100 nm does not strongly reduce the spatial correlations. Only in case of strongly reducing the lattice fill factor, do spatial correlations become faint. Besides an analysis of the structure factor, that only accounts for the particle ordering, lasing naturally also depends on the gain length, and particle scattering strength. The gain length of the Rh6G ($3 \cdot 10^{-20}$ m^2 cross section) doped waveguide layer is estimated as $\approx 4\mu$m, or 10 unit cell spacings, at the maximum pump intensity. Lasing is thus aided by the fact that the 2D planar waveguide geometry strongly favors amplification of in-plane

scattered light, with a short gain length comparable to the interparticle distance. As regards scattering strength, in Chapter 2, it was established for the 'perfect' periodic lattice (no intentional disorder) that the Ag particles are sufficiently strongly scattering to open a clear, 3% wide stop gap at the second order Bragg condition. This is a key number, since the inverse of the relative stop gap width is a direct measure for the Bragg length, i.e., the number of unit cells required for Bragg reflection [28]. In dielectric DFB structures lasing is achieved under conditions where the scattering strength per unit cell is very small, meaning that not just 30 lattice spacings (or scatterers) provide sufficient feedback for lasing, but of order 10^3 are needed [29]. Indeed, as we reported in Chapter 2 the exact same lasing geometry but with Ag replaced by the highest index possible for a dielectric (TiO_2), we could not even obtain lasing given the pump area of about 150 lattice spacings across. With particles twice bigger in volume, we barely obtained sufficient feedback for lasing. This rationalizes that for the plasmonic particles, even at a strong reduction of the scattering strength per unit cell there is sufficient distributed feedback for lasing, whether that reduction is obtained by shrinking particles, or removing them altogether. An interesting question is if upon diluting the lattice, scattering measurements in absence of gain can be used to resolve the width of the bands, and the width of the stop gap. In practice, however, we note that such experiments are hardly feasible. Figure 4.5, further discussed below, shows that the passive-system features that are due to Bagg diffraction vanish in amplitude upon dilution, even though upon amplification they stand out. Given the particle cross section of about $0.07\mu m^2$, expected transmission features have only a few percent amplitude at dilutions to 20% or less. We note that a *full* theory of lasing in these systems is beyond the scope of this thesis. In fact, even for the perfect periodic case, there is currently no theory that covers simultaneously the plasmonic lattice dispersion, gain, and the emergence of lasing from noise [30].

4.3 Fourier space analysis

The structure factor analysis directly motivates a study of Fourier images to further understand the distinct lasing characteristics at various types of disorder. Fourier images, or "back focal plane" images for the perfectly ordered case (P=100% and *l=0*) were discussed in depth in Chapter 2. In brief, they present the following appearance (figure 4.5a) for below-threshold emission. They appear as bright disks on the CCD where the center corresponds to the optical axis, and the distance from the center outwards is proportional to $|k_{||}|/k_0 = n\sin\theta$ (θ the emission angle into glass). Thus the outer edge of the disk corresponds to the NA of the objective, which is equal to 1.45. The inner circle corresponds to an NA of 1 (i.e. $k_{||} = \omega/c$). It is due to the fact that below threshold most emission exits the dye layer at an angle just above the critical angle for the air/glass interface, i.e., at an NA greater than 1, which is a well known property of the emission pattern of dipole emitters held just above a glass interface [31]. In addition to these sharp concentric circles, eight broad, diffuse, circles appear that are not centered at the origin, but rather are centered at the reciprocal lattice

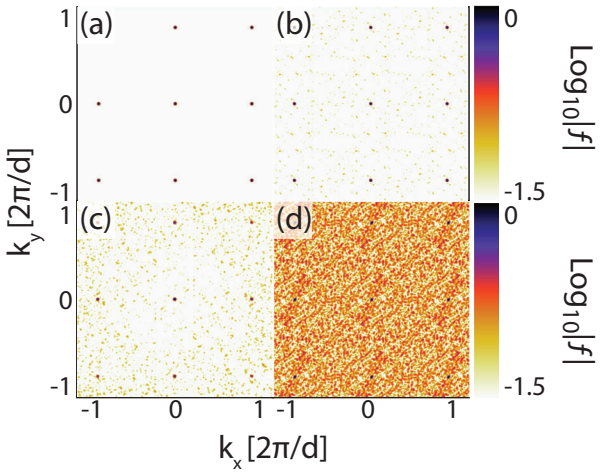

Figure 4.4: Fourier transform of a lattice with fill fraction 100% and shuffle 0 (a), fill fraction 50% and shuffle 0 nm (b), fill fraction 50% and shuffle 100 nm (c), and fill fraction 5% and shuffle 0 nm (d). The color scale is normalized to the FT maximum.

vectors $\mathbf{k}_{||} = 2\pi/d(m,n)$ (with d the particle pitch and m,n integer) and have radius $k_0 \times n_{\text{waveguide}}$. Here $n_{\text{waveguide}}$ is the effective refractive index of the waveguide mode, inbetween the index of glass and the refractive index of the SU8 layer ($n_{SU8} = 1.65$). Thus the waveguide mode index $n_{\text{waveguide}} \approx 1.55$ can be directly read off from the radius of curvature of the observed bands. In solid-state physics terms, these images represent repeated-zone-scheme iso-frequency surfaces of the nearly-free waveguide dispersion relation, blurred by the spectral bandwidth of the dye. Note that these circles appear to touch at $k_{||} = 0$ indicating that the pitch is such that the second order Bragg condition is met for waveguide modes at wavelengths close to the emission band of Rh6G. The below-threshold Bragg diffracted waveguide modes, i.e., the circles, are broad because the fourier images are panchromatic, and different wavelengths yield cirlces centered at somewhat different origins. Strictly, the circles touch in the center for just one emission wavelength, which is equal to the lasing wavelength (590 nm, see Fig.4.2a). When the system reaches the lasing threshold, a central lasing spot emerges at $k_{||} = 0$ (center of the image), as can be seen in all fourier images in Fig. 4.5).

Figure 4.5 shows back focal plane images for disordered samples at pump powers just a few percent above lasing threshold, so that besides the emission at $k_{||}$ from the lasing mode, the wave vector structure for spontaneous emission can still be made out, as can be seen from the circles in Figure 4.5a. Figure 4.5 b, c and d show fourier images for samples in which we reduced the fill factor of the lattice to 20%, 5% and 1%, respectively. Going from 100% to 20% fill factor, two facts stand out. First, the back aperture is now filled with distinct speckle. The emergence of speckle directly points at the spatial and temporal coherence of the lasing mode. We attribute the emergence of speckle to the fact that lasing that in the 100% case only couples out as a $k_{||} = 0$ beam,

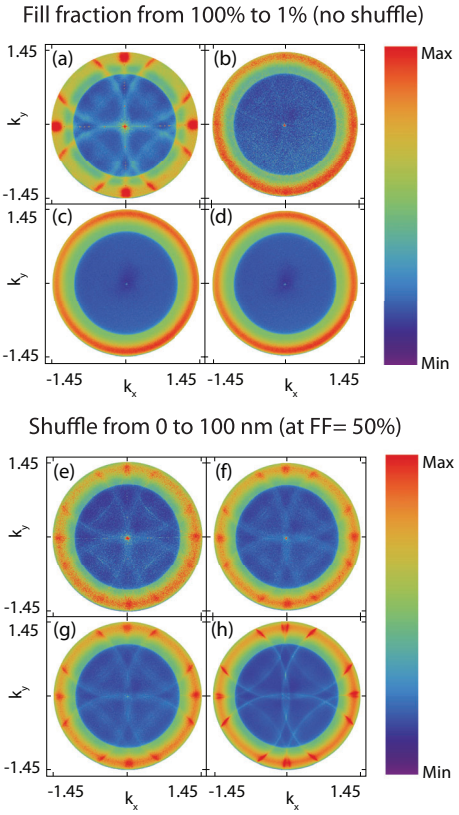

Figure 4.5: Back focal plane images taken at a pump power just a few percent above threshold for plasmon lattice lasers that are randomized by diluting from 100% to 20%, 5% and 1% fill factor (a-d), and by shuffling ((e-h), fixed 50% fill factor) by 0, 40, 60 and 100 nm. The color axes in all cases are chosen to obtain a dynamic range of around 5 spanning *mean*×[0.35 1.8] around the *mean* image intensity. Specifically, for the background subtracted images, the ranges are [min,max]=[154,700], [199,1050,], [212,1144], [264,1503] for (a-d) and [174,946], [204,1095], [282,1525], [402,2257] for (e-h), where numbers correspond to background-subtracted CCD counts (about 3 photoelectrons per count) in single shot images. The horizontal and vertical axes are in units of $k_0 = \omega/c$, i.e., in units of numerical aperture. In all cases the lasing output is visible as an intense spike at $\mathbf{k}_{||} = 0$, as well as to varying degrees as speckle.

can randomly scatter at the introduced disorder, thereby distributing intensity over the back aperture. The second remarkable observation is that, compared to the ordered sample, the repeated circles are only faintly observable. At even lower fill factor the repeated circles completely disappear. This stands in good agreement with the fact that for randomly removing particles, the reciprocal lattice of the lattice in the structure factor rapidly looses contrast. For the strongest dilution the speckle itself reduces in visbility, owing to the fact that the associated increase in threshold causes an increase in broad background emission as consequence of the increased pump intensity.

Fourier images at a fixed, high fill factor of 50%, but increasing degree of disorder introduced by shuffling present a very different evolution of Fourier images. Figure 4.5(e-h) shows fourier images for pump energies just above the lasing threshold for a 50% fill factor at l=0, l=40, l=60, and l=100. At all degrees of shuffle, even as large as 100 nm, the repeated-zone-scheme dispersion relation remains clearly evident as repeated circles. In most instances we in fact see two sets of repeated-zone scheme dispersion. Our interpretation is the following. The "inner" set of circles, which is narrow in width and speckled and that touches at $k_{||} = 0$ corresponds to lasing emission. The fact that scattering of the laser light does not lead to a homogeneous distribution of speckle over the back aperture as in the case of strongly diluted lattices shows that the high fill-factor lattices with displaced particles are disordered yet still strongly correlated. The width of the circles reflects the spectrally narrow lasing line, while the speckled nature shows spatial coherence of the lasing mode. The "outer" set of circles is broader and diffuse. They correspond to incoherent Rh6G emission at shorter wavelength, i.e., at the Rh6G spontaneous emission maximum. These circles become more apparent at higher disorder, as consequence of the much higher threshold pump intensity at which the image needs to be acquired. The experimental observation that whereas the dilute lattices hardly show evidence for the underlying repeated zone scheme dispersion relation, the dense lattices clearly do is easily understood from considering the structure factor of the underlying lattice (Figure 4.4), in which the reciprocal lattice still clearly stands out.

4.4 Real space speckle statistics

So far we have examined the lasers as perturbed versions of the ideal, periodic, plasmonic DFB laser, asking how performance ‘suffers’ upon introducing disorder. From a very different perspective, our plasmonic lasing platform is of a very large current interest in another field of resarch, i.e., lasing in random systems, and in systems with correlated disorder [23–25]. In that field, rather than studying Fourier images for residual diffraction conditions, one rather focuses on the statistical properties of speckle. Above lasing threshold, one expects the emitted light to be spatially coherent across an extended area of the structure. Interference between coherent scattered waves in a random medium will generate a grainy pattern that is known as speckle [32] for which the random scattering community has developed quantitative analysis tools. These analysis tools map intensity distributions, as well as spatial/angular correlations.

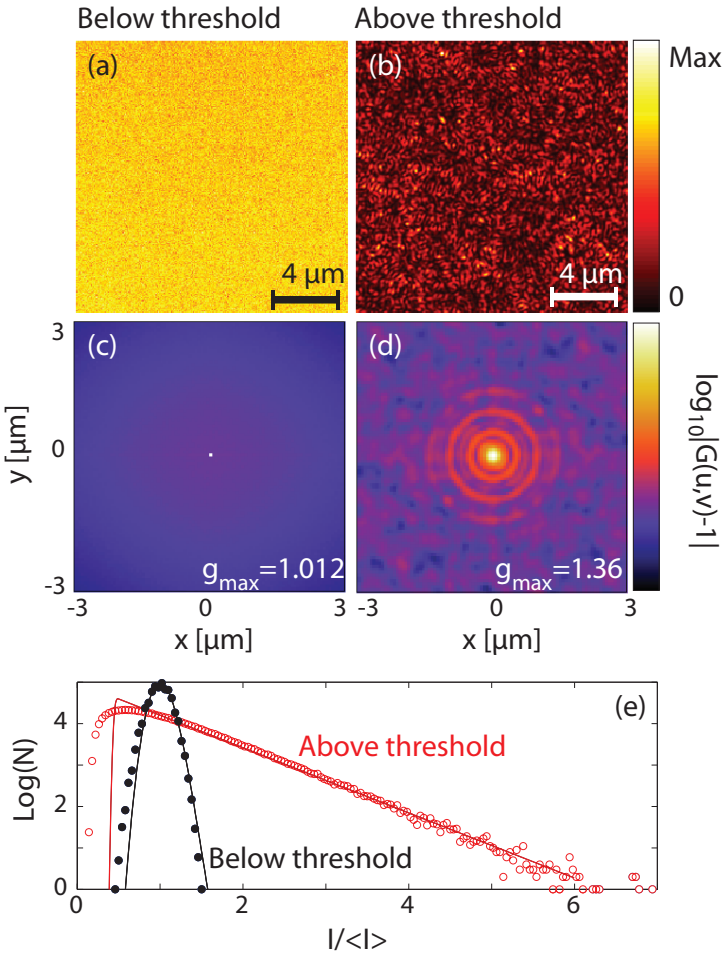

Figure 4.6: Real space fluorescence images below (a) and above (b) threshold for an array with fill factor 50% and no particle shuffling. The pump powers are at about 20 resp 250 nJ for panels (a) and (b), and the color scales span to 180 resp. 10000 counts. Panels (c,d) show the respective autocorrelations, using a colorscale that is linear in $|\log_{10} G(u,v) - 1|$, covering the range for $G(u,v)$ from [1.003,1.012] in (c) and [1.001, 1.36] in (d). The intensity statistics for below threshold data is Poissonian (black dots, distribution with no adjustable parameter), while the above-threshold speckle shows a much longer tail (red dots). Overplotted is the expected statistics for the sum of incoherent Poisson distributed emission (contributing $\alpha = 60\%$ of the intensity and speckle with pure Rayleigh statistics.). The intensity statistics is plotted as function of $I/\langle I\rangle$ using as vertical scale the log of the number of occurrences. The statistics uses $\sum N = 6.1 \cdot 10^4$ image pixels.

In the context of random lasers, for instance, intensity statistics of speckle has been studied as function of pumping strength [26, 27]. While for perfectly uncorrelated disorder, speckle statistics follows robust laws, deviations from these laws are of even larger interest, as they can for instance point at localisation effects, are sensitive probes of otherwise poorly quantifiable scattering correlations, and can be used to quantify rare, but dramatic events in correlated disorder systems [33].

Example real space images below and above threshold for the laser with fill factor P=50% and no further shuffling l=0 nm, are shown in figure 4.6a and b. Below threshold, the emission is essentially constant over the field of view (about 20 microns across, set by the pump spot size) with a small pixel-to-pixel variation that is consistent with Poisson noise. This behavior is commensurate with expected behavior for fluorescence. That the particle lattice, which in principle is resolvable with white light illumination, does not stand out is likely due to the fact that the waveguide height (400 nm) far exceeds the particle height, meaning that most fluorophores do not enjoy a strong local field enhancement. Above threshold the real space fluorescence image is entirely different, with signal variations from position to position comparable in magnitude to the mean intensity itself, as expected for a speckle pattern.

To investigate spatial correlations we show the normalized autocorrelation in figure 4.6c and d. The normalized autocorrelation is given by

$$G(u,v) = \frac{\iint I(x,y) \cdot I(x-u, y-v) dx dy}{(\iint I(x,y) dx dy)^2} \tag{4.1}$$

In this definition complete uncorrelated images yield $G(u,v) = 1$, whereas any spatial correlation will result in $G(u,v) \neq 1$.

Below threshold, the real space images yield a normalized autocorrelation that is flat, and 1, except for a single-pixel wide peak at (0,0). For a fluorescence emission image where each pixel follows an independently drawn Poisson statistics, one indeed expects $G = 1$, except at $(u,v) = (0,0)$ where a small excess correlation is expected for Poisson noise, of $G(0) = 1 + \frac{1}{\langle I \rangle}$ with $\langle I \rangle$ the mean intensity. Thus, the autocorrelation of our below-threshold data is in excellent accord with uncorrelated fluorescence emission from a homogeneous dye film. Above threshold two features change. First, the autocorrelation shows a much higher maximum value of around 1.36 at $(u,v) = (0,0)$, well above $1 + \frac{1}{\langle I \rangle}$. Second, also away from $(u,v) = (0,0)$ there is a clear correlation, with distinct circles appearing around the central peak. For a speckle pattern that results from uncorrelated disorder through superposition of plane waves of random phase and amplitude, one expects the autocorrelation to exhibit a sinc-type oscillatory behavior with a typical width at half maximum equal to the diffraction limit and a maximum of 2, at least for purely random, but fully coherent, speckle [32, 34]. Our data is in good qualitative agreement with this expectation, barring two features. First, we note that the square nature of the underlying lattice is faintly visible in the autocorrelation, directly indicating the correlated nature of the disorder [35]. Second, the autocorrelation contrast of 2 is not reached. We attribute this to the fact that above threshold, images are a summation of incoherent and uncorrelated spontaneous emission that is broadband, plus the speckle pattern resulting from the spectrally narrowband lasing mode (see

Fig. 4.2). Indeed, with increasing pump power above threshold we find increasing autocorrelation contrast (see below). Clearly, the crossing of the laser threshold is dramatically present in the real space autocorrelation images as a transition from completely uncorrelated to showing a distinct spatial autocorrelation commensurate with a speckle pattern.

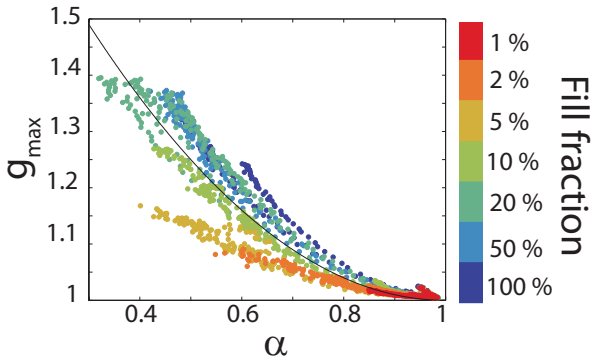

Figure 4.7: Plot of $g_{\max}$, i.e., the maximum value of the real-space autocorrelation, versus α, i.e., the ratio of the incoherent Poisson distributed emission to the total system output, as fitted from the slope of the tail of the intensity statistics. This plots assembles pump-power dependent traces for all values of P and l, where different fill fractions are indicated by the color coding (no coding used for shuffle). The black curve represents the expected universal behavior in equation (4.4). For each sample, as a function of pump power the curve starts near $(g_{\max}, \alpha) = (1.05, 0.95)$ and $\alpha = 0.95$ for lowest pump power, approaching $(1.0, 1.0)$ as pump power is increased, until threshold is exceeded. From that point on, the data points rapidly trace upwards in $g_{\max}$ along the parabola.

Beyond the spatial autocorrelation function, a second tool to analyze speckle is intensity statistics [26, 27, 32, 34]. When speckle is generated as a sum of waves with independently varying amplitudes and randomly distributed phases (uniformly distributed over 2π), the intensity is expected to be distributed according to the so-called Rayleigh distribution [26, 27, 32, 34], given by

$$P_{\text{Rayleigh}}(I;\langle I\rangle) = \frac{1}{\langle I\rangle} e^{\frac{-I}{\langle I\rangle}} \tag{4.2}$$

where $\langle I\rangle$ represents the mean intensity. Speckle generally satisfies the Rayleigh distribution, unless it results from strongly correlated scattering events, and assuming that corrections due to polarization effects can be disregarded. Importantly, the exponential form of the Rayleigh distribution implies that a histogram of $P(I/\langle I\rangle)$ versus $I/\langle I\rangle$ on a semilogarithmic scale simply yields a line of slope -1, independent of the sample, provided that the scattering events randomize phase. Below lasing threshold, we would expect a markedly different intensity statistics, since when fluorophores emit photons incoherently the intensity will simply follow a Poissonian intensity distribution

$$P_{\text{Poisson}}(I;\langle I\rangle) = \frac{\langle I\rangle^I}{I!} e^{-\langle I\rangle}. \tag{4.3}$$

Figure 4.6(e) shows intensity histograms for the below and above threshold image of 4.6(a,b). The below-threshold intensity histogram generated from figure 4.6a is sharply peaked around the mean per-pixel count. It is excellently described by the Poisson distribution, without any adjustable parameter. In stark contrast, the intensity histogram for the above-threshold dataset of Figure 4.6b is not sharply peaked but shows a long, linear tail that is indicative of an exponential dependence as expected for Rayleigh statistics. However, the exponent is not equal to -1. As explanation, we note that just above threshold one expects the collected emission to be the sum of incoherent spontaneous emission plus the speckle pattern generated by the lasing mode, with a ratio between the two that changes as one further exceeds threshold. To benchmark this assertion, we compare the data to the joint probability distribution for the sum of an independently drawn Poisson process, and Rayleigh statistics

$$P_{\text{joint}}(I;\langle I\rangle,\alpha) = \int_0^I P_{\text{Poisson}}(I_1;\alpha\langle I\rangle)P_{\text{Rayleigh}}(I-I_1;(1-\alpha)\langle I\rangle)dI_1$$
$$\approx e^{-I/[\langle I\rangle(1-\alpha)]}\cdot\frac{e^{\alpha/(1-\alpha)}}{2(1-\alpha)}\left\{\text{erf}\left[\sqrt{\frac{\alpha\langle I\rangle}{2}}\right]-\text{erf}\left[\sqrt{\frac{\alpha\langle I\rangle}{2}}(1-I/\sqrt{\alpha\langle I\rangle})\right]\right\}$$

Here the only free parameter is the ratio $0 \le \alpha \le 1$ defined as the fraction of signal contributed by the Poisson background. The approximate expression results from applying a Gaussian approximation to the Poisson distribution and requires $\alpha\langle I\rangle \gtrsim 50$ counts, and reasonably large argument I (rule of thumb $I > \langle I\rangle$). It shows that the large intensity tail is again exponential, but with exponent steepened by a factor $(1-\alpha)$. Therefore, to compare the joint probability function, we fit to the slope of the high-intensity tail. Indeed, now we obtain a good match to the data, again containing no vertical scaling whatsoever. For the example dataset, in Figure 4.6(d), the fit indicates that $\alpha = 0.6$, meaning that 60% of the total intensity is contributed by incoherent emission, and 40% by lasing. As the pump power increases from 25 nJ to 250 nJ, the value of α decreases from 0.96 to 0.6.

To summarize our results from analyzing real space images for a particular randomized laser, the above threshold emission shows an autocorrelation commensurate with that expected for random speckle, with a contrast at $(0,0)$ that rises from 1 (incoherent background) yet remains well below 2 (expected for just speckle). We attribute this to the fact that emission is a sum of incoherent (fractional contribution α) and coherent emission. This same hypothesis also is consistent with the intensity statistics, from which we fit α. We now proceed to show that the normalized autocorrelation contrast at $(0,0)$ and the intensity ratio α are directly related. One can easily derive the expected autocorrelation for a 2D dataset that is the sum of coherent and incoherent radiation in terms of the autocorrelations of each constituent. Supposing once again a mean intensity $\langle I\rangle$ of which a fraction α is contributed by uncorrelated Poisson distributed emission, and a fraction $1-\alpha$ from pure speckle (autocorrelation 2), one expects

$$g_{\max} = 1 + (1-\alpha)^2 + \frac{\alpha}{<I>} \tag{4.4}$$

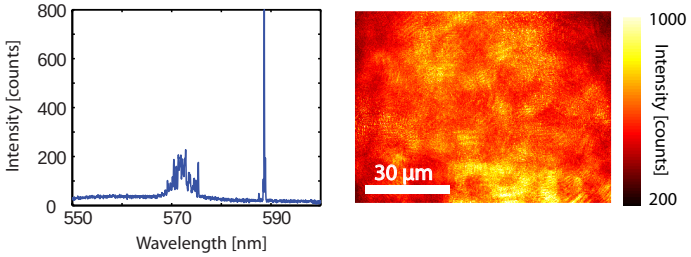

Figure 4.8: Spectrum and real space image above threshold, for a plasmon array laser with fill fraction of just 1%, and shuffle 100 nm. The spectrum clearly shows lasing at the 2nd order Bragg condition of the perfect lattice, near 590 nm. In addition, the spectrum shows many random sharp peaks, clustered around a wavelength of 570 nm. This band coincides with the gain maximum. These peaks do not occur for dense arrays and are attributed to random lasing (out)competing DFB lasing. The real space image shows another distinct feature of diluted systems. Instead of exhibiting a uniform speckle pattern, clusters of speckle appear, on top of a diffuse background.

where $g_{\max}$ is the value of the normalized autocorrelation at $(u, v) = 0$. Typically one can neglect the $\alpha/\langle I\rangle$ term, and the normalized maximum autocorrelation relates to $1-\alpha$ as $g_{\max} = 1 + (1-\alpha)^2$. Figure 4.7 shows $g_{\max}$ as a function of α for all values of P and I and for all 50 pump powers between 0 and 250 nJ. Each dataset traces out the following dependence as function of pump power. Below threshold, we find $g_{\max}$ starting at around 1.05 ($g_{\max} = 1 + 1/\langle I\rangle$, with 20 counts per pixel in our lowest pump power images), and closing in on $g_{\max} = 1$ as pump power is increased towards threshold. At this stage, α is essentially 1 througout. As soon as threshold is crossed, the data trace out the parabolic dependence $g_{\max} = 1 + (1-\alpha)^2$, meaning that simultaneously α decreases well below 1 and $g_{\max}$ increases well above 1.

To first order, we indeed find that all datasets cluster around the predicted parabola of Eq. (4.4, black curve). Closer inspection of Fig. 4.7 surprisingly shows systematic deviations from this picture. In particular, the randomized plasmonic lattices with high fill factor show spatial correlations (g_{max} above the parabola) that exceed the expectation derived from intensity statistics, while conversely for the randomized plasmonic lattices with low fill factors, below 5%, the data remain significantly below the parabola. The latter indicates that the intensity statistics is more wildly fluctuating (α further from 1) then the spatial autocorrelation predicts. We propose that the fact that there is a systematic deviation from the expectations derived for purely uncorrelated disorder is an important starting point for future investigations: it shows that 2D random plasmon arrays are an exciting platform to study lasing in correlated disorder systems. For instance, for the very dilute systems, we hypothesize that we enter the regime where our field of view can contain several uncoupled and spatially separated random lasing modes simultaneously. To support this notion, in figure 4.8 real space images and spectra for this particular subset of dilute samples are shown. The above threshold

spectrum for fill fraction 1% and shuffle 0 nm is significantly different from that in dense arrays, with the appearance of multiple narrow, apparently randomly located peaks in a band around $\lambda = 570$ nm. The above threshold real space image exhibits clusters of speckle on a diffuse background, instead of uniform speckle. This supports the notion that this sample supports isolated lasing at spatially separated clusters of particles. We envision that similar analysis can be applied to a plethora of other designer disorder structures, random lasers and Anderson localization systems, to resolve what are the lowest-loss modes.

4.5 Outlook

To conclude, in this Chapter we have shown that plasmonic DFB lasers are remarkably robust to the introduction of positional disorder, as well as to random removal of particles from the lattice. In fact, even upon removal of as many as 99% of the particles from a periodic lattice, a lasing peak centered on a original Bragg peak of the lattice remains. We attribute the remarkable resilience of lasing in this system to two characteristics of our geometry. On one hand, the basic geometry of a 2D waveguide with high gain favors lasing strongly, owing to the fact that the confinement along one direction creates a strong tendency for in-plane amplification of spontaneous emission (ASE) [22]. We estimate a gain length of just 10 to 15 lattice periods. The second unique characteristic is that plasmonic particles are exceptionally strongly scattering. As we found in our analysis of the purely periodic lattice, the plasmon particles scatter over twenty times more strongly than dielectric particles of comparable size. As size estimate, the inverse of the relative width of the band structure stop gap (3%) of the periodic system provides as estimate that Bragg diffraction requires a distance of just 15 microns (30 unit cells). Hence it is understandable that 'moderate dilutions', meaning removal of 50% to 80% of the particles leaves sufficient feedback by scattering, yet without any penalty in threshold. One could argue that removing particles may even *lower* the threshold owing to the fact that it reduces the likelihood of Ohmic damping. An interesting future experiment is to understand precisely what the optimum filling fraction for lowest lasing threshold is, in dependence of particle scattering and absorption cross sections. In addition, an exciting outlook of this work is that, besides obvious interest for applications of disorder-immune lasing behavior, the geometry of a planar organic waveguiding system with metal particle lattices or oligomers is very amenable to studies of lasing in correlated disordered systems [24, 25]. The plasmon particle arrays are very easy to make by lithography, and are embedded in an easily fabricated gain medium that allows for simple room temperature experiments. Thus they could enable studies of lasing in random 2D systems, and systems with correlated disorder that are now performed using perforated III-V semiconductor membranes [25]. Using the techniques of organic electronics, one could furthermore envision scenarios in which electrically driven operation is possible.

References

[1] S. A. Maier, *Plasmonics: Fundamentals and Applications*, Springer, 2007.

[2] T. H. Taminiau, R. J. Moerland, F. B. Segerink, L. Kuipers, and N. F. van Hulst, $\lambda/4$ *resonance of an optical monopole antenna probed by single molecule fluorescence*, Nano Lett. **7**, 28 (2007).

[3] Z. Han and S. I. Bozhevolnyi, *Radiation guiding with plasmon polaritons*, Rep. Prog. Phys. **76**, 016402 (2013).

[4] M. Agio and A. Alù, *Optical Antennas*, Cambridge University Press, 2013.

[5] A. Kinkhabwala, Z. Yu, S. Fan, Y. Avlasevich, K. Muellen, and W. E. Moerner, *Large single-molecule fluorescence enhancements produced by a bowtie nanoantenna*, Nat. Photonics **3**, 654 (2009).

[6] D. Punj, M. Mivelle, S. B. Moparthi, T. S. van Zanten, H. Rigneault, N. F. van Hulst, M. F. García-Parajo, and J. Wenger, *A plasmonic 'antenna-in-box' platform for enhanced single-molecule analysis at micromolar concentrations*, Nat. Nanotechnol. **8**, 512 (2013).

[7] G. M. Akselrod, C. Argyropoulos, T. B. Hoang, C. Cirac, C. Fang, J. Huang, D. R. Smith, and M. H. Mikkelsen, *Probing the mechanisms of large Purcell enhancement in plasmonic nanoantennas*, Nat. Photonics **8**, 835 (2014).

[8] C. Belacel, B. Habert, F. Bigourdan, F. Marquier, J.-P. Hugonin, S. Michaelis de Vasconcellos, X. Lafosse, L. Coolen, C. Schwob, C. Javaux, B. Dubertret, J.-J. Greffet, P. Senellart, and A. Maitre, *Controlling spontaneous emission with plasmonic optical patch antennas*, Nano Lett. **13**, 1516 (2013).

[9] L. Langguth, D. Punj, J. Wenger, and A. F. Koenderink, *Plasmonic band structure controls single-molecule fluorescence*, ACS Nano **7**, 8840 (2013).

[10] F. Le, D. W. Brandl, Y. A. Urzhumov, H. Wang, J. Kundu, N. J. Halas, J. Aizpurua, and P. Nordlander, *Metallic nanoparticle arrays: A common substrate for both -enhanced Raman scattering and -enhanced infrared absorption*, ACS Nano **2**, 707 (2008).

[11] L. Zhao, K. L. Kelly, and G. C. Schatz, *The extinction spectra of silver nanoparticle arrays: Influence of array structure on plasmon resonance wavelength and width*, J. Phys. Chem. B **107**, 7343 (2003).

[12] S. Mokkapati and K. R. Catchpole, *Nanophotonic light trapping in solar cells*, J. Appl. Phys. **112**, 101101 (2012).

[13] G. Lozano, D. J. Louwers, S. R. K. Rodriguez, S. Murai, O. T. A. Jansen, M. A. Verschuuren, and J. Gómez Rivas, *Plasmonics for solid-state lighting: enhanced excitation and directional emission of highly efficient light sources*, Light. Sci. Appl. **2**, e66 (2013).

[14] P. Berini and I. De Leon, *Surface plasmon-polariton amplifiers and lasers*, Nat. Photonics **6**, 16 (2012).

[15] R. F. Oulton, V. J. Sorger, T. Zentgraf, R.-M. Ma, C. Gladden, L. Dai, G. Bartal, and X. Zhang, *Plasmon lasers at deep subwavelength scale*, Nature **461**, 629 (2009).

[16] R.-M. Ma, R. F. Oulton, V. J. Sorger, G. Bartal, and X. Zhang, *Room-temperature sub-diffraction-limited plasmon laser by total internal reflection*, Nat. Mater. **10**, 110 (2011).

[17] D. J. Bergman and M. I. Stockman, *Surface plasmon amplification by stimulated emission of radiation: Quantum generation of coherent plasmons in nanosystems*, Phys. Rev. Lett **90**, 027402 (2003).

[18] J. Stehr, J. Crewett, F. Schindler, R. Sperling, G. von Plessen, U. Lemmer, J. M. Lupton, T. A. Klar, J. Feldmann, A. W. Holleitner, M. Forster, and U. Scherf, *A low threshold polymer laser based on metallic nanoparticle gratings*, Adv. Mater. **15**, 1726 (2003).

[19] J. Y. Suh, C. H. Kim, W. Zhou, M. D. Huntington, D. T. Co, M. R. Wasielewski, and T. W. Odom, *Plasmonic bowtie nanolaser arrays*, Nano Lett. **12**, 5769 (2012).

[20] W. Zhou, M. Dridi, J. Y. Suh, C. H. Kim, D. T. Co, M. R. Wasielewski, G. C. Schatz, and T. W. Odom, *Lasing action in strongly coupled plasmonic nanocavity arrays*, Nat. Nanotechnol. **8**, 506 (2013).

[21] A. H. Schokker and A. F. Koenderink, *Lasing at the band edges of plasmonic lattices*, Phys. Rev. B **90**, 155452 (2014).

[22] I. D. W. Samuel and G. A. Turnbull, *Organic semiconductor lasers*, Chem. Rev. **107**, 1272 (2007).

[23] F. Riboli, N. Caselli, S. Vignolini, F. Intonti, K. Vynck, P. Barthelemy, A. Gerardino, L. Balet, L. H. Li, A. Fiore, M. Gurioli, and D. S. Wiersma, *Engineering of light confinement in strongly scattering disordered media*, Nat. Mater. **13**, 720 (2014).

[24] G. M. Conley, M. Burresi, F. Pratesi, K. Vynck, and D. S. Wiersma, *Light transport and localization in two-dimensional correlated disorder*, Phys. Rev. Lett. **112**, 143901 (2014).

[25] P. D. García, S. Stobbe, I. Söllner, and P. Lodahl, *Nonuniversal intensity correlations in a two-dimensional Anderson-localizing random medium*, Phys. Rev. Lett. **109**, 253902 (2012).

[26] H. Cao, Y. Ling, J. Xu, C. Cao, and P. Kumar, *Photon statistics of random lasers with resonant feedback*, Phys. Rev. Lett. **86**, 4524 (2001).

[27] G. van Soest, F. J. Poelwijk, and A. Lagendijk, *Speckle experiments in random lasers*, Phys. Rev. E **65**, 046603 (2002).

[28] C. M. Soukoulis, *Photonic Crystals and Light Localization in the 21st Century (p. 194)*, Kluwer, Dordrecht, 2001.

[29] S. Riechel, C. Kallinger, U. Lemmer, J. Feldmann, A. Gombert, V. Wittwer, and U. Scherf, *A nearly diffraction limited surface emitting conjugated polymer laser utilizing a two-dimensional photonic band structure*, Appl. Phys. Lett. **77**, 2310 (2000).

[30] J. Cuerda, F. Rüting, F. J. García-Vidal, and J. Bravo-Abad, *Theory of lasing action in plasmonic crystals*, Phys. Rev. B **91**, 041118 (2015).

[31] L. Novotny and B. Hecht, *Principles of Nano-Optics*, Cambridge University Press, 2007.

[32] J. C. Dainty, The statistics of speckle. In *Progress in Optics* ; Ed. E. M. Wolf, North-Holland, Amsterdam, 1976.

[33] C. Liu, R. van der Wel, N. Rotenberg, L. Kuipers, T. Krauss, A. Di Falco, and A. Fratalocchi, *Triggering extreme events at the nanoscale in photonic seas*, Nature Phys. **11**, 358 (2015).

[34] A. Genack, Fluctuations, Correlation and Average Transport of Electromagnetic Radiation in Random Media. In *Scattering and Localization of Waves in Random Media*; P. Sheng, Ed., World Scientific, Singapore, 1990.

[35] J. J. Greffet and R. Carminati, *Relationship between the near-field speckle pattern and the statistical properties of a surface*, Ultramicroscopy **61**, 43 (1995).

5

Lasing in aperiodic systems

In this Chapter we demonstrate lasing in a suite of quasiperiodic and aperiodic 2D lattices of silver particles in a dye doped waveguide. In particular, starting from a square lattice of plasmon particles we use deterministic generation sequences to generate Galois, Thue-Morse, Fibonacci, Paperfolding, Rudin-Shapiro lattices that have a Fourier spectrum that goes from discrete to increasingly continuous. We show that if the original lattice has a periodicity that allows 2nd order Bragg diffraction in the gain window, the lasing frequency in all structures determined by the second order diffraction condition. However, the outcoupling of laser emission is altered distinctly as compared to square periodic particle arrays, as demonstrated by above threshold fourier images. For different underlying lattice pitches, we also identify lasing on basis of Bragg conditions specific for quasi-periodic lattices that do not occur for periodic square arrays. We also discuss spatial auto-correlations in the real-space output, showing distinct differences from random speckle.

5.1 Introduction

Enhancing light matter interactions is a much studied subject that has both scientific and technological interest. Plasmonics is a promising route to enhance light matter interaction based on strong coupling of light to resonant electron density oscillations in nobel metals [1]. Metallic particles have been shown to exhibit strong scattering, near

field enhancement, and tight light field confinement that has been used for enhancing spectroscopy [2], lighting applications [3], sensors [4, 5], and photovoltaic structures [6, 7]. Moreover, when plasmonic nanoparticles are placed in periodic arrays even stronger interactions can occur due to the coupling of individual particle resonances to the diffraction modes of the lattice, creating a sharp and low loss lattice resonance [8–10].

This type of diffractive plasmon resonance has been employed by several workers to realize plasmonic distributed feedback (DFB) lasers [11–13]. It has been shown that the strong scattering strength of plasmonic particles gives rise to strong feedback in this scattering type laser, much stronger than in conventional dielectric DFB lasers that typically utilize small index-contrast periodic gratings. A DFB laser is a type of scattering laser in which mirrors are replaced by an array of scatterers in which the interparticle distance is chosen such that a second order Bragg diffraction condition is satisfied for frequencies within the bandwidth of the gain medium. Another type of scattering laser has no fixed interparticle distance but a random configuration of particles. In such "random lasers" multiple scattering can result in an effective feedback cavity sufficient for lasing [14–17]. In contrast to the second order DFB laser a random laser results in non-directional and multifrequency laser emission.

In this Chapter we study an intermediate case between periodic and random systems consisting of aperiodic arrays [18–27]. Unlike random arrays, aperiodic systems can be generated according to a deterministic generation sequence. In addition, unlike periodic structures, aperiodic structures are not translationally invariant [28]. A classification scheme to organize the geometry of aperiodic systems can be made by looking at the fourier transform of the structure [25]. The fourier transform of a periodic structure exhibits infinitely sharp Bragg peaks, whereas the fourier transform of an infinite and completely random system is flat. Aperiodic systems can have a fourier transform comparable to these extremes or anywhere in between. For instance, quasiperiodic structures are a particular subset of aperiodic systems and characterized by being more periodic than random [25], while the Rudin-Shapiro structure is generally considered to be close to random. In this work we study lasing in a suite of systems that span the entire scale from periodic to random.

Although quasi/aperiodicity was introduced as a purely mathematical discovery, a link was made with physics when it was shown that certain metallic alloys have a quasiperiodic ordering [29]. Quasiperiodicity has since then become hugely important in crystallography and proven to be such a breakthrough in solid state physics that in 2011 the Nobelprize in Chemistry was awarded to Levine and Steinhardt. Also in optics, the photonic properties of aperiodic arrays have been subject of studies for the past decades [22, 26, 30, 31], especially in framework of 1D and 2D photonic crystals, and in case of plasmonics also in form of 2D particle lattices. In the context of plasmonics, there are two main reasons for which aperiodic systems have received interest. First, numerical studies [32] have claimed that aperiodic plasmonic particle arrays give rise to an intensity enhancement as large as 10^{12} due to large fluctuations of the local fields. Second, as opposed to periodic arrays, aperiodic systems exhibit a broadband optical response [19]. These properties could make aperiodic systems applicable in many

areas such as biosensors [23] and engineered SERS substrates. Demonstrations of this have been given by Lee et al. [33] who used aperiodic metal particle arrays for optical refractive index sensing in a microfluidics device and for sensing a protein monolayer [34]. Another application of quasiperiodic systems is in LEDs where quasiperiodicity can result in more efficient light exctraction [35] because quasiperiodic systems exhibit isotropic photonic bandgap and scattering of light. According to Dal Negro [25], both the broadband response and the field enhancement effects are related to the type of modes that are predicted to occur in aperiodic systems. Aperiodic arrays, are believed to give rise to *critically localized* modes that are characterized by multifractal spatial patterns, large fluctuations of the local density of states and high near field enhancement [36]. These modes are distinct from the infinitely spatially extended Bloch modes of periodic systems, and the exponentially localized modes of random media (assuming Anderson localization is achieved [37]).

When viewing plasmon particle arrays as a research platform for scattering lasers, aperiodic systems offer a way to get controlled randomness or aperiodicity in the multiple scattering, making it possible to study lasing behaviour as a function of order parameters such as spectral flatness. Studies on lasing action in aperiodic systems so far have demonstrated effects such as ten-fold symmetric lasing spot patterns in quasi-periodic photonic crystal lasers [38], reproducibility and robustness of the lasing mode against structural fluctuations [39], multicolour operation [40] and a claimed reduction in lasing threshold [41]. To our knowledge, these demonstrations have all relied on dielectric structures. In particular, in those demonstrations that used 2D systems, workers used high-index slabs with aperiodic arrangements of weakly scattering air holes. In this chapter we study 2D plasmonic aperiodic lasers consisting of strongly scattering particles. In the next section, the experimental setup and measuring procedure is shown, as well as the definition of 7 different lattices that span the scale from periodic to random. We discuss lasing spectra, Fourier-space and real-space output both for the case where the underlying square lattice does and does not support Bragg conditions. Finally we summarize our results and give an outlook.

5.2 Aperiodic plasmonic lattice structures

We fabricate silver particle arrays on cover glass using electron beam lithography, thermal evaporation, and lift off, following the procedure described in Chapter 2. The silver particles have a diameter of 100 nm and a height of 30 nm. We use a thin chromium adhesion layer. We create aperiodic lattices by starting with a square grid of particle positions, and removing particles according to given generation sequences for the Galois, Thue-Morse, Fibonacci, Paperfolding, and Rudin-Shapiro lattice. In the appendix a summary of the generation sequences we use can be found. Using this method for creating aperiodicity a regular 2D lattice underlies the aperiodic pattern, which defines a starting pitch that is the minimum distance between particles. We fabricated three samples: one for which the underlying 2D lattice has a pitch of 380 nm, one with an underlying particle pitch of 300 nm, and one with a pitch of 190 nm.

According to Bragg's law, for a particle pitch of 380 (190) nm, the second (first) order Bragg diffraction condition occurs within the bandwidth of the fluorescence emission of the dye (Rh6G) we use, whereas for a pitch of 300 nm this is not the case. In this Chapter we report on 7 different lattice types organized in the sequence periodic, Galois, Fibonacci, Paperfolding, Thue-Morse, Rudin-Shapiro and random. We define random here by using a square grid as a starting point and randomly removing 50 % of the particles. In figure 5.1a, b, c, d, e, k and l we show SEM pictures of all lattices for a pitch of 380 nm. This ordering sequence for organizing results is on basis of a mathematical measure called "spectral flatness" given by

$$SF = \frac{\sqrt[NM]{\prod_{n,m}^{N,M} |DFT\{s(n,m)\}|}}{\frac{1}{NM}\sum_{n,m}^{N,M} |DFT\{s(n,m)\}|}. \tag{5.1}$$

Input for this quantity is the digitized structure, essentially a matrix of 0's and 1's representing absence and presence of particles on a site (m,n). The denominator is the arithmetic mean of the discrete Fourier transform $DFT\{s(n,m)\}$ of the digitized structure, while the numerator represents the geometric mean. For a periodic structure the spectral flatness equals 0, while for a random structure, the spectral flatness tends to 1, for infinite systems.

Figure 5.1a-g shows SEM images of the various lattices we fabricated (sample pitch 380 nm), while Figure 5.1h-n shows Fourier transforms (absolute value of DFT, or "structure factors") for all lattices. Note that these Fourier transforms have not been obtained from the SEM images, but from finite truncation (250 periods across, similar to size of experimentally studied fields) of the mathematically generated lattices, where we have used Gaussian apodization to reduce truncation artefacts. For the periodic lattice the DFT necessarily corresponds to the reciprocal lattice, i.e., isolated δ-spikes in a square grid of spacing $2\pi/d$. For the Galois, Thue-Morse and Fibonacci lattice, evidently many additional, largely discrete features appear, which is why these structures, that are not translationally invariant, are considered "quasi-periodic". On the other hand, the Rudin-Shapiro lattice has an almost densely filled Brillouin zone, and a spectral flatness that is close to that of the randomized lattice. It should be noted that in the random system, while the Brillouin zone is essentially uniformly filled, the diffraction features at $2\pi/d$ still stand out. This is due to the fact that randomization by particle removal from a random lattice still leaves spatial correlations. Table 5.1 lists spectral flatness calculated numerically from the DFT's, showing an increase from low to high value, as lattices vary from periodic to random. Note that neither the extremum 0, nor the extremum 1 are obtained for the periodic resp. random lattice, a fact which we attribute to the finite truncation and apodization in real space, and correspondingly chosen finite discretization in k-space, used to generate and sample the DFTs. Empirically, we note that convergence of spectral flatness with structure truncation is slow. As this equally affects the experiment and the mathematical analysis, we have chosen to present values appropriate for the experimentally truncated samples.

After fabricating the particle arrays we spincoat a layer of dye doped SU8 2005 (0.25 wt %), which has a refractive index of 1.6 (Chapter 3) and a thickness of 450 nm.

The thickness of the SU8 is chosen such that the SU8 layer acts as a waveguide that supports one TE and one TM mode. The thickness is a trade off between requiring single mode waveguiding on one hand, and good field confinement in the gain medium on the other hand.

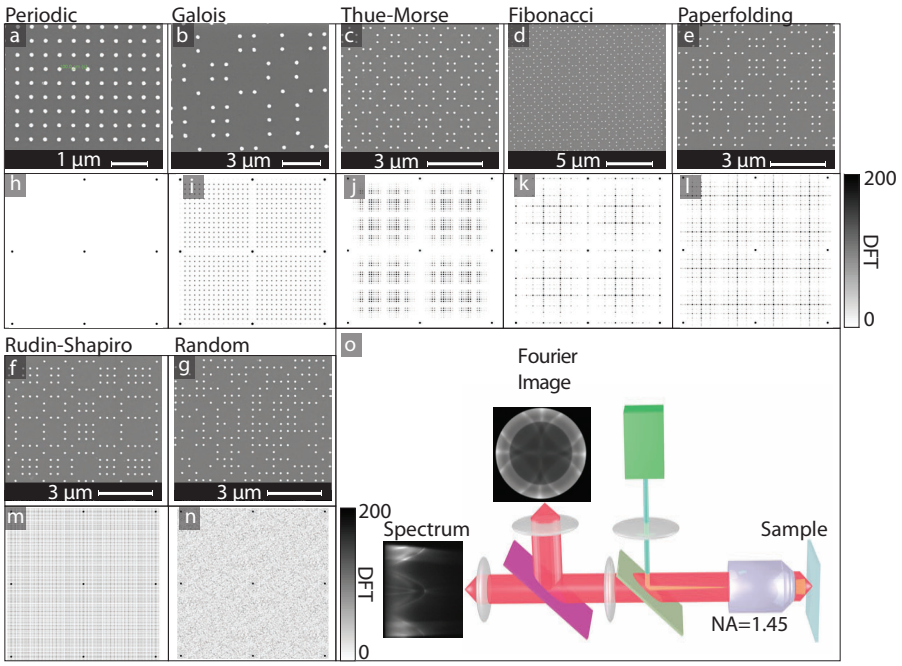

Figure 5.1: Figure a-g shows SEM images of the various lattices we fabricated (sample pitch 380 nm) together with the fourier transform of the corresponding array (h-n). The fourier transform is calculated for a finite grid with values 0 (corresponding to absence of a particle) and 1 (corresponding to presence of a particle). In figure (0) a schematic of the setup is shown, depicting the path of excitation (green light) and of fluorescence (red beam). Both excitation and fluorescence collection is done from the glass side of the sample. With an extra flip lens (between the green and purple mirrors) we can do fourier imaging and spectrally resolved fourier imaging.

5.3 Lasing of aperiodic systems

We use an inverted fluorescence microscope in which the sample is excited from the glass side with a green (532 nm) laser that provides sub-nanosecond pulses in the sub-μJ range. In figure 5.1o a sketch of the inverted fluorescence microscopy imaging setup is shown. We pump a spot of about 50 μm across. Emission is collected from the same side with an NA=1.45 objective and imaged onto a Andor CLARA CCD or the slit of a Shamrock spectrometer coupled to a Si CCD detector. For a sequence of

Structure	Spectral Flatness	Threshold [μ J]
Periodic	0.005	12.5
Galois	0.04	13.5
Thue-Morse	0.13	15.6
Fibonacci	0.17	14.6
Paperfolding	0.35	12.5
Rudin-Shapiro	0.81	15.6
Random	0.84	18.7

Table 5.1: Table with calculated spectral flatness as function of structure type, as well as threshold pump power required to obtain lasing for the case of pitch 380 nm.

50 pump powers we collect single-shot spectra, fourier space images and real space images. In figure 5.2a emission spectra above the lasing threshold are shown for the seven structures, all at underlying pitch of 380 nm. These spectra have been taken only just above lasing threshold, and therefore show both the characteristic broad spontaneous emission spectrum of Rh6G, peaking around 550 nm, and a sharp lasing line. It can be seen that all arrays have a lasing wavelength of approximately 591 nm. This wavelength corresponds to the wavelength for which the second order Bragg diffraction condition holds for a pitch of 380 nm, meaning that $d = \lambda / n_{WG}$, where d is the lattice pitch, λ the vacuum lasing wavelength, and n_{WG} the waveguide mode index. This result is consistent with our earlier studies on periodic arrays, and randomized periodic arrays in which we randomly removed particles to obtain site occupation numbers as low as 1%, that all show that the original periodic-lattice lasing condition is robust against particle removal. Physically this can be understood by noting that the Fourier transform in all cases shows strong peaks at the original reciprocal lattice vectors.

In figure 5.2b threshold curves for all arrays are shown, obtained by plotting the emission intensity a bandwidth of 0.34 nm around the lasing peak. The input-output curves demonstrate a clear kink in the slope corresponding to the lasing threshold. Thresholds (see Table 5.1) vary by about a factor 1.5, while slope efficiencies vary by about a factor two. The lowest threshold is obtained in the periodic case. This result indicates that removing particles aids outcoupling of emission, as was also seen for randomized structures in our earlier work. Quasiperiodic arrays appear to have similar thresholds as the periodic lattice,while the more "spectrally flat" structure (Rudin-Shapiro, Randomized) have higher threshold.

5.4 Lasing output in fourier space

In terms of spectra and input-output curves, the quasi/aperiodicity appears to have no, or only a weak, effect on lasing. However, fourier images, i.e., parallel wave vector resolved images, above lasing threshold clearly reflect the quasi-/aperiodicity as can be seen in figure 5.3. Fourier imaging is obtained by flipping an extra lens into the optical

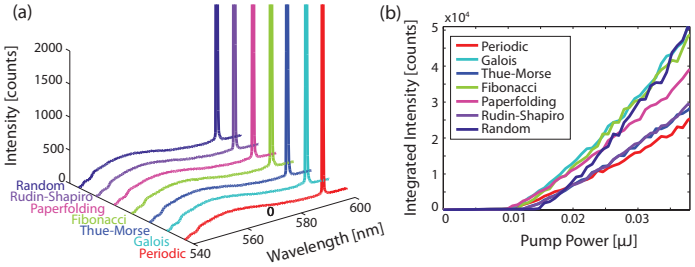

Figure 5.2: Spectra above the lasing threshold for periodic, Galois, Thue-Morse, Fibonacci, Paperfolding, Rudin-Shapiro and random arrays. The lasing wavelength is the same to within 1 nm for all arrays and corresponds to the wavelength for which the 2^{nd} order Bragg diffraction condition holds for a pitch of 380 nm. In b) threshold curves are shown for all arrays. From these curves, we obtain threshold pump powers of 12.5 μJ, 13.5 μJ, 15.6 μJ, 14.6 μJ, 12.5 μJ, 15.6 μJ, 18.7 μJ,

path at a focal distance away from the back focal plane of the imaging objective, in between the dichroic mirror and the tube lens of the CCD. As in previous chapters, images represent the output intensity as function of parallel emission wave vector $\mathbf{k}_{||} = \omega/c(\cos\phi, \sin\phi)\sin\theta$, where θ corresponds to polar angle (angle with the optical axis), and ϕ to azimuthal angle. Thus the center of each image corresponds to the optical axis, and the outer rim to the microscope NA (1.45)

The fourier image of the periodic lattice shows a single peak in the center, which indicates lasing at the second order Bragg condition. All quasiperiodic structures show additional structure. The structure ranges from discrete peaks that are comparable in intensity to the $\mathbf{k}_{||} = 0$ peak for the quasiperiodic lattices, (periodic up to Paperfolding), to a smoother (but speckled) background for the Rudin-Shapiro and randomized case.

Comparing these fourier images with the fourier transforms in figure 5.1 it can be seen that the pattern in the fourier image correspond to the fourier transform of the lattice. Therefore, whereas the lasing mode is unchanged when varying the periodicity from periodic to aperiodic, the outcoupling of the lasing mode is altered distinctly by the lattice. A physical picture is that essentially the underlying laser mode is the same in all lattices, meaning it is formed by second order Bragg diffraction and carries wavevectors $\mathbf{k}_{||} = 0$, plus all diffraction orders of the original lattice. Upon outcoupling the $\mathbf{k}_{||} = 0$ wave inherits the structure factor of the lattice as wave vector distribution. Thus the lasing output has exactly the same wave vector structure as the diffraction pattern one would obtain upon normal incidence excitation from the far field (in the limit of weak multiple scattering interactions between particles, i.e., in the limit of equally strong dipole moments on all sites).

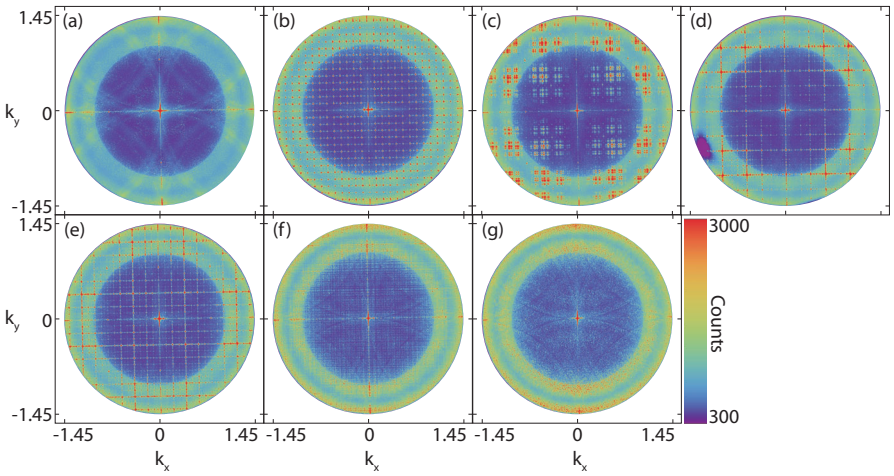

Figure 5.3: Fourier images far above threshold, for periodic (a), Galois (b), Thue-Morse (c), Fibonacci (d), Paperfolding (e), Rudin-Shapiro (f), and Random (g). The fourier images are obtained for an excitation energy of 0.05 μJ. For all quasiperiodic structures extra peaks appear besides the 2nd order Bragg peak in the middle at $\mathbf{k}_{||} = 0$.

5.5 Real space output

In addition to fourier space imaging we have also acquired real space images above and below threshold. Below-threshold real-space images show plain poissonian noise, as we also reported for randomized lattices in Chapter 4. However above threshold patterns with large intensity fluctuations appear, which for random systems are known as speckle [42]. Examples are shown in figure 5.4 for all lattices. Clearly the speckle is not random, and instead presents a pattern that reflects the lattice in a nontrivial way. When taking an autocorrelation of these real space images, the difference in speckle patterns between the different structures becomes even clearer. In particular, the quasiperiodic lattices show long range correlations, while instead the patterns with lower spectral flatness show a narrow autocorrelation that has diffraction limited width.

We note that speckle patterns, while seemingly entirely random, in fact can be used for applications due to their autocorrelation function. For instance, improvements to microscopy have recently been show on basis of using speckle. Bertolotti et al. [43] have shown non-invasive imaging *through* opaque media using the so-called "memory effect", whereby speckle patterns obtained upon transmission through a random medium are correlated as function of incidence angle [44]. Also, Mudry et al. [45] have reported imaging of objects using illumination with speckle in a form of structured illumination microscopy, while Katz et al. [46] have shown single shot imaging of objects through completely opaque media upon incoherent illumination. The key in these works is that the autocorrelation of speckle through a random medium is well known, and that the object shape is imprinted in the image as a convolution of

the object and speckle autocorrelation. From our work it appears that we can make light sources on basis of deterministic aperiodic arrays that produce speckle patterns with controlled auto correlations. In essence this gives control over the point-spread function of speckle based imaging techniques, which may be used for extending speckle-based imaging techniques, similar to point-spread function control in the more usual raster-scanning imaging techniques [47], or the use of gratings as illumination in Structured Illumination Microscopy [48, 49]. Aside from this potential application, the importance of our real-space and Fourier space results taken together is that by deterministically removing particles from the original diffractive array, it is possible to make a laser with an output that does not emit a single beam, but in fact emits with characteristics that are simply inherited from the binary amplitude mask that one imprints by simply removing particles. We expect that this idea also extends to phase masks that one could generate by changing particle sizes.

5.6 Lasing at other diffraction conditions

Periodic systems are expected to only support extended Bloch states, and to only lase at Bragg conditions. Quasiperiodic systems, in contrast, may support lasing at different d/λ ratios, i.e., at Bragg-like conditions that appear as strong features in the Fourier transform, yet do not correspond to a strict Bragg condition. In addition, aperiodic systems have been predicted to support critically localized modes. For these reasons, it is important to also analyze geometries that do not support lasing on the 2nd Bragg diffraction order. In figure 5.5h spectra are shown for maximum excitation power for arrays with a pitch of 300 nm. For this pitch, within the bandwidth of the dye the 1^{st} and 2^{nd} order Bragg diffraction condition can not be fulfilled. This explains why the periodic array does not show any lasing: Bragg diffraction can not create a standing wave for laser feedback. For the other lattices, we do see lasing at various wavelengths. In particular, for the quasiperiodic lattices (Galois up to Paperfolding) we see discrete and reproducible lasing lines at low thresholds. For the Rudin-Shapiro and randomized lattice, in contrast, we have to pump significantly harder (0.192 μJ for Rudin-Shapiro and 0.289 μJ for the Random array, compared to 0.042 μJ for the Fibonacci structure), to then obtain random lasing peaks. These observations are evident in figure 5.5 in that the quasiperiodic cases show sharp peaks on the familiar Rh6G spontaneous emission spectrum, while the Rudin-Shapiro and randomized lattice show spectral narrowing due to ASE peak near the gain maximum (550 nm), on top of which random lasing peaks occur.

In addition to spectra, we show fourier images for maximum excitation power in figure 5.5a-g. For the periodic lattice, the only visible features are four circles, indicating that emission occurs preferentially in the wave guide mode (circle radius of curvature given by the mode index), that is coupled out diffractively, giving rise to a repeated zone scheme dispersion slice (averaged over the bandwidth of the dye). For the Rudin-Shapiro and randomized case, the structure is very similar, though the circles appear narrower. This narrowing is due to the fact that amplified spontaneous

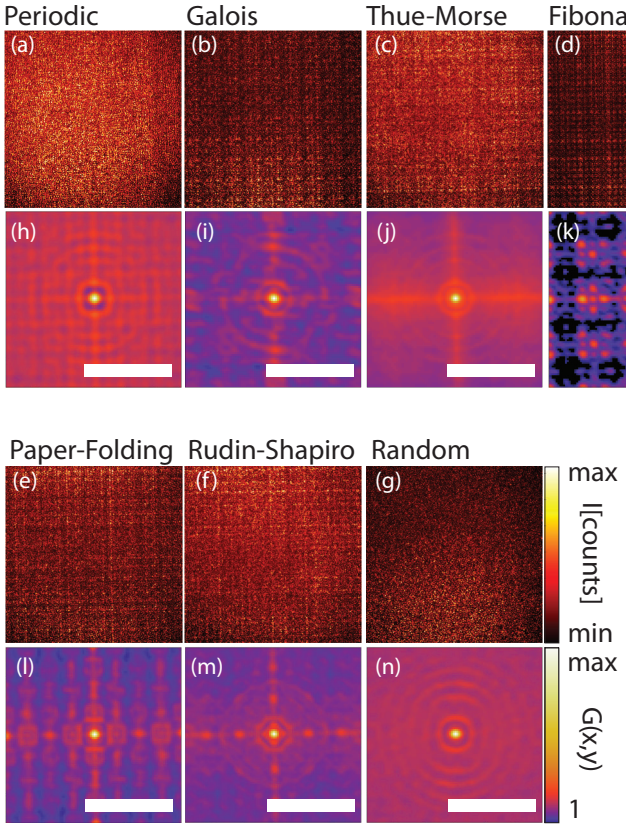

Figure 5.4: Real space images and the logarithm of the normalized autocorrelation far above the lasing threshold for all structures. The real space images have a field of view of 20 μm, and a clipped colorscale [ranges (223, 1898) (a), (225, 1423) (b), (204, 1051) (c), (175, 512) (d), (241, 1333) (e), (189, 905)) (f), (189, 818) (g); ranges corresponding to 1.4 times the minimum number of counts to 0.6 times the maximum number of counts]. Color ranges for the resulting autocorrelations range from 1.0 (minimum, no excess correlation) to the maximum correlation attained at $(x, y) = (0, 0)$, which is for panels (h-n) 1.05, 1.12, 1.07, 1.14, 1.09, 1.07, 1.1. We ascribe no particular meaning to this value, besides the fact that it is a measure for how far above threshold data was taken. The scalebar is 3 μm for the autocorrelations.

emission narrows the spectrum, which in turn reduces blurring of the observed bands. As the pitch is now reduced (larger **G**, shifting the origins of the cirles outward) the circles do not intersect at $\mathbf{k}_{||}$, but rather at four intersection points at approximately $k_{||}/k_0 \sim 0.4$ For the lasing lattices, again lasing spots appear across the entire back aperture. However, now the pattern does not reflect the Fourier transform of the lattice.

We assign the observation of new lasing conditions to the fact that the aperiodic arrays have many more peaks in the fourier spectrum, which give rise to new Bragg-like diffraction conditions. This can be illustrated using a calculated free-photon band

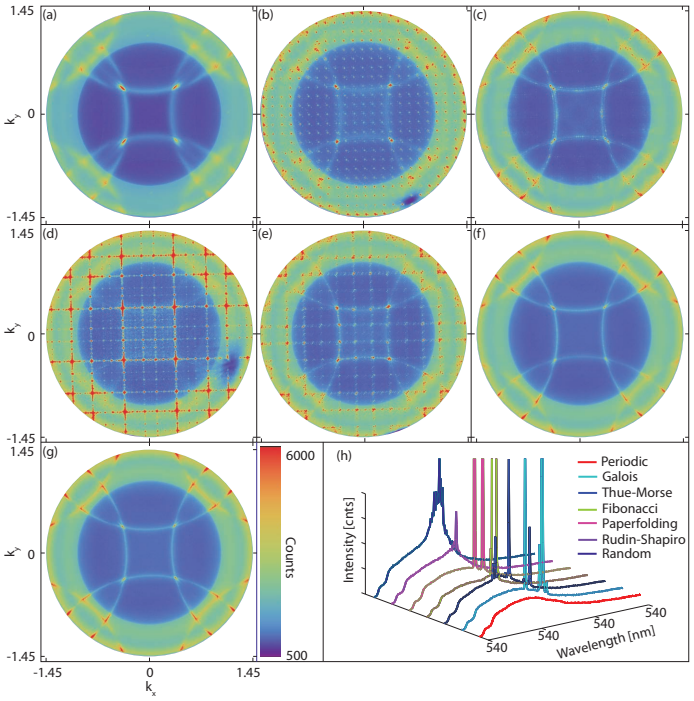

Figure 5.5: Fourier images above lasing threshold for a pitch of 300 nm (a-g) and spectra at maximum pump power, for periodic (a), Galois (b), Thue-Morse (c), Fibonacci (d), Paperfolding (e), Rudin-Shapiro (f) and random (g) arrays. As can be seen in figure (h) the lasing wavelength is different for each structure, and lasing can not be assigned to a Bragg condition of the underlying lattice. Moreover the periodic system does not show a lasing peak.

diagram as shown in figure 5.6. For a periodic system, one can find the repeated-zone scheme free photon dispersion by convolving the dispersion relation $|\mathbf{k}_{||}| = \omega n_{WG}/c$ with the structure factor of the lattice, i.e., the comb of δ-peaks situated at $(m,n)2\pi/d$. Here convolution is over wave vector. Although a band structure has no formal meaning for systems that are not periodic, one can arguably find an apparent repeated-zone scheme free photon dispersion for quasi periodic systems by convoluting the free-photon dispersion relation with the structure factors in Fig. 5.1. Examples are shown for the case of a Fibonacci, Galois and Paperfolding lattice. Indicated as horizontal lines are normalized lasing frequencies ($n_{WG}d/\lambda_0$) at which we obtain lasing. Samples with $d = 380$ nm lase at 2nd order Bragg diffraction, while at half the pitch $d = 190$ nm, lasing matches the 1st order Bragg diffraction. The $d = 300$ samples lase at various conditions, notably at a band crossings that occur in several of the structures at $d/\lambda_{WG} \approx 0.8$, and at the M-point in case of the Galois lattice. While in retrospect, lasing conditions in these samples may be reasonably explained by "strong"

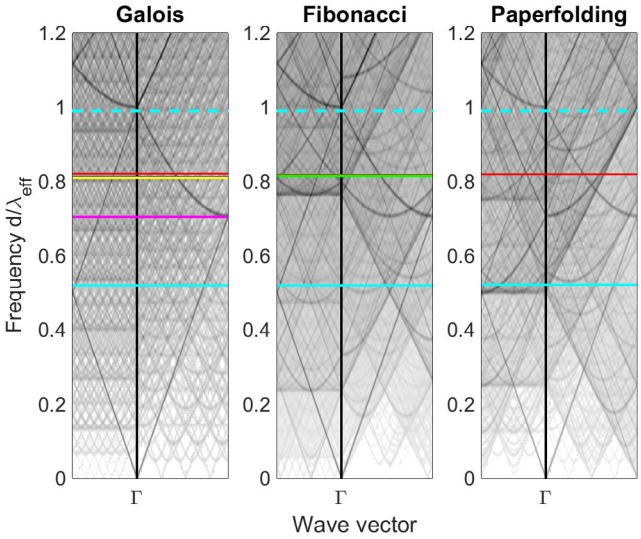

Figure 5.6: Calculated band diagrams for a Galois, Fibonacci and Paperfolding array obtained by convolving the lattice structure factor with the free photon dispersion. Note that special points in the unit cell are labelled as Γ, X, M, being $(0,0), (0,1)$ and $(1,1)$ in units of π/d. In all diagrams the dashed cyan lines represent measured lasing peak frequencies, for the lattices with 380, 190 and 300 nm, plotted in normalized units $n_{WG}d/\lambda$ (where λ is measured wavelength, d nominal pitch and $n_{WG} = 1.54$, assumed fixed). Solid (dashed) cyan lines represent the $d = 380$ nm ($d = 190$ nm) samples, lasing at second resp. first order Bragg diffraction. Other lines correspond to the $d = 300$ nm samples (plot colors in each diagram cycling through red, green, blue, yellow, magenta, brown - note that lines overlap for closeby lasing conditions).

crossings in the dispersion diagrams, predicting of dominant lasing conditions is not easy. One reason is that not just the appearance of a (pseudo)-Bragg condition is required, but also the dye gain window enters as a weighting factor.

5.7 Conclusion and outlook

We have shown lasing in quasi- and aperiodic plasmonic particle arrays and made a comparison with random and periodic systems. We show that, independent of the spectral flatness of the structure, lasing occurs on the 2nd order Bragg diffraction condition of the underlying lattice. However, above lasing threshold all fourier images show that directionality of the laser emission is strongly altered and resemble the pattern of the fourier transform of the lattice. We conclude that this is caused by the altered outcoupling due to the introduced quasi- or aperiodicity. In addition, the periodicity manifests itself in the speckle pattern, as is most clear from the autocorrelations of the above threshold real space images. Finally, we have shown data measured on lattices with an underlying particle pitch equal to 190 (half the 2nd order Bragg condition)

and 300 nm. We demonstrated multifrequency lasing, where the lasing condition is related to extra peaks in the fourier transform of the lattice, or in other words, extra periodicities can replace the 2nd order Bragg condition. We substantiate this claim by showing calculated band diagrams for Galois, Fibonacci and Paperfolding lattices indicating the lasing frequencies.
We show that it is possible to tune the speckle patterns and control their autocorrelations. This might be used in several applications, such as speckle based imaging techniques and Structured Illumination Microscopy.
For future experiments it would be interesting to determine if it is possible to optimize the system to give maximum field enhancement in such a way that it benefits lasing, e.g. results in a lower lasing threshold. In addition, our work paves the way to study many other quasiperiodicities in the context of lasing. More specific, systems without an underlying square grid can still have band edge modes. For example, it has been predicted that Golden-Angle spirals exhibit an analogue to the band edge modes of periodic systems [25, p. 164] and it would be interesting to find out if lasing can take place on these band edge modes. Penrose [50] and hyperuniform [51] lattices are other examples for which band gaps and localized states exists and which would be interesting to study in the context of lasing.

5.8 Appendix

Quasi- or aperiodicity can be implemented in an optical system by adjusting any optical property according to a given generation sequence. For example, in Bragg stacks the thickness of the reflecting layers can be altered[40], or in photonic crystals the hole size can be varied[52]. In this work we introduce aperiodicity by removing particles. The periodic array is the starting configuration for the other six periodicities, where the random array is generated by randomly removing 50 % of the particles. The remaining five periodicities are generated using generation sequences as also used by Cao, dal Negro and Borivskina [25]

Fibonacci The Fibonacci sequence is well known because of the many situations in which it can be applied. The sequence starts with two elements, $F_0 = 1$ and $F_1 = 1$. All following sequence elements F_n are generated by adding the preceding two elements together, or $F_n = F_{n-2} + F_{n-1}$. The resulting sequence therefore is 1, 1, 2, 3, 5, 8, 13, 21, 34, etc. Instead of using numbers, we can assign an entity to F_0 and F_1 in which case the element F_n is generated by concatenating, instead of adding. If we set $F_0 = A$ and $F_0 = B$, then the first sequence elements become A, B, AB, BAB, ABBAB, BABABBAB, ABBABBABABBAB, etc. In our samples we use the convention that A corresponds to absence of a particle, and B corresponds to presence of a particle, where the only free parameter is the distance between lattice sites, which we set equal to 380 nm for all structures. A 1D Fibonacci grating therefore is obtained by taking the sequence element that has enough lattice sites to span a specified length. To extend the 1D grating to a 2D particle array, several methods exist[53], however we use the

most straightforward method [36]. For each lattice site m in the 1D particle row, we transpose the row to define a column vector. This directly defines the mth column of the 2D lattice whenever the mth entry in the 1D grating is occupied. When the mth site, however, was empty the mth colun is obtained by flipping all entries (an empty site becomes a particle and vice versa).

Galois We generate the Galois array using $G_{n+4} = G_{n+1} + G_n$. The starting values are $G_1 = 1$, $G_2 = 0$, $G_3 = 0$, and $G_4 = 0$. If $G_{n+4} = G_{n+1} + G_n > 1$ then we set $G_n = 0$, and we use the convention that a value of 1 indicates the presence of a particle, whereas 0 is equivalent to an empty position. Now the 1D sequence is a concatenation of all G_n elements. The extension to 2D is generated as in the case of the Fibonacci array.

Thue-Morse The Thue-Morse sequence is generated by concatenating a Boolean sequence with its complement. Starting with $T_1 = 0$ we obtain for the following elements 01, 0110, 01101001, 0110100110010110, etc. Using the same conventions as before and extending in the same way to 2D we obtain the complete Thue-Morse array.

Paper Folding A Paper Folding sequence is the sequence of left and right folds in a paper that has been folded in half in the same direction n times. It is obtained by creating a neighbouring element for each 0 or 1, where this added element alternates between 0 and 1. If we start with $P_1 = 1$, then the next term is $P_2 = \mathbf{110}$ and the following terms are $\mathbf{1101100}$, $\mathbf{110110011100100}$, etc. Again, extension to 2D proceeds as for the Fibonacci case.

Rudin-Shapiro The Rudin-Shapiro sequence has the largest value for spectral flatness and is closest to the 50 % random array, but it is still constructed from a generation sequence. We start with a seed, A from which we will construct a row of 4 letters, A, B, C and D. We use the following generation rules; A→AC, B→DC, C→AB and D→AC and put the 2 generated elements at position $i \cdot 2$ and $i \cdot 2 - 1$. Thus, we get A, AC, ACAB, ACABACDC, ACABACDCDC, etc. Now we use 4 rules to convert from letters to 0 and 1 values, namely A→0, B→1, C→0, and D→1. From here on, we use the same conventions as in the other arrays to convert from binary values to particles and from a 1D row to a 2D array.

References

[1] W. L. Barnes, A. Dereux, and T. W. Ebbesen, *Surface plasmon subwavelength optics*, Nature **424**, 824 (2003).

[2] P. L. Stiles, J. A. Dieringer, N. C. Shah, and R. R. Van Duyne, *Surface-enhanced Raman spectroscopy*, Annu. Rev. Anal. Chem. **1**, 601 (2008).

[3] G. Lozano, D. J. Louwers, S. R. K. Rodriguez, S. Murai, O. T. A. Jansen, M. A. Verschuuren, and J. Gómez Rivas, *Plasmonics for solid-state lighting: enhanced excitation and directional emission of highly efficient light sources*, Light. Sci. Appl. **2**, e66 (2013).

[4] J. N. Anker, W. P. Hall, O. Lyandres, N. C. Shah, J. Zhao, and R. P. Van Duyne, *Biosensing with plasmonic nanosensors*, Nat. Mater. **7**, 442 (2008).

[5] M. E. Stewart, C. R. Anderton, L. B. Thompson, J. Maria, S. K. Gray, J. A. Rogers, and R. G. Nuzzo, *Nanostructured plasmonic sensors*, Chem. Rev. **108**, 494 (2008).

[6] S. Mokkapati and K. R. Catchpole, *Nanophotonic light trapping in solar cells*, J. Appl. Phys. **112**, 101101 (2012).

[7] H. A. Atwater and A. Polman, *Plasmonics for improved photovoltaic devices*, Nat. Mater. **9**, 205 (2010).

[8] L. Zhao, K. L. Kelly, and G. C. Schatz, *The extinction spectra of silver nanoparticle arrays: Influence of array structure on plasmon resonance wavelength and width*, J. Phys. Chem. B **107**, 7343 (2003).

[9] A. A. Penzkofer and Y. Lu, *Fluorescence quenching of rhodamine 6g in methanol at high concentration*, Chem. Phys. **103**, 399 (1986).

[10] G. Vecchi, V. Giannini, and J. Gómez Rivas, *Shaping the fluorescent emission by lattice resonances in plasmonic crystals of nanoantennas*, Phys. Rev. Lett. **102**, 146807 (2009).

[11] M. J. H. Marell, B. Smalbrugge, E. J. Geluk, P. J. van Veldhoven, B. Barcones, B. Koopmans, R. Notzel, M. K. Smit, and M. T. Hill, *Plasmonic distributed feedback lasers at telecommunications wavelengths*, Opt. Express **19**, 15109 (2011).

[12] J. Y. Suh, C. H. Kim, W. Zhou, M. D. Huntington, D. T. Co, M. R. Wasielewski, and T. W. Odom, *Plasmonic bowtie nanolaser arrays*, Nano Lett. **12**, 5769 (2012).

[13] J. Stehr, J. Crewett, F. Schindler, R. Sperling, G. von Plessen, U. Lemmer, J. M. Lupton, T. A. Klar, J. Feldmann, A. W. Holleitner, M. Forster, and U. Scherf, *A low threshold polymer laser based on metallic nanoparticle gratings*, Adv. Mater. **15**, 1726 (2003).

[14] D. S. Wiersma, M. P. Vanalbada, and A. Lagendijk, *Random laser*, Nature **373**, 203 (1995).

[15] D. Wiersma and A. Lagendijk, *Light diffusion with gain and random lasers*, Phys. Rev. E **54**, 4256 (1996).

[16] H. Cao, Y. Zhao, S. Ho, E. Seelig, Q. Wang, and R. Chang, *Random laser action in semiconductor powder*, Phys. Rev. Lett. **82**, 2278 (1999).
[17] D. S. Wiersma, *The physics and applications of random lasers*, Nat. Phys. **4**, 359 (2008).
[18] E. Maciá, *Exploiting aperiodic designs in nanophotonic devices*, Rep. Prog. Phys. **75**, 036502 (2012).
[19] A. Gopinath, S. V. Boriskina, N.-N. Feng, B. M. Reinhard, and L. Dal Negro, *Photonic-plasmonic scattering resonances in deterministic aperiodic structures*, Nano Lett. **8**, 2423 (2008).
[20] C. Forestiere, G. F. Walsh, G. Miano, and L. Dal Negro, *Nanoplasmonics of prime number arrays*, Opt. Express **17**, 24288 (2009).
[21] M. Florescu, S. Torquato, and P. J. Steinhardt, *Complete band gaps in two-dimensional photonic quasicrystals*, Phys. Rev. B **80**, 155112 (2009).
[22] L. Dal Negro and S. V. Boriskina, *Deterministic aperiodic nanostructures for photonics and plasmonics applications*, Laser Photonics Rev. **6**, 178 (2012).
[23] S. V. Boriskina and L. Dal Negro, *Sensitive label-free biosensing using critical modes in aperiodic photonic structures*, Opt. Express **16**, 12511 (2008).
[24] S. V. Boriskina, A. Gopinath, and L. Dal Negro, *Optical gaps, mode patterns and dipole radiation in two-dimensional aperiodic photonic structures*, Phys. Rev. E **41**, 1102 (2009).
[25] L. Dal Negro, Optics of aperiodic structures, Pan Stanford Publishing Pte. Ltd., Stanford, 2014.
[26] Z. V. Vardeny, A. Nahata, and A. Agrawal, *Optics of photonic quasicrystals*, Nat. Photonics **7**, 177 (2013).
[27] E. Maciá, *The role of aperiodic order in science and technology*, Rep. Prog. Phys. **69**, 397 (2006).
[28] D. Levine and P. J. SteinhardtLubin, *Quasicrystals. i. definition and structure*, Phys. Rev. B **34**, 596 (1986).
[29] D. Shechtman, I. Blech, D. Gratias, and J. W. Cahn, *Metallic phase with long range orientational order and no translation symmetry*, Phys. Rev. Lett. **53**, 1951 (1984).
[30] B. le Feber, J. Cesario, H. Zeijlemaker, N. Rotenberg, and L. Kuipers, *Exploiting long-ranged order in quasiperiodic structures for broadband plasmonic excitation*, Appl. Phys. Lett. **99**, 019903 (2011).
[31] M. Ghulinyan, C. Oton, L. Dal Negro, L. Pavesi, R. Sapienza, M. Colocci, and D. Wiersma, *Light-pulse propagation in Fibonacci quasicrystals*, Phys. Rev. B **71**, 094204 (2005).
[32] M. Stockman, *Inhomogeneous eigenmode localization, chaos, and correlations in large disordered clusters*, Phys. Rev. E **56**, 6494 (1997).
[33] C.-W. Lee, G. Singh, and Q. Wang, *Light extraction - a practical consideration for a plasmonic nano-ring laser*, Nanoscale **5**, 10835 (2013).
[34] S. Y. Lee, J. J. Amsden, S. V. Boriskina, A. Gopinath, A. Mitropolous, D. L. Kaplan, F. G. Omenetto, and L. Dal Negro, *Spatial and spectral detection of protein monolayers with deterministic aperiodic arrays of metal nanoparticles*, Proc. Natl. Acad. Sci. U. S. A. **107**, 12086 (2010).
[35] J. H. Lin, W. L. Chang, H.-Y. Lin, T.-H. Chou, H.-C. Kan, and C. C. Hsu, *Enhancing light extraction efficiency of polymer light-emitting diodes with a 12-fold photonic quasi crystal*, Opt. Express **21**, 22090 (2013).
[36] L. Dal Negro, N.-N. Feng, and A. Gopinath, *Electromagnetic coupling and plasmon localization in deterministic aperiodic arrays*, J. Opt. A: Pure Appl. Opt. **10**, 064013 (2008).
[37] A. Lagendijk, B. van Tiggelen, and D. Wiersma, *Fifty years of Anderson localization*, Phys.

Today **62**, 24 (2009).

[38] M. Notomi, H. Suzuki, T. Tamamura, and K. Edagawa, *Lasing action due to the two-dimensional quasiperiodicity of photonic quasicrystals with a Penrose lattice*, Phys. Rev. Lett. **92**, 123906 (2004).

[39] J.-K. Yang, S. V. Boriskina, H. Noh, M. J. Rooks, G. S. Solomon, L. Dal Negro, and H. Cao, *Demonstration of laser action in a pseudorandom medium*, Appl. Phys. Lett. **97**, 223101 (2010).

[40] L. Mahler, A. Tredicucci, F. Beltram, C. Walther, J. Faist, H. E. Beere, D. A. Ritchie, and D. S. Wiersma, *Quasi-periodic distributed feedback laser*, Nat. Photonics **4**, 165 (2010).

[41] D. Luo, Q. G. Du, H. T. Dai, H. V. Demir, H. Z. Yang, W. Ji, and X. W. Sun, *Strongly linearly polarized low threshold lasing of all organic photonic quasicrystals*, Sci. Rep. **2**, 627 (2012).

[42] G. van Soest, F. J. Poelwijk, and A. Lagendijk, *Speckle experiments in random lasers*, Phys. Rev. E **65**, 046603 (2002).

[43] H. Yilmaz, E. G. van Putten, J. Bertolotti, A. Lagendijk, W. L. Vos, and A. P. Mosk, *Speckle correlation resolution enhancement of wide-field fluorescence imaging*, Optica **2**, 424 (2015).

[44] I. Freund, M. Rosenbluh, and S. Feng, *Memory effects in proagation of optical waves through disordered media*, Phys. Rev. Lett. **61**, 2328 (1988).

[45] E. Mudry, K. Belkebir, J. Girard, J. Savatier, E. Le Moal, C. Nicoletti, M. Allain, and A. Sentenac, *Structured illumination microscopy using unknown speckle patterns*, Nat. Photonics **6**, 312 (2012).

[46] O. Katz, P. Heidmann, M. Fink, and S. Gigan, *Non-invasive single-shot imaging through scattering layers and around corners via speckle correlations*, Nat. Photonics **8**, 784 (2014).

[47] E. T. F. Rogers, J. Lindberg, T. Roy, S. Savo, J. E. Chad, M. R. Dennis, and N. I. Zheludev, *A super-oscillatory lens optical microscope for subwavelength imaging*, Nat. Mater. **11**, 432 (2012).

[48] M. G. L. Gustafsson, L. Shao, P. M. Carlton, C. J. R. Wang, I. N. Golubovskaya, W. Z. Cande, D. A. Agard, and J. W. Sedat, *Three-dimensional resolution doubling in wide-field fluorescence microscopy by structured illumination*, Biophys. J. **94**, 4957 (2008).

[49] A. Sentenac, P. C. Chaumet, and K. Belkebir, *Beyond the Rayleigh criterion: Grating assisted far-field optical diffraction tomography*, Phys. Rev. Lett. **97**, 243901 (2006).

[50] M. Notomi, H. Suzuki, T. Tamamura, and K. Edagawa, *Lasing action due to the two-dimensional quasiperiodicity of photonic quasicrystals with a Penrose lattice*, Phys. Rev. Lett. **92**, 123906 (2004).

[51] W. Man, M. Florescu, K. Matsuyama, P. Yadak, G. Nahal, E. Hashemizad, Seyed Williamson, P. Steinhardt, S. Torquato, and P. Chaikin, *Photonic band gap in isotropic hyperuniform disordered solids with low dielectric contrast*, Opt. Express **21**, 19972 (2013).

[52] H. Noh, J.-K. Yang, S. V. Boriskina, M. J. Rooks, G. S. Solomon, L. Dal Negro, and H. Cao, *Lasing in Thue-Morse structures with optimized aperiodicity*, Appl. Phys. Lett. **98**, 201109 (2011).

[53] A. Barbe and F. Von Haeseler, *Correlation and spectral properties of multidimensional Thue-Morse sequences*, Int. J. Bifurcation Chaos **17**, 1265 (2007).

Summary

Through light we see the world around us, both in every day life, but also in the sense that through light mankind has elucidated the nature of stars, cells, and even the structure of atoms. This fact is the main reason why light has been the subject of so many studies and still is today. Humans have been developing their ability to manipulate light since ancient history, ever since we were capable of making fire to create light. Research on light has for a large part been purely curiousity driven, with the sole purpose to get a fundamental understanding of the physics behind processes involving light. Yet, nowadays, steering and manipulating light has turned out so important for every day life that we could not even think of what life would be like without the devices originating from discoveries that are in one way or another related to understanding and using light. For example, understanding and being able to use light is essential for designing efficient solar cells, in which light is converted into electricity instead of being absorbed and dissipated as heat. Another application is in lighting. We use artificial light everywhere around us and designing more efficient light sources has, as do solar cells, a huge environmental interest. A third area in which light can be used is information technology. At the moment, information technology is mainly based on electronic circuits in which electrons are the information carriers. To keep pace with Moore's law that describes that on-chip circuit density and operation speed increase exponentially, a technology other then the current technology using electronic circuits needs to be developed since electronics suffers from issues with dissipation, and signal bandwidth. If one could steer and manipulate light on a chip, just as is possible with electrons in an electronic circuit, then light could provide the solution. The great benefits of light in the context of information technology is that first, it travels faster then signals do in an electronic circuit, second, it can be losslessly transported, and third it can be multiplexed as a light signal typically contains many colors each of which can be an individual information channel. Two challenges in using light for such applications are 1) the interaction strength of light with matter is weak compared to matter-matter interactions which makes it a challenge to manipulate light just as is done for electrons, and 2) light is limited by the diffraction limit, as is any wave. For visible light, this size limit is larger then the typical size of components in an electrical circuit. In the field of plasmonics exactly these two challenges are

adressed. Plasmonic materials are materials, typically metals such as gold or silver, in which electrons move freely, such that incident light can strongly couple to the free electron cloud. Besides the increased coupling strength, electromagnetic fields coupled to these free electrons are also confined, enabling subdiffraction limited light fields.
Current research in the field of nanophotonics revolves around manipulating light at the nanoscale, such that we can benefit from its potential in the above mentioned applications, but also to get a fundamental understanding. In this thesis, we use plasmonics to create a laser. Since the birth of plasmonics, there has been an interest in designing lasers with plasmonics. The large interest has been mainly motivated by applications, e.g. from the perspective of creating an on chip coherent light source that is exceptionally small, smaller than the diffraction limit. In this thesis, we focus on obtaining a fundamental understanding of a simple system that consists of the following ingredients: (1) a gain medium, and (2) periodic arrays of strongly scattering plasmon particles. We start with very basic questions. What are the requirements to get lasing? How does strong scattering of plasmonic particles change these requirements compared to dielectric lasers that use similar feedback by scattering? How much can we disturb this system without destroying our laser?
In Chapter 1 we first explain what makes plasmonic particles interesting in terms of their scattering properties, and motivate why to use them to create a laser cavity. Second, we introduce the ingredients of our laser, namely the physics of plasmon particles, of feedback by periodic diffractive systems, and of gain. The subject of lasing requires a basic understanding of the Jablonski diagram describing the energy levels of fluorophores, spontaneous and stimulated emission and basic laser behaviour. Finally, we review the subject of plasmon lasers in the broadest sense and motivate how our work complements other plasmon laser types.
In Chapter 2 experimental results are presented for a laser in which we use a simple diffractive square array of silver disks embedded in a waveguide with gain. We demonstrate that lasing can occur when using plasmonic scatterers as feedback elements. We not only show the typical linewidth narrowing and threshold curves expected for lasing, but in addition measure fourier images, and show how to map dispersion diagrams from fluorescence emission, making use of fourier imaging. Fourier plane imaging is a method in which one measures quantities as function of wave vector, i.e., angle, instead of imaging real space, i.e., position. Such dispersion diagrams present the optical analogon of an electronic band structure, and are useful tools in studying lasing. Finally, we compare measurements done with silver scatterers with measurements done on gold and TiO_2 scatterers. From this, we conclude that silver scatterers alter the dispersion diagram that summarizes the mode structure of the periodic scattering system that provides the feedback for lasing much more then gold and TiO_2 do. This is due to its strong plasmonic scattering, as witnessed by e.g. the size of the stop gap in the band diagram for silver. In this study, the resonance frequency of the scatterers in the waveguide is red shifted with respect to the sponteanous emission spectrum of the dye. In Chapter 3 we show results on a system containing again silver scatterers but where we tune the resonance frequency of our silver scatterer throught the emission frequency of the emitter. To enable this, we use a FRET pair of dyes to red shift

the frequency window in which we can obtain gain while enabling excitation at 532 nm. Subsequently, we tune the resonance frequency of our scatterer by changing the size, where we vary the silver disk diameter from 40 to 125 nm. Using polarization-resolved spectroscopic Fourier imaging we unravel the band structure dependence of particle size. From the data we conclude that 1) relative stop gap width correlates with scattering strength and 2) the band edge on which the system starts to lase is determined by whether particle resonance is above or below the 2nd order Bragg diffraction lasing condition. Having established the effect of strong scattering strength, in Chapter 4 we change direction by studying randomized particle lattices. Because plasmonic particles are such good scatterers, we hypothesize that disturbing our system by randomization should have less of an effect on lasing. In Chapter 4 we demonstrate that this is indeed the case. We introduce randomness, starting from a square particle grid and either randomly removing particles or randomly repositioning the particles within a set area. We show that lasing persists even when 99% of the particles are randomly removed. Remarkably such a strong perturbation leaves the lasing condition, i.e., the spectral position and width of the laser line, unaffected, while only having a moderate effect on the lasing threshold. Moreover, we introduce correlation methods, and intensity statistics analysis to analyse real space speckle images. This technique allows us to 1) differentiate between lasing and spontaneous emission, and 2) show that strongly randomized lattices exhibit different speckle statistics as compared to the perfect periodic array. Finally, in Chapter 5 we move into the realm of aperiodic and quasiperiodic system, thereby studying systems that are intermediate to periodic and randomized lattices. We create aperiodic lattices by applying deterministic number sequences to decide which particles in an underlying square lattice to keep, and which to remove. In this way we can create quasi-crystalline lattices, such as Galois and Fibonacci lattices, as well as lattices like the Rudin-Shapiro structure, that have a Fourier transform that is almost as flat as that of a random lattice. We show that when choosing the underlying pitch to match the 2nd order Bragg condition, lasing is hardly affected by the altered periodicity in the sense that the lasing mode is the same as for the periodic case. However, the quasi- or aperiodic structure is visible in the above-threshold fourier images, which reflect the fourier transform of the particle lattice. In addition, speckle statistics shows that speckle is very much determined by the spatial structure of the aperiodic lattice. In other words, the spatial speckle autocorrelation is quite different from aperiodic structure to aperiodic structure. Finally, we extend the study to lattices with a different underlying particle pitch and show that here lasing can occur on extra diffraction conditions that do not exist in periodic lattices, but appear in quasi-crystalline structures.

Samenvatting

Met licht kunnen we de wereld om ons heen waarnemen. Dit gebruiken we niet alleen in ons dagelijkse bestaan, maar ook heeft licht de mensheid in staat gesteld een inzicht te krijgen in de samenstelling en vorming van sterren, cellen, en zelfs de structuur van atomen. Hierdoor is licht door de eeuwen heen het onderwerp van vele studies geweest en ook vandaag de dag nog wordt licht onderzocht. Al sinds de mensheid in staat is om vuur te maken om licht te creeëren kunnen we licht manipuleren. Onderzoek naar licht was altijd grotendeels gedreven door nieuwsgierigheid waarbij het doel was om een fundamenteel begrip te krijgen van de natuurkunde achter processen die te maken hebben met licht. Tegenwoordig is gebleken dat deze nieuwsgierigheidsgedreven studies ertoe geleid hebben dat we licht zo kunnen sturen en manipuleren dat we het kunnen gebruiken in vele praktische toepassingen en technologieën. We kunnen ons niet meer voorstellen hoe ons leven er uit zou zien zonder de toepassingen die hun oorsprong hebben in ontdekkingen die op de één of andere manier gerelateerd zijn aan het begrip van licht. Denk bijvoorbeeld aan zonnecellen, waarbij we optische technieken gebruiken om licht efficiënter te kunnen omzetten naar elektriciteit, in plaats van dat het geabsorbeerd en gedissipeerd wordt als warmte. Een andere toepassing is verlichting. Kunstmatig licht gebruiken we overal om ons heen, en het ontwerpen van een lichtbron die veel efficiënter is dan de gloeilamp van Edison heeft, net als zonnecellen, een belangrijke impact op het milieu. Een derde toepassingsgebied waar licht voor gebruikt kan worden is in de informatie technologie. Momenteel is informatietechnologie gebaseerd op elektronische circuits waarin elektronen de informatiedragers zijn. Moore's wet beschrijft dat de dichtheid van circuit elementen en hun snelheid exponentieel toenemen. Om deze voorspelling waar te blijven maken moet een nieuwe technologie ontwikkeld worden die anders is dan de huidige technologie die gebruik maakt van elektronische circuits, omdat elektronica uiteindelijk tegen grenzen aan zal lopen die gesteld worden door dissipatie en signaal bandbreedte. Als we de mogelijkheid hebben om op een chip licht te sturen en manipuleren net zoals dat bij elektronen mogelijk is, dan zou licht de oplossing kunnen brengen. Er zijn drie grote voordelen die licht biedt in de context van informatie technologie. Ten eerste plant licht zich sneller voort. Ten tweede kan licht zonder verliezen getransporteerd worden. Tot slot kunnen we licht multiplexen omdat het uit meerdere kleuren bestaat die elk

afzonderlijk een informatie kanaal kunnen vormen. Het feit dat het gebruik van licht in deze toepassing nog niet gerealiseerd is heeft twee oorzaken. Licht heeft een hele zwakke interactie met materie en dit maakt het lastig licht te manipuleren zoals gedaan wordt voor elektronen. Met andere woorden, het equivalent van een transistor is voor licht moeilijk te realiseren. Daarnaast wordt het gebruik van licht beperkt door de diffractielimiet, zoals dat voor elke golf het geval is. De diffractielimiet zegt dat het lichtveld altijd groter is dan de helft van de golflengte. Voor zichtbaar licht betekent dit dat de minimum afmeting altijd groter is dan de typische component grootte in een elektrisch circuit. Het werkgebied van de plasmonica adresseert precies deze twee uitdagingen. Plasmonische materialen zijn metalen, waarin de elektronen vrij kunnen bewegen. De wolk van vrije elektronen heeft intrinsiek een resonantie die sterk kan koppelen met invallend licht. Typische plasmonische materialen zijn metalen zoals goud en zilver waarbij zilver in het zichtbare deel van het optisch spectrum de voorkeur heeft qua verliezen. Behalve de versterkte koppeling tussen plasmonische materialen en licht zijn electromagnetische velden gekoppeld aan de vrije elektronen ook nauwer opgesloten, wat het mogelijk maakt de diffractielimiet te doorbreken.
Het huidige onderzoek in het veld van de nanofotonica draait om het manipuleren van licht op de nanoschaal zodat we licht kunnen gebruiken in de hierboven genoemde toepassingen, maar ook om een fundamenteel begrip te krijgen. In dit proefschrift gebruiken we nanofotonica om een laser te creëren. Al sinds de geboorte van plasmonica is er interesse geweest in het ontwerpen van lasers met plasmonische materialen. Deze grote interesse vloeit voornamelijk voort uit het vooruitzicht van toepassingen, zoals bijvoorbeeld het mogelijk maken van een coherente licht bron geintegreerd op een chip, die een afmeting heeft kleiner dan de diffractie limiet. In dit proefschrift richten we ons voornamelijk op het verkrijgen van een fundamenteel begrip van een simpel systeem dat bestaat uit de volgende ingrediënten: (1) een versterkend medium en (2) periodieke roosters van sterk verstrooiende plasmonische deeltjes. We beginnen met simpele basisvragen. Wat zijn de vereisten om lasing te krijgen in dit systeem? Hoe beïnvloedt de sterke verstrooing van zilveren deeltjes deze vereisten wanneer we een vergelijking maken met dielektrische lasers met dezelfde vorm van feedback? En hoeveel wanorde kunnen we in zo'n sterk verstrooiend rooster introduceren waarbij het systeem nog steeds als laser werkt?
In hoofdstuk 1 leggen we uit waarom plasmonische deeltjes zo interessant zijn in termen van hun verstrooiingseigenschappen. We motiveren waarom we ze gebruiken om een trilholte voor een laser te creëren. Vervolgens introduceren we de ingrediënten van onze laser, namelijk de natuurkunde van plasmon deeltjes, terugkoppeling door een periodiek diffractief systeem en versterking. Het onderwerp van lasers vereist basiskennis van het Jablonski diagram dat de energieniveaus beschrijft van fluoroforen, spontane en gestimuleerde emissie en generiek gedrag van lasers. Tot slot vatten we samen wat er in de literatuur al gerapporteerd is in de context van plasmon lasers en we motiveren hoe ons werk complementair is aan andere plasmon laser types.
In hoofdstuk 2 presenteren we experimentele resultaten voor een laser waarin we een simpel diffractief vierkant rooster van zilveren nanoschijven gebruiken die ingebed zijn in een golfgeleider met fluoroforen. We demonstreren dat dit systeem met plasmonische

deeltjes als terugkoppelingselement als laser werkt. We meten hierbij niet alleen de lijnbreedte versmalling en drempelcurves zoals ze er typisch uit zien voor een laser, maar complementair hieraan meten we ook fourier afbeeldingen. Fouriervlak beeldvorming is een methode waarin observabelen als functie van golfvector, en daarmee als functie van de hoek gemeten worden, in plaats van de gebruikelijke reeële beeldvorming waarbij observabelen als functie van posite afgebeeld worden. Daarnaast gebruiken we een techniek om fourier afbeeldingen langs één as spectraal op te lossen, wat ons in staat stelt bandendiagrammen te meten met fluorescentie. Zulke dispersie diagrammen zijn het optische analogon van een elektronische bandenstructuur, en zijn een nuttige techniek voor het bestuderen van periodieke plasmon structuren, en de lasers die we daaruit maken. Tot slot vergelijken we metingen gedaan met zilveren verstrooiers met metingen gedaan met gouden en titanium dioxide verstrooiers. Uit deze vergelijking kunnen we concluderen dat zilveren verstrooiers het dispersie diagram veel meer veranderen dan gouden en titanium dioxide verstrooiers doen, wanneer we het bandendiagram vergelijken met het ideale bandendiagram waarin tegengesteld propagerende golven geen interactie met elkaar hebben. Dit wordt veroorzaakt door de sterke plasmonische verstrooing van de zilverdeeltjes, zoals we kunnen opmaken uit bijvoorbeeld de grootte van de stopgap in het bandendiagram. In dit onderzoek is de resonantie frequentie van de verstrooiers in de golfgeleider roodverschoven ten opzichte van het spectrum van spontane emissie van de fluorofoor. In hoofdstuk 3 laten we resultaten zien van een systeem dat weer dezelfde zilveren verstrooiers bevat, maar waar we de resonantie frequentie van onze verstrooier door het emissie spectrum van de fluorofoor schuiven. Om dit mogelijk te maken gebruiken we een FRET paar van twee verschilende fluoroforen om het frequentie bereik waarin we versterking hebben te verschuiven naar langere golflengtes, maar waarmee we de fluoroforen nog steeds kunnen exciteren met een pompgolflengte van 532 nm. Vervolgens veranderen we de resonantie frequentie van de verstrooier door de grootte ervan te veranderen. Met behulp van polarisatie opgeloste spectroscopische fourier afbeeldingen ontravelen we de bandenstructuur als functie van deeltjesgrootte. Uit de data kunnen we concluderen dat 1) de relatieve stopgap breedte correleert met verstrooingssterkte, en 2) de bandkant waarop het systeem laseremissie begint uit te zenden wordt bepaald door of de deeltjesresonantie boven of beneden de tweede orde Bragg diffractie conditie is.

Waar hoofdstuk 2 en 3 draaiden om een volledige karakterisatie van lasers gemaakt uit periodieke roosters van deeltjes, richten we ons in hoofdstuk 4 en 5 op de vraag hoe dit systeem verandert als we het periodieke rooster ernstig verstoren. In hoofdstuk 4 bestuderen we deeltjesroosters met aanzienlijke willekeurige verstoringen. We introduceren wanorde door vanuit een vierkant periodiek rooster deeltjes willekeurig te herpositioneren in een gegeven gebied rondom de startpositie, en door willekeurig deeltjes weg te halen. We laten zien dat het systeem nog steeds een laser is, zelfs wanneer we 99% van de deeltjes willekeurig verwijderen. Opvallend is dat deze sterke verstoring de laserconditie, dat wil zeggen de spectrale positie en breedte van de laserlijn niet beïnvloedt en er een minimaal effect op de laser drempel is. Daarnaast analyseren we microscopie-afbeeldingen in de reeele ruimte die we gemaakt

hebben van de lasers boven de laserdrempel. Deze afbeeldingen laten schijnbaar willekeurige spikkels zien. Zulke speckle is bekend uit onderzoek aan verstrooiing van licht aan willekeurige systemen. We analyseren ruimtelijke correlaties in de spikkelpatronen, en ook kansverdelingen in intensiteit. Tot slot gaan we in hoofdstuk 5 van gerandomiseerde roosters naar het rijk van aperiodieke en quasiperiodieke systemen, waarbij we systemen bestuderen die intermediair zijn aan periodieke en gerandomiseerde roosters. We definieren aperiodieke roosters door deterministische getallensequenties toe te passen om te bepalen welke deeltjes in een onderliggend vierkante rooster blijven, en welke verwijderd worden. Op deze manier kunnen we quasi-kristallijne roosters genereren, zoals Galois en Fibonacci roosters, evenals roosters als het Rudin-Shapiro rooster die een fourier transformatie hebben die bijna net zo vlak is als dat van een volledig wanordelijk rooster. We laten zien dat wanneer we de onderliggende onderlinge deeltjesafstand zo kiezen dat deze aan de tweede orde Bragg conditie voldoet, de laser eigenschappen bijna niet veranderen in de zin dat het systeem op dezelfde lasermode opereert als voor het periodieke geval. De quasi- en aperiodieke structuur is wel duidelijk zichtbaar in fourier afbeeldingen boven de drempel, aangezien deze fourier images het patroon van de fourier transformatie van het deeltjesrooster laten zien. Speckle statistiek laat zien dat de speckle ruimtelijke correlaties heeft die bepaald worden door de structuur van het aperiodieke rooster. Tot slot zetten we deze studie voort naar roosters met een onderliggende onderlinge deeltjesafstand die niet overeenkomt met de tweede Bragg conditie en vinden we nieuwe condities waaronder laserwerking optreed. We laten zien dat zulke systemen ook als laser kunnen werken op extra diffractie condities die niet voorkomen in periodieke roosters, maar die specifiek zijn voor quasi-kristallijne structuren.

Gearfetting

Mei ljocht kinne wy de wrâld om ûs hinne sjen. Dit brûke wy net allinne yn ûs deistich bestean, mar ek hat ljocht de minskheid yn steat steld in ynsjoch te krijen yn de gearstalling en foarming fan stjerren, sellen, en sels de struktuer fan atomen. Hjirtroch hat ljocht troch de ieuwen hinne it underwerp fan in protte stúdzjes west en ek hjoed-de-dei noch wurdt ljocht ûndersocht. Al sûnt it minskdom yn steat is om fjoer te meitsjen om ljocht te kreëarjen kinne wy ljocht manipulearje. Undersiik nei ljocht wie altyd fierhinne dreaun troch nijsgjirrigens wêrby't doel wie om in fûneminteel begryp te krijen fan de natuerkunde efter prosessen dy't te meitsjen ha mei ljocht. Tsjinwurdich hat bliken dien dat dizze út nijsgjirrigens dreaun stúdzjes der ta laad ha dat wy ljocht sa stjoere en manipulearje kinne dat wy it brûke kinne yn in protte praktyske tapassingen en technologyen. Wy kinne ûs net mear yntinke hoe't ús libben der út sjen soe sûnder de tapassingen die harren oarsprong ha yn dy ûntdekkingen dy't op de ien of oare manier in relaasje ha mei it begryp fan ljocht. Tink bygelyks oan sinnesellen, wêrby't wy optyske techniken brûke om ljocht effisijint om te setten nei elektrisiteit, ynstee fan dat it absorbearje en ferlern giet oan hjittens. In oare tapassing is ferljochting. Keunstmjittich ljocht brûke wy oeral om ús hinne, en it ûntwerp fan in ljochtboarne dy't folle effisjinter is as de gloeilampe fan Edison hat, lykas sinnesellen, in wichtige ynfloed op it miljeu. In tredde tapassingsgebiet wêrfoar ljocht brûkt wurde kin, is yn de ynformaasjetechnology. Op it stuit is ynformaasjetechnology baseare op elektroanyske sirkwys wêryn elektronen de ynformaasjedragers binne. De wet fan Moore beskriuwt dat de tichtens fan sirkwy eleminten en harren gong eksponinsjeel tanimme. Om dizze foarsizzing wier te meitsjen bliuwe moat in nije technology ûntwikkele wurde dy't oars is as de hjoeddeiske technology dy't gebrûk makket fan elektroanyske sirkwys, omdat elektroanika úteinlik tsjin grinzen oanrint dy't fêststeld wurde troch ferliezen en sinjaal bânbreedte. At wy de mooglikheid ha om op in chip ljocht te stjoeren en te manipulearjen krekt as dat by elektroanen mooglik is, dan soe ljocht de oplossing bringe kinne. Der binne trije grutte foardielen oan it gebrûk fan ljocht yn de kontekst fan ynformaasjetechnology. Earst plantet ljocht har sneller fuort. Twad kin ljocht sûnder ferliezen transporteard wurde. Ta beslút: ljocht kinne wy multiplexe omdat it út mear kleuren bestiet dy 't elts apart fan inoar in ynformaasje kanaal foarmje kinne.It feit dat it brûken fan ljocht yn dizze tapassing noch net realisearre is hat twa oarsaken. Ljocht hat

mar in bytsje ynteraksje mei matearje en dit makket it lêstich ljocht te manipulearjen lykas dien wurdt foar elektroanen. Mei oare wurden: it lykweardige fan in transistor is foar ljocht min te realisearjen. Dêrneist wurdt it brûken fan ljocht beheind troch de diffraksjelimyt lykas dat foar eltse weach jildt. De diffraksjelimyt seit dat it ljochtfjild altyd greater is as de helte fan de weachlingte. Foar sichtber ljocht betsjut dit dat de lytste ôfmjitting altyd greater is as de tipyske komponent grutte yn in elektrysk sirkwie. It wurkgebiet fan de plasmonica adresseart mei krektens dizze twa útdagingen. Plasmonyske materialen binne metalen lykas goud en sulver wêrby't sulver yn it sichtbere diel fan it optysk spektrum de foarkar hat wat ferlies oanbelanget. Behalven de fersterke koppeling tusken plasmonyske materialen en ljocht binne elektromachnetyske fjilden , keppele oan de frije elektroanen, ek nauwer opsletten, wat it mooglik makket de diffraksjelimyt te trochbrekken. It hjoeddeiske ûndersyk yn it fjild fan de nanofotonika draait om it manipulearen fan ljocht op de nanoskaal sadat wy ljocht brûke kinne yn de hjirboppe neamde tapassingen, mar ek om in fundamintiel begryp te krijen. Yn dit proefskrift brûke wy nanofotonika om in laser te meitsjen. Al sûnt de berte fan plasmonika hat der niget west yn it ûntwerpen fan lasers mei plasmonyske materialen. Dizze greate niget komt benammen troch it sicht op tapassingen lykas it mooglik meitsjen fan in coherente ljochtbron yntegrearreop in chip, dy't in fômjitting hat lytser as de diffraksjelimyt. Yn dit proefskrift rjochtsje wy ús benammen op it krijen fan in fundamintiel begryp fan in ienfâldich systeem dat bestiet út de folgjende yngrediënten:1 in fersterkjend medium en 2 perioadike roasters fan sterk ferstruiende plasmonyske dieltsjes . Wy begjinne mei ienfâldige basisfragen. Wat binne de easken om lasing te krijen yn dit systeem? Hoe beynfloedet de sterke struijing fan sulveren dieltsjes dizze easken wannear't wy in ferliking meitsje mei dielektryske lasers mei deselde foarm fan feedback? En hoefolle dusoarder kinne wy yn sa'n sterk struijend roaster ynfiere wêrby't it systeem noch hieltyd as laser wurket? Yn haadstik 1 lizze wy út wêrom plasmonyske dieltsjes sa nijsgjirrich binne yn termen fan harren struijingseigenskippen. Wy jouwe oan wêrom wy se brûke om in trilholte foar in laser te meitsjen. Fierders yntroduseare wy de ingrediënten fan ús laser nammentlik de natuurkunde fan plasmon dieltsjes,weromkoppeling troch in periodyk diffraktyf systeem en fersterking. It ûnderwerp fan lasers easket basiskundem fan it Jablonski diagram dat de energieniveaus beskriuwt fan fluoroforen, spontane en fuortsterke útstjit en generyk gedrach fan lasers. Ta beslút fetsje wy gear wat der yn de literatuur al rapportearre is yn de kontekst fan plasmon lasers en wy lizze út hoe't ús wurk oanfuljend is oan oare plasmon laser types. Yn haadstik 2 presintearje wy experimentele rissultaten foar in laser wêryn't wy in ienfâldich diffraktyf fjouwerkant roaster fan sulveren nanoskiven brûke dy't ynbêdde binne yn in weachlieding mei fluorofoaren. Wy demonstrearje dat dit systeem mei plasmonyske dieltsjes as weromkoppelingselemint as laser wurket. Wy mjitte hjirby net allinnich de linebreedte, fersmelling en drompelcurves lykas hja der typysk útsjogge foar in laser mar komplementair hjiroan mjitte wy ek fourier ôfbyldingen. Fourierflakke byldfoarming is in methoade wêrmei't opservabelen as funksje fan weachvector en dêrmei as funksje fan de hoek metten wurde, ynsté fan de gebrûkelike reeële byldfoarming wêrby't observabelen as funksje fan posysje ôfbylde wurde. Dêrneist brûke wy in technyk om fourier ôfbyldingen by ien as lâns spektraal

op te lossen wat ús yn steat stelt bândiagrammen te mjitten mei fluorescentie. Sokke dispersie diagrammen binne it optyske analogon fan in elektroanyske bânstruktuur en binne in nuttige technyk foar it bestudearjen fan periodike plasmon strukturen en de lasers dy't wy dêrút meitsje. Ta beslút fergelykje wy mjittingen dien mei sulveren struijers mei mjittingen dien mei gouden en titanium dioxide struijers. Ut dizze ferliking kinne wy opmeitsje dat sulveren struijers it dispersie diagram folle mear feroarje as gouden en titanium dioxide struijers dogge, as wy it bândiagram ferlykje mei it ideale bândiagram wêryn tsjinsteld propagerende weagen gjin ynteraksje mei inoar hawwe. Dit wurdt feroarsake troch de sterke plasmonyske struijing fan de sulverdieltsjes, lykas wy opmeitsje kinne út bygelyks de greatte fan de stopgap yn it bândiagram. Yn dit ûndersyk is de resonantie freguentie fan de struijers yn de weachlieding readferskood yn it ljocht fan it spektrum fan spontane útstjit fan de fluorofoor. Yn haadstik 3 litte wy risseltaten sjen fan in systeem dat wer deselde sulveren struijers hat, mar dêr't wy de resonante frekwinsje fan ús struijer troch it emissie spectrum fan de fluorofoor skowe. Om dit mooglik te meitsjen brûke wy in FRET pear fan twa ûngelikense fluoroforen om it frekwinsje berik dêr't wy fersterking yn hawwe te ferskowen nei langere weachlingtes, mar mei hokker wy de fluoroforen noch hieltyd exciteare kinne mei pompweachlingte fan 532 nm. Fierdersoan feroarje wy de resonantie frekwinsje fan de struijer troch de greatte dêrfan te feroarjen. Mei help fan polarisatie oploste spectroscopyske fourier ôfbyldingen raffelje wy de bânstruktuur as funksje fan dieltsjesgreatte út. Út de data kinne wy de konklúzje lûke dat 1) de relatieve stopgap breedte gearhinget mei struijingssterkte en 2) de bânkant wêrop it systeem laserútstjit begjint te jaan bepaald wurdt troch de dieltsjesresonânsje boppe of ûnder de twadde orde Bragg diffraksje. Dêr't haadstik 2 en 3 om in folsleine beskriuwing fan lasers makke út perodike roasters fan dieltsjes, rjochtsje wy ús yn haadstik 4 en 5 op de fraach hoe't dit systeem feroaret as wy it perodike roaster bot fersteure. Yn haadstik 4 bestudearje wy dieltjesroasters mei frijwat eigenwillige fersteuringen. Wy helje disoarder binnen troch fanút in fjouwerkant periodyk roaster dieltjes eigenwillich in nij plak te jaan yn in fêststeand gebiet om de startposysje hinne en troch eigenwillich dieltjes wei te heljen. Wy litte sjen dat it systeem noch hieltyd in laser is, sels as wy 99 prosint fan de dieltsjes eigenwillich fuorthelje. Opfallend is dat dizze sterke fersteuring de laserkondysje,dat wol sizze de spectrale posysje en breedte fan de laserline, net beynfloedet en dat der in sa'n lyts mooglik effekt op de laser drompel is. Dêrneist analiseare wy mikroskopyske ôfbyldingen yn de wurklike rûmte dy't wy makke hawwe fan de lasers boppe de laserdrompel. Dizze ôfbyldingen litte nei't it liket eigenwillige spikkels sjen. Sok speckle is bekend út ûndersyk oan struijing fan ljocht oan eigenwillige systemen. Wy analiseare rûmtlike gearhing yn de spikkelpatroanen en ek kânsferdielingen yn intensiteit. Ta beslút geane wy yn haadstik 5 fan randomisearde roasters nei it ryk fan aperiodike en sabeareperiodike systemen wêrby't wy systemen bestdearje dy't yntermediair binne oan periodike randomisearde roasters. Wy defineare aperiodike roasters troch deterministyske getallesequenties ta te passen om te bepalen hokker dieltsjes yn in ûnderlizzend fjouwerkant roaster bliuwe en hokker fuorthelle wurde. Op dizze wize kinne wy sabeare-kristalline roasters meitsje lykas Galois en Fibonacci roasters, en roasters as it Rudin-Shapiro roaster dy't in fourier

transformaasje hawwe dy' t hast like flak is as dat fan in folslein disoarderlik roaster. Wy litte sjen dat bywannear't wy de ûnderlizzende ûnderlinge dieltsjesôfstân sa kieze dat dizze oan de twadde oarder Bragg kondysje foldocht, de laser eigenskippen hast net feroarje yn dy sin dat it systeem op deselde lasermoade wurket as foar it periodike gefal. De sabeare-en aperiodike struktuur is wol dúdlik sichtber yn fourier ôfbyldingen boppe de drompel, omt dizze fourier images it patroan fan de fourier transformaasje fan it dieltsjesroaster sjen litte. Speckle statistyk lit sjen dat de speckle rûmtlike gearhing hat dy't bepaald wurdt troch de struktuur fan it aperiodike roaster. Ta beslút sette wy dizze stúdzje troch nei roasters mei in ûnderlizzende ûnderlinge dieltsjesôfstân dy't net oerienkomt mei de twadde Bragg kondysje en fine wy nije kondysjes ûnder hokker laserwurking him foardocht. Wy litte sjen dat sokke systemen ek as laser wurkje kinne op ekstra diffraksje kondysjes dy't net foarkomme yn periodike roasters mar dy't eigen binne oan sabeare-kristalline strukturen

List of publications

This thesis is based on the following publications:

- *Lasing at the band edges of plasmonic lattices*, A. H. Schokker and A. F. Koenderink, Phys. Rev. B **90**, 155452 (2014). **(Chapter 2)**
- *Statistics of Randomized Plasmonic Lattice Lasers*, A. H. Schokker, A. F. Koenderink, ACS Photonics. **2**,1289-1297 (2015). **(Chapter 4)**
- *Lasing in aperiodic systems*, A. H. Schokker and A. F. Koenderink, in preparation. **(Chapter 5)**
- *Band structure in plasmonic lattice lasers*, A. H. Schokker, F. van Riggelen,Y. Hadad and A. Alù, and A. F. Koenderink, in preparation. **(Chapter 3)**

Other publications by the author:

- *Experimental Realization of a Polarization-Independent Ultraviolet/Visible Coaxial Plasmonic Metamaterial*, M. A. van de Haar, R. Maas, A. H. Schokker, and A. Polman, Nano Lett. **14**, 6356-6360 (2014).
- *Plasmonic phase-gradient metasurface for spontaneous emission control*, L. Langguth, A. H. Schokker, K. Guo, and A. F. Koenderink, Phys. Rev. B **92**, 205401:1-9 (2015).

Dankwoord

Ik wil een aantal mensen bedanken voor het tot stand komen van dit proefschrift en voor de fijne tijd die ik gehad heb op AMOLF.

Allereerst wil ik mijn promotor Femius Koenderink bedanken. Vier jaar lang heb ik onderzoek in je groep mogen doen. Je bent altijd erg betrokken bij je PhDs en maakt veel tijd voor ze vrij. Als ik je 's avonds emailde stuurde je altijd diezelfde avond een antwoord terug en als ik je tekst gaf om te corrigeren kreeg ik dit gewoonlijk binnen een dag terug. Ook geef je je Phd's veel vrijheid voor wat betreft het bepalen van de richting van hun onderzoek. Je bent erg georganiseerd en werkt efficient en gestructureerd. Zo maak je voor alles een planning, heb je de gewoonte om ook zaken die niet gerelateerd zijn aan wetenschap of onderzoek in termen van wiskundige termen te beschrijven, en als iemand een wollige vraag stelt, herhaal je de vraag in een verkorte en duidelijke vorm. In dit opzicht was je een voorbeeld voor mij en heb ik veel van je kunnen leren en dit is iets waar ik ook na mijn promotie veel profijt van ga hebben. Daarnaast heb je natuurlijk ontzettend waardevolle input gegeven voor wat betreft mijn onderzoek, wat bijgedragen heeft aan het tot stand komen van dit proefschrift.

Daarnaast wil ik Albert Polman bedanken. Tijdens mijn master volgde ik je Nanophotonics college en hierdoor ben ik bij AMOLF terecht gekomen. Dit bleek achteraf een erg goede keuze en ik heb hier heel veel aan te danken. Ik kan me nog goed herinneren dat ik na het laatste college van het vak *Nanophotonics* aan je wilde vragen of ik mijn masteronderzoek bij jou in de groep kon doen. Het was nog niet eenvoudig mijn vraag te stellen omdat er een rij studenten klaar stond die doorliep tot achterin het lokaal die je allemaal iets wilden vragen- je had op veel studenten indruk gemaakt. Je colleges en de tijd die ik bij je in de groep heb gezeten heb ik erg gewaardeerd en hebben me veel geleerd.

I would also like to thank James Parsons, who was my direct supervisor during my masters project. You introduced me to the cleanroom and showed me how to do nanofabrication. With your help I was able to learn how to use all equipment in the cleanroom within a few months. Thanks!

Ook wil ik mijn groepsleden uit de groep Resonant Nanophotonics bedanken. In mijn eerste jaren als promovendus hoorden Martin en Ivana hier bij. Martin, ik kan me nog goed herinneren dat je in het eerste jaar van het promotieonderzoek tegen me zei

"Hinke, I don't think your samples will ever lase". Je was van nature kritisch, maar daarmee was je ook altijd degene die de meest scherpe en waardevolle opmerkingen maakte tijdens groepsbesprekingen, poster sessies en colloquia. Ivana, thanks for your help in my first year and thanks for showing me the Duimelijn set up. Andrej, je bent een erg fijne collega en stond altijd klaar voor anderen. Je beterschapskaartje met Spitfire bewaar ik goed. Felipe, many thanks for your support and help during my PhD. I have very much appreciated your positive and happy attitude and your buddhist approach to everything. Lutz, thanks for your suggestions and useful input during groupmeetings. I really enjoyed our collaboration project and even sharing the lab with you was somehow a fun experience. I can remember you describing the lab "as if a crazy and blind racoon had entered the lab and trashed it" when I had finsihed doing my measurements. I like your creative approach to everything which have always resulted in very nice ideas for potential new experiments. Cocoa, you may not have the loudest voice during groupmeetings, but whenever you make a comment it is always useful. I am happy that you will continue with the Spitfire set up and with the lasing experiments and I am sure you will do succesfull measurements with it! Abbas, Hugo, Remmert, Wouter, Mengqi, Allessandro, and Clara thanks for your input during groupmeetings and presentation practice drill sessions. Floor van Riggelen, jou wil ik ook bedanken. Je kwam in mijn laatste jaar als masterstudent in de groep onder mijn begeleiding. Voordat je begon gaven we je de keuze uit 7 onderwerpen om je onderzoek in te doen. Je koos een onderwerp, ging ermee aan de slag en je maakte je onderzoek tot een groot succes. Je data bleek zo waardevol te zijn dat je resultaten tot een artikel leiden. Daarnaast was je gewoon een hele fijne collega om mee samen te werken en een gezellige kamergenoot! Je resultaten hebben bijgedragen aan het tot stand komen van hoofdstuk 3.

Said, Vasco, Alexei and Alexandre, and Per many thanks for the scientific discussions and useful input! Leontien, bedankt voor de gesprekken gedurende het laatste jaar van mijn promotieonderzoek. Ik heb je adviezen erg gewaardeerd en ter harte genomen en dit heeft zeker geholpen bij het tot stand komen van dit proefschrift.

Mijn onderzoek was niet mogelijk geweest zonder de hulp van alle collega's die hebben meegeholpen in het ontwerpen van de opstelling, het schrijven van software, en het oplossen van elektronica uitdagingen. Henk-Jan en Ilyah, bedankt voor de microscoop mount van Spitfire! Jan Zomerdijk en Idsart, bedankt voor de piezo's en de pulse integrator. Marko Kamp, bedankt voor al je hulp in het lab. Het was een interessante samenwerking. Ik moet wel een erg lastige promovendus voor je zijn geweest in het begin. Ik wilde het liefst zoveel mogelijk zelf doen in het lab, terwijl jij juist zoveel mogelijk wilde helpen. Dit betekent overigens niet dat je niet hebt bijgedragen aan het experimentele deel van mijn onderzoek. Vooral in de ontwerp fase heb je erg veel input gegeven. Daarnaast had je altijd wel verhelderende ideeën en suggesties als ik tegen problemen aan liep en wist je op de één of andere manier alle praktische problemen op te lossen. Zo was er een moment waarop mijn camera niet meer werkte door oververhittingsproblemen. Je pakte een pen, begon daarmee tegen de ventilator aan te duwen en sindsdien werkte mijn camera weer. MacGyver van het optische lab! Bedankt dat je mijn paranimf wilt zijn.

Al in de eerste paar maanden van mijn promotie was duidelijk dat de software een uitdagend project op zich zou zijn, omdat we de ambitie hadden om single shot metingen te doen en de camera en spectrometer tegelijkertijd met de laser getriggerd moest worden. Marco Konijnenburg en Sjoerd wil ik graag bedanken voor alle projectbijeenkomsten en het meedenken hierover. In het bijzonder wil ik Marco Seynen bedanken voor het schrijven van de software. Niet alleen was er de uitdaging van het triggeren, maar ook moest de AOM aangestuurd worden, wilden we een automatisch aangestuurd filterwiel en zo waren er nog vele andere details. Niet alleen heb je nog vele opties toegevoegd maar ook stond je altijd klaar als ik iets nieuws toegevoegd wilde hebben. Als ik metingen met collega's deed waren ze altijd verbaasd over hoe alles zo eenvoudig automatisch werkte met de spitfire software. Bedankt daarvoor!
In mijn amolf tijd heb ik vele dagen doorgebracht in de cleanroom. Hans Zeijlemaker, Dimitry Lamers en Andries Lof, bedankt voor alle hulp en ondersteuning! Het maakt niet uit wat er gebeurde of wat er mis ging, jullie gingen altijd vol goede moed en optimisme er mee aan de slag en zorgden er altijd voor dat het opgelost werd, of het nu om een vastgelopen computer ging of een in stukken gezaagd onderdeel van de Kameleon.
Zoals vele collega's op AMOLF zullen beamen is er om wetenschappelijke successen te bereiken niet alleen hard werk, goede ideeën en een goede ondersteuning nodig, maar is goed contact met collega's net zo belangrijk. In de personeelsvereniging heb ik dit extra mogen ervaren. Nuria, Gesa, Anouk, Roeland, Joris, Bart, Marie Anne en Ronald bedankt voor de leuke PV tijd. Marie Anne, het bleek dat we een gezamenlijke interesse in paarden hadden en hier konden we eigenlijk elke dag wel weer opnieuw over praten. Op collega's had dit een wisselend effect: soms wisten we collega's te enthousiasmeren en soms haakten ze af. Memorabel in de geschiedenis van AMOLF is die keer dat we met de PV een personeelsuitje van heel AMOLF naar een paardenmanege hadden georganiseerd. Evenzo opmerkelijk is dat we dit hadden bewerkstelligd met een democratische verkiezing in de PV meeting. Achteraf was iedereen erg enthousiast. Ook hebben we samen vele uren in de cleanroom doorgebracht. De cleanroom technici werden altijd een beetje huiverig als ze ons samen in de cleanroom zagen, ondanks ons verweer dat cleanroom malfuncties alleen correleren met gebruikerstijd en niet met hoe luidruchtig de gebruikers zijn. Daarnaast heb ik vele goede herinneringen aan de keren dat we hotelkamers hebben gedeeld (gelukkig heb ik je maar éen keer verward met een wekker), en de keren dat we samen workshops hebben geleid tijdens de AMOLF open dagen. Ik ga onze gezamenlijke AMOLF tijd missen!
Benjamin, ik wil jou ook bedanken voor de fijne AMOLF tijd. Samen met Marie Anne zijn we onze Phd op AMOLF begonnen na onze master gedaan te hebben in utrecht. Je bent altijd in voor een gesprek en ik kan altijd bij je terecht als ik ergens over wil praten. Je liep vaak mijn kamer binnen om te kletsen over wat je bezig houdt en wat je gaat doen. Het kwam daarbij regelmatig voor dat je na 1 minuut alweer vergeten was waarom je eigenlijk mijn kamer binnen liep, maar dat vormde voor jou geen belemmering om door te blijven praten. Ook heb ik goede herinneringen aan de AMOLF hardloopgroep, waar jij samen met Mark de drijvende kracht achter was. Tot slot was je nooit te beroerd om uitgebreide schuine en half rijmende gedichten te

schrijven voor sinterklaas en ervoor te zorgen dat ik elk jaar weer naar voren werd geroepen.
Freddy Rabouw, Gydo van Zundert en Niek den Harder, jullie waren samen met Marie Anne en ik deel van het Powertrio. Hoewel we het allemaal altijd te druk hadden om af te spreken hebben we toch wat avonden vrij kunnen maken om samen te eten. Bedankt voor de leuke tijd tijdens de studie en daarna!
Jan Bonne Aans, bedankt voor het controleren van de Friese samenvatting van dit proefschrift! En natuurlijk voor het helpen tijdens de open dag bij de vouwmicroscopen workshop. Bart Vos, bedankt voor je gezelligheid en je koekjes en natuurlijk bedankt voor al die keren dat je mijn bureau hebt opgeruimd. Frans Giskens, Marc Duursma en Ronald Buijs, bedankt dat jullie mee wilden doen met het meisjesteam van Marie Anne en mij op de FOM sportdag. Het beeld van jullie in roze t-shirts beplakt met pluche bollen staat bij vele AMOLFers nog op het netvlies gebrand. Frans, je kwam regelmatig eens mijn kantoor of lab binnen om bij te praten. Bedankt voor je humor en gezelligheid. Ook wil ik mijn kamergenoten Anouk en Ruben, en mijn voormalige kamergenoten Daan, Dolfine, Claire, Jochen en Timmo bedanken voor de gesprekken en gezelligheid. Daarnaast zijn er nog vele AMOLFers die zorgden voor gezelligheid tijdens koffiepauzes, borrels en AMOLF uitjes: Mark, Mohammed, Rick, Hinco, Jorik, Ruben, Boris, Niels, Parisa, Annemarie, Freek, Cristina, Giorgos, Martijn, Toon, en vele anderen op AMOLF bedankt!

Tot slot wil ik mijn familie en vrienden bedanken. In het bijzonder wil ik mijn ouders, Hendrik, Marike, Niki en David bedanken voor de steun, hulp en aanmoediging tijdens mijn onderzoek.